Thèse n° 10 201

Spectral and thermodynamic properties of interacting electrons with dynamical functionals

Présentée le 2 mai 2023

Faculté des sciences et techniques de l'ingénieur
Laboratoire de théorie et simulation des matériaux
Programme doctoral en science et génie des matériaux

pour l'obtention du grade de Docteur ès Sciences

par

Tommaso CHIAROTTI

Acceptée sur proposition du jury

Prof. A. Mortensen, président du jury
Prof. N. Marzari, Dr A. Ferretti, directeurs de thèse
Prof. L. Reining, rapporteuse
Prof. M. Capone, rapporteur
Prof. G. Carleo, rapporteur

École
polytechnique
fédérale
de Lausanne

2023

Acknowledgments

I am very grateful to Andrea and Nicola for having walked with me on this journey.

And to all my friends, I say thank you.

Abstract

Empowered by ever-increasing computational power and algorithmic developments, electronic-structure simulations continue to drive research and innovation in materials science. In this context, ab-initio calculations offer an unbiased platform for the understanding, development, design, and discovery of materials. The treatment of the electron interactions is at the core of any ab-initio method, with the accuracy of its solution affecting the final result. Here, dynamical functionals can play a crucial role in allowing the accurate prediction of spectral and thermodynamic properties of materials.

In this thesis we develop a framework to deal with dynamical quantities, and a novel dynamical functional to address the electronic structure of correlated materials.

We design the so-called sum-over-poles representation for dynamical propagators to perform accurately the calculations in dynamical frameworks. Then, we draw a link between the fundamental equation of Green's function formalism, the Dyson equation, and nonlinear eigenvalue problems, also highlighting that the Dyson equation is the (nonlinear) generalization of the Schrödinger equation for embedded systems. Notably, the sum-over-poles representation of the dynamical potential allows for an exact solution of the nonlinear problem by mapping the interacting system to a non-interacting "fictitious" system with augmented degrees of freedom and having the same Green's function of the interacting system, with the spurious degrees of freedom traced away. The (linear) diagonalization of the effective Hamiltonian for the "fictitious" system yields the Dyson orbitals of the material as the eigenvectors of the nonlinear problem, and the poles of the Green's function, i.e., the excitation energies of the material, as the eigenvalues. Also, the sum-over-poles representation of the Green's function is known and allows for the computation of accurate spectroscopic and thermodynamic quantities.

Furthermore, we introduce a novel approximation to the exchange-correlation part of the Luttinger-Ward functional, that generalizes the energy functional of DFT+U to host a dynamically screened potential $U(\omega)$. Exploiting a localized-GW approach, we combine the precision of DFT+U for ground-state properties with the accuracy of GW for spectroscopic quantities and design the so-called dynamical Hubbard (Luttinger-Ward) functional. This yields a localized-GW self-energy as derivative, and simplifies to DFT+U in the case of a static

screening.

To test the approach, we use the algorithmic-inversion method on sum over poles to calculate the spectroscopic and thermodynamic quantities of the homogeneous electron gas at the *GW* level, finding very good agreement with previous results.

Finally, we combine the algorithmic inversion method on sum over poles with the dynamical Hubbard functional to study the electronic structure of correlated materials. We apply the framework to compute the spectral, thermodynamic, and vibrational properties of $SrVO_3$. We find results in excellent agreement with experiments and state-of-the-art computational methods, but with negligible simulation costs.

Sommario

Potenziate dalla sempre maggiore capacità di calcolo e dai progressi degli algoritmi, le simulazioni di struttura elettronica continuano a guidare la ricerca e l'innovazione nella scienza dei materiali. In questo contesto, i calcoli ab-initio offrono una piattaforma imparziale per la comprensione, lo sviluppo, la progettazione e la scoperta di nuovi materiali. Il trattamento delle interazioni elettroniche è al centro di qualsiasi metodo ab-initio, con l'accuratezza della sua soluzione che influisce sul risultato finale. Qui, i funzionali dinamici possono svolgere un ruolo cruciale nel permettere la previsione accurata delle proprietà spettrali e termodinamiche dei materiali.

In questa tesi sviluppiamo un metodo teorico e computazionale per gestire le quantità dinamiche e un nuovo funzionale dinamico per calcolare la struttura elettronica dei materiali correlati.

Rappresentiamo i propagatori dinamici in somme di poli al fine di eseguire con precisione i calcoli nei metodi dinamici. Successivamente, stabiliamo un collegamento tra l'equazione fondamentale per le funzioni di Green in materia condensata, l'equazione di Dyson, e i problemi agli autovalori non lineari, evidenziando che l'equazione di Dyson è la generalizzazione (non lineare) dell'equazione di Schrödinger per sistemi aperti. In particolare, la rappresentazione di somma di poli di un potenziale dinamico consente la soluzione esatta del problema non lineare grazie a una mappa del sistema interagente su un sistema "fittizio" non interagente con gradi di libertà aumentati e avente la stessa funzione di Green del sistema interagente, con i gradi di libertà spurii tracciati via. La diagonalizzazione (lineare) dell'hamiltoniana effettiva per il sistema "fittizio" restituisce gli orbitali di Dyson del materiale come autovettori del problema non lineare e i poli della funzione di Green, cioè le energie di eccitazione del materiale, come autovalori. Infine, la procedura determina la rappresentazione in somma di poli della funzione di Green, rendendo possibile il calcolo accurato di quantità spettroscopiche e termodinamiche.

Inoltre, introduciamo una nuova approssimazione per la parte di scambio-correlazione del funzionale di Luttinger-Ward, generalizzando il funzionale energia di DFT+U per trattare un potenziale schermato dinamicamente, $U(\omega)$, invece che statico. Sfruttando un approccio GW

localizzato, combiniamo la precisione di DFT+U per le proprietà di stato fondamentale con l'accuratezza di *GW* per le grandezze spettroscopiche e progettiamo il cosiddetto funzionale di Hubbard dinamico (Luttinger-Ward). La derivata di questo restituisce una self-energia *GW* localizzata, ma contemporaneamente si semplifica al funzionale DFT+U nel caso di uno screening statico.

Per testare l'approccio, utilizziamo il metodo di inversione algoritmica su somma di poli per calcolare le grandezze spettroscopiche e termodinamiche del gas omogeneo di elettroni a livello *GW*, trovando un accordo molto buono con i risultati precedenti.

Infine, combiniamo il metodo di inversione algoritmica su somma di poli con il funzionale di Hubbard dinamico, per studiare la struttura elettronica dei materiali correlati. Applichiamo il metodo per calcolare le proprietà spettroscopiche, termodinamiche e vibrazionali di $SrVO_3$, trovando risultati in ottimo accordo con gli esperimenti e i metodi computazionali all'avanguardia, ma a un costo di simulazione di molto inferiore.

Contents

1 Introduction and overview

Computational materials science is a major driving force for understanding, modeling, and discovering materials [1]. Ab initio simulations, enabled by ever-increasing computational power and algorithmic advances, offer a platform for unbiased prediction of material properties that can be useful for understanding materials [2], making accurate comparisons with experiments [3], or even designing new materials [4].

The computational simplicity and accuracy of density functional theory has contributed massively to these areas, improving upon ab initio simulations in the context of phase diagrams, molecular dynamics, vibrational properties, but also contributing to spectroscopic and optical predictions, as shown in Refs. [5, 6, 7, 8].

The interaction between electrons in the Schrödinger equation is at the core of the difficulty of the problem, making it analytically unsolvable and numerically very expensive to treat. Differently than for atoms and small molecules, where an exact treatment of the interaction between the electrons is computationally feasible, in solids the situation is much different since in principle at least an Avogadro number of electrons are present.

Density-functional theory (DFT) maps the search of the ground-state wave function to the minimization of an energy functional of the density, effectively passing from a problem with an almost infinite number of variables to a problem with only the space x, y, z variables. The price to pay is the knowledge of the functional. In the Schrödinger formulation of quantum mechanics the functional of the N-particle wave function is known, in density functional theory it is not [9]. The celebrated local-density approximation [9], together with its generalizations, e.g., by Perdew, Burke, and Ernzerhof [10], are common approximate density functionals used for calculations on solids nowadays.

Importantly, for practical applications of density functional theory, the interacting system of electrons is mapped to a non-interacting "fictitious" system where the electrons feel an effective modified external potential. This Kohn-Sham mapping guarantees that the ground-state density is the same as that of the interacting "true" system. Most naturally, the (charged)

excitations of the non-interacting Kohn-Sham system, i.e., the band structure in solids, are interpreted as the excitations of the material, and its stationary states as the quasiparticles even though this is not really accurate [11].

Though density-functional theory has provided a major step forward, it remains challenging to improve on existing approximate functionals [12], often resulting in incorrect predictions for complex or strongly-correlated systems [13]. Also, addressing spectroscopic quantities from the Kohn and Sham band structure can lead to incorrect predictions even on the most simple materials [14, 15, 16, 17].

As discussed in Chapter 2, Green's function dynamical formalisms can improve these limitations. Not only designed for spectroscopics [18], the existence of variational energy functionals of the Green's function [19] leads to an effective simplification of the many-body problem. This can be at the base of a new computational revolution as it was for DFT.

While the different Green-function-based frameworks differ, a common element is the appearance of dynamical potentials. For example, many-body perturbation theory (MBPT) reduces the multi-particle electronic degrees of freedom to a single particle subjected to a non-local and dynamical potential, which is the electron-electron self-energy [20]. Dynamical mean-field theory (DMFT) couples a real-space impurity with the rest of the system, requiring self-consistency between the impurity and the bath [21, 22, 23]. Coherent electronic-transport theories use a Green's function embedding to calculate the electronic conductance of, for example, a conductor between two semi-infinite leads, coupling the three systems dynamically [24, 25]. Thus, properly handling frequency-dependent potentials is of central interest in the field.

As far as total energies are concerned, the Luttinger-Ward (LW) and Klein functionals [19, 26, 27, 20, 28] are variational energy functionals of the Green's function that result in conserving dynamical potentials at self-consistency. Although the Φ term is explicitly known diagrammatically, it is computationally inaccessible and needs to be approximated [29, 30]. The choice of approximation for Φ determines the physics accessible to the functional, ranging from long-range plasmonic effects, as in GW [31, 18], to strongly correlated local interactions, as in DMFT [21, 32]. The stationarity condition of the functional yields the Dyson equation, involving the interacting propagator G and the dynamical self-energy (as a derivative of Φ with respect to G) [20, 28]. Therefore, the functional and its derivative determine the quality of the predictions of the thermodynamic and spectral properties of a material, allowing, at self-consistency, the computation of ground-state quantities such as forces and phonons through the Hellmann-Feynman theorem [32].

In this thesis we propose a novel theoretical and computational framework to obtain accurate spectroscopic and thermodynamic properties of materials based on interacting-electrons formulations and dynamical potentials.

First, in Chapters 3 and 4, we introduce a novel "algorithmic inversion method on sum over

poles" (AIM-SOP) to deal with dynamical potentials.

Specifically, in Chapter 3, we develop a representation suited for a dynamical potential as a "sum over poles" (SOP). In this framework, we study how to transform a propagator from the frequency domain to a SOP form. Furthermore, we develop an improved basis set called the n-th order Lorentzians to improve the accuracy and decay properties of the resulting SOP.

Then, in Chapter 4, we discuss the Dyson equation as a nonlinear eigenvalue problem and show a way to solve it using the algorithmic-inversion method. Similar to Kohn and Sham DFT, the SOP representation of the dynamical potential allows us to exactly map the interacting system into a non-interacting "fictitious" system with augmented degrees of freedom, i.e., the poles of the self-energy. This non-interacting system allows us to compute the Green's function via a matrix diagonalization of a larger effective (exact) Hamiltonian. The exact SOP representation of the interacting Green's function is found by tracing away the fictitious degrees of freedom, granting access to the Dyson orbitals and the excitation energies of the system. Additionally, the SOP form for the Green's function allows for the accurate computation of the thermodynamic properties, i.e., the frequency-integrated ground-state properties of the system.

Having set up the computational framework, in Chapter 5, we introduce a novel approximation to the exchange-correlation part of the Luttinger-Ward functional. By exploiting a localized-GW approach, we generalize the energy functional of DFT+U to host a dynamical screening $U(\omega)$. The so-called "dynamical Hubbard functional" features a localized-GW self-energy as a derivative while maintaining DFT+U-like accuracy for the thermodynamics. In particular, when a static screening U is used, the dynamical Hubbard functional yields the Dudarev et al. form of DFT+U [33].

As a test case study for AIM-SOP, in Chapter 6, we investigate the homogeneous electron gas (HEG) in the GW approximation. We implement the method in a computer code, enabling accurate numerical computations of spectral and thermodynamic quantities simultaneously. We compare the results with previous literature and find very good agreement in terms of the spectral function, effective mass, renormalization factor, and total energy at several densities of the HEG.

By combining AIM-SOP with the dynamical Hubbard functional, we develop a framework capable of accurately tackling the electronic structure of correlated materials in Chapter 7. We implement the formalism in a PYTHON code, taking advantage of the DFT results for the starting electronic structure and the random-phase approximation (RPA) for the screening. We apply the formalism to study the correlated metal $SrVO_3$, and find results in very good agreement with experiments and state-of-the-art methods for the spectrum, bulk modulus, and vibrational properties, at a greatly reduced computational cost compared to established approaches.

This thesis is mainly based on my two publications in Refs. [34] and [35], which were published

during my doctorate.

1.1 Organization of the work

The rest of the thesis is organized as follows:

- In Chapter 2, we provide an overview of the general framework of Green's functions. Specifically, in Sec. 2.1, we introduce the many-body problem and explain how one-particle Green's functions can simplify it. In Sec. 2.2, we show how the self-energy is related to embedding theory. In Sec. 2.3, we discuss energy functionals in both DFT and Green's function formalisms. In Sec. 2.4, we compare Green's function theories with linear response. In Sec. 2.5, we focus on the analytic structure of the Green's function. In Sec. 2.6, we elaborate on dynamical propagators for describing interacting systems. In Sec. 2.7, we draw a link between the Green's functions and angle-resolved photoemission spectroscopy.

- In Chapter 3, we introduce the sum-over-poles method to represent dynamical propagators. Specifically, in Sec. 3.1, we provide an overview of the AIM-SOP approach, discussing its main goals and the SOP form for propagators and self-energies. In Sec. 3.2, we discuss the connection between a propagator and its spectral function. In Sec. 3.3, we provide the numerical procedure to transform a propagator sampled on a frequency grid to a SOP representation. In Sec. 3.4, we introduce several useful expressions when dealing with propagators on SOP, like analytic convolutions and moments. In Sec. 3.5, we provide numerical examples of the representation on SOP for a test propagator.

- In Chapter 4, we introduce the algorithmic inversion method to solve Dyson-like equations. Specifically, in Sec. 4.1, we discuss the Dyson equation in the context of non-linear eigenvalue problems, drawing a link between the physical and mathematical frameworks. In Sec. 4.2, we design the algorithmic inversion method in the scalar (homogeneous) case. In Sec. 4.3, we extend the method to a general operatorial (non-homogeneous) case to apply it to real systems.

- In Chapter 5, we introduce a novel approximation to the exchange-correlation part of the Klein functional, termed the dynamical Hubbard functional. Specifically, in Sec. 5.1, we discuss the need for the Hubbard manifold to separate short- and long-range interactions. In Sec. 5.2, we propose a way to localize GW. In Sec. 5.3, we present the novel functional. In Sec. 5.4, we elaborate on the double counting needed for the final form of the functional.

- In Chapter 6, we apply the AIM-SOP method to the homogeneous electron gas at the GW level. Specifically, in Sec. 6.1, we elaborate on the problem of computing spectral and thermodynamic quantities jointly, and explain how AIM-SOP addresses the problem. In Sec. 6.2, we discuss the application of AIM-SOP to the HEG for spectral quantities.

In Sec. 6.3, we discuss the thermodynamics. In Sec. 6.5, we present the results on the electron gas. In Sec. 6.6, we provide a summary of the chapter.

- In Chapter 7 we combine the AIM-SOP method with the dynamical Hubbard functional to address the electronic structure of correlated materials. Specifically, in Sec. 7.1 we discuss the screening $U(\omega)$ as an averaged RPA screened potential. In Sec. 7.2 we elaborate on its application to compute the spectroscopics of real crystals. In Sec. 7.3 we move to the thermodynamic quantities. In Sec. 7.5 we show the results on $SrVO_3$. In Sec. 7.6 we give a recap of the Chapter.

- In Chapter 8 we give the conclusions together with some future perspectives.

We use the "we" throughout almost the whole thesis, also highlighting how this work is the result of the collaboration and supervision of A. Ferretti and N. Marzari. When the first person is used it refers to T. Chiarotti.

2 Green's functions, embedding, and energy functionals

In this chapter, we start by introducing one-particle Green's functions. Then, we discuss self-energies in the context of embedding theory. Additionally, we show that energy functionals can be used to find good approximations for solving the many-body problem. Furthermore, we provide an overview of the differences between Green's function methods and linear response theories, highlighting the importance of time-ordering and the dynamical nature of the self-energy. Finally, we point out the link with experimental observables. Throughout the thesis, we assume that we are at zero temperature and are dealing with spinless fermions, i.e., the spin-unpolarized case. The contents of this chapter are adapted from Refs. [20, 28, 36].

2.1 Green's function: general theory

In this section, we introduce the one-particle Green's function starting from the many-body Hamiltonian.

In physics, it is fundamental to approach a problem based on the quantity one wants to predict. This allows for a reduction of information and helps in understanding the fundamental variables, designing experiments, and finding a cost-effective (or even possible) way of computing the desired quantities using a computer. In electronic-structure methods for computational condensed matter physics, the aim is to predict the dynamics of electrons within a solid. By means of the Born-Oppenheimer approximation, the nuclear degrees of freedom (DOF) are decoupled from the electronic DOF and fixed at some positions [37]. As a consequence, the kinetic energy of the nuclei can be neglected, and one can focus on the electronic part of the many-body Hamiltonian, which, in position space and atomic units, is given by

$$H = -\sum_i \frac{\nabla_i^2}{2} - \sum_{i,I} \frac{Z_I}{|\mathbf{r}_i - \mathbf{R}_I|} + \sum_{I<J} \frac{Z_I Z_J}{|\mathbf{R}_I - \mathbf{R}_J|} + \sum_{i<j} \frac{1}{|\mathbf{r}_i - \mathbf{r}_j|}, \tag{2.1}$$

where the sums run over N electrons and M nuclei. The first term represents the kinetic energy of the electrons, the second term represents the interaction between electrons and

nuclei, the third term is the nucleus-nucleus interaction (just a shift of the total energy since nuclear positions are frozen), and the fourth term represents the electron-electron interaction. Upon diagonalization of the Hamiltonian, one obtains the stationary modes of the system as eigenvectors and the corresponding energies as eigenvalues. In the absence of perturbations, the system stays in its least energetic eigenmode, the ground-state, represented as a vector $|GS\rangle$ in the N-particle Hilbert space. It is worth noting that neglecting the interacting term, the eigenvectors of the above Hamiltonian are Slater determinants [38] composed of the eigenvectors of the single-particle Hamiltonian. This follows from the fact that in a non-interacting system the total energy is the sum of the single-particle energies, and takes into account that the many-electron wave function is antisymmetric since we deal with fermions. However, when we switch on the interaction between electrons, the problem cannot be factorized anymore, and a full diagonalization of the many-body Hamiltonian is required. This scales almost with a cubic law with the dimension of the Hilbert space. Considering a basis of Slater determinants (e.g., the eigenstates of the non-interacting Hamiltonian), we see that the dimension of the Hilbert space is equivalent to the binomial coefficient with on top the number of elements in the basis of the single-particle Hilbert space and on the bottom the number of particles. All in all, this results in an exponential scaling of the space dimension with the number of particles in the system, which is unfeasible for classical computers even with a small number of electrons.

To simplify the problem, instead of predicting the full dynamics of the system, one can focus just on computing the *expectation values* of observables to directly compare them with experiments. For single-particle properties (operators), if one knows the density matrix of the system (in the Schrödinger picture), i.e.,

$$\tilde{n}(\mathbf{r}, t; \mathbf{r}', t) = \int \mathrm{d}\mathbf{r}_2 \ldots \mathrm{d}\mathbf{r}_n \, \Psi(\mathbf{r}, \mathbf{r}_2, \ldots, \mathbf{r}_N; t) \Psi^*(\mathbf{r}', \mathbf{r}_2, \ldots, \mathbf{r}_N; t), \tag{2.2}$$

the expectation value of one-particle operators can be computed effectively as

$$\begin{aligned} \langle \Psi | O | \Psi \rangle &= \int \mathrm{d}\mathbf{r} \, \mathrm{d}\mathbf{r}_2 \ldots \mathrm{d}\mathbf{r}_n \, \mathrm{d}\mathbf{r}' \, \Psi(\mathbf{r}, \mathbf{r}_2, \ldots, \mathbf{r}_N; t) O(\mathbf{r}, \mathbf{r}') \Psi^*(\mathbf{r}', \mathbf{r}_2, \ldots, \mathbf{r}_N; t) \\ &= \int \mathrm{d}\mathbf{r} \, \mathrm{d}\mathbf{r}' \, \tilde{n}(\mathbf{r}, t; \mathbf{r}', t) O(\mathbf{r}, \mathbf{r}'). \end{aligned} \tag{2.3}$$

This represents a major simplification to the problem, since we avoid the calculation of the N-particle wave function, and only the much simpler $\tilde{n}(\mathbf{r}, t; \mathbf{r}', t)$ is needed. Furthermore, if the operator O is diagonal in the position representation, i.e. $O(\mathbf{r}, \mathbf{r}') = O(\mathbf{r})\delta(\mathbf{r} - \mathbf{r}')$ (as for an external potential and its derivatives), the expectation value depends only on the diagonal part of the density matrix, i.e., the density of the system, $\tilde{n}(\mathbf{r}, t; \mathbf{r}, t) = \tilde{n}(\mathbf{r}, t)$.

If the system is in the ground state and a time-independent Hamiltonian is considered, as in Eq. (2.1), the *ground-state* density matrix and the density of the system (denoted here as $n(\mathbf{r}, t; \mathbf{r}', t)$ and $n(\mathbf{r}, t)$, respectively) do not depend on time, along with the expectation value of single-particle operators. It can be seen that if one is able to predict the ground state density

and density matrix *without* diagonalizing the many-body Hamiltonian or computing the N-particle ground-state wave function, single-particle observables can be easily calculated.

In this thesis, our aim is to go beyond the ground state and address the spectroscopic properties of materials. These processes involve adding or removing an electron at two different times and spaces while allowing for internal relaxation. A useful way to approach these problems is through the language of Green's functions. Since Green's functions are formulated within a second quantization framework, they provide a natural approach to address the addition and removal of *identical* particles.

As mentioned before, the diagonal of the density matrix gives the density of the system, which is the probability of finding an electron at position $\mathbf{r}$. The off-diagonal elements represent the probability of finding an electron at positions $\mathbf{r}$ and $\mathbf{r}'$ *at the same time.* [1] That said, the expression for the density matrix in second quantization is simply given by

$$n(\mathbf{r}, t; \mathbf{r}', t) = \langle GS|\hat{\psi}^\dagger(\mathbf{r}, t)\hat{\psi}(\mathbf{r}', t)|GS\rangle\,, \tag{2.4}$$

where the operator $\hat{\psi}(\mathbf{r}', t)$ destroys a particle at position $\mathbf{r}'$ and time t to the ground state (while $\hat{\psi}^\dagger$ creates a particle), and the *field operators* fulfill $\{\hat{\psi}(\mathbf{r}, t), \hat{\psi}^\dagger(\mathbf{r}', t)\} = i\delta(\mathbf{r} - \mathbf{r}')$. If we account for the time for the particle to move from $\mathbf{r}'$ to $\mathbf{r}$, we obtain the *one-particle Green's function* of the system:

$$iG(\mathbf{r}, t; \mathbf{r}', t') = \langle GS|\hat{\psi}(\mathbf{r}, t)\hat{\psi}^\dagger(\mathbf{r}', t')|GS\rangle\,\theta(t - t') - \langle GS|\hat{\psi}^\dagger(\mathbf{r}', t')\hat{\psi}(\mathbf{r}, t)|GS\rangle\,\theta(t' - t), \tag{2.5}$$

where we consider the possibility of first creating a particle at $\left|\mathbf{r}', t'\right\rangle$ and destroying it at $|\mathbf{r}, t\rangle$ or vice versa. The first term (without the theta) on the right-hand side is called the "addition" Green's function, $iG^> = \langle GS|\hat{\psi}(\mathbf{r}, t)\hat{\psi}^\dagger(\mathbf{r}', t')|GS\rangle$, and is related to the propagation of an electron inside the material. The other $-iG^< = \langle GS|\hat{\psi}^\dagger(\mathbf{r}', t')\hat{\psi}(\mathbf{r}, t)|GS\rangle$ is the "removal" Green's function and is the propagation of a hole. We will further justify this later on in the chapter. Since it is a complex quantity, the Green's function is not a physical observable of the system. Conversely, the real and imaginary parts separately are: in particular, the imaginary part of the Green's function is related to the photoemission spectrum of the system (see Sec. 2.7 for an in-depth discussion).

In a *non-interacting* system, we can write the addition Green's function on the eigenvectors of the Hamiltonian H as

$$iG^>_{0,ij} = \left\langle GS(t)\middle|\hat{a}_i e^{-i\hat{H}_0(t-t')}\hat{a}^\dagger_j\middle|GS(t')\right\rangle = e^{iE_N(t-t')}e^{-iE^i_{N+1}(t-t')}\delta_{ij} = e^{-i\epsilon^0_i(t-t')}\delta_{ij}\theta(\epsilon_i - \mu), \tag{2.6}$$

where we add the factor $\theta(\epsilon_i - \mu)$ to take into account that $G^>_{0,ij}$ is non-zero only for empty states. Thus, $-iG^>_0$ solves the "homogeneous" Schrödinger equation $(i\partial_t - h_0)G^>_0(t - t') = 0$, where h_0 is the single-particle Hamiltonian of the system. The removal Green's function

[1] This is a purely quantum property since, in classical mechanics, we either find a particle in $\mathbf{r}$ or in $\mathbf{r}'$.

solves the same equation but for occupied states. Since we want to solve the same equation for different time zones—specifically, we want to propagate electrons ($t > t'$) with $G_0^<$ and holes ($t < t'$) with $G_0^>$—we can combine the two solutions of the homogeneous equation with the theta function and obtain the Green's function for the system. Thus, the time-ordered non-interacting Green's function solves $(i\partial_t - h_0)G_0(t-t') = \delta(t-t')$ and is a Green's function for the non-interacting system.

In the thesis, we will deal with Green's functions in frequency space since it is the "natural" space for looking at the spectrum of a system. The Fourier transform of the time-ordered Green's function of Eq. (2.5) yields (see Appendix A.1 for details)

$$\begin{aligned} G(\mathbf{r},\mathbf{r}',\omega) = &\langle GS|\hat{\psi}(\mathbf{r})\frac{1}{\omega-(\hat{H}-E_{GS})+i\eta}\hat{\psi}^\dagger(\mathbf{r}')|GS\rangle \\ &+\langle GS|\hat{\psi}^\dagger(\mathbf{r}')\frac{1}{\omega-(E_{GS}-\hat{H})-i\eta}\hat{\psi}(\mathbf{r})|GS\rangle\,, \end{aligned} \tag{2.7}$$

where η is understood to always vanish, $\eta \to 0^+$. [2] We call the first term on the right-hand side the electron Green's function $G^{\mathrm{el}}(\omega)$ and the second term the hole Green's function $G^{\mathrm{hl}}(\omega)$. Importantly, we obtain the density matrix by the anti-Fourier transform:

$$n(\mathbf{r},\mathbf{r}') = \int \mathrm{d}\omega\, \frac{e^{i\omega 0^+}}{2\pi i} G(\mathbf{r},\mathbf{r}',\omega) = \int \mathrm{d}\omega\, \frac{e^{i\omega 0^+}}{2\pi i} \langle GS|\hat{\psi}^\dagger(\mathbf{r}')\frac{1}{\omega-(E_{GS}-\hat{H})-i\eta}\hat{\psi}(\mathbf{r})|GS\rangle\,, \tag{2.8}$$

which corresponds to integrating over the electronic (occupied) part only. Thus, obtaining the total number of particles in the system amounts to

$$N = \int \mathrm{d}\mathbf{r}\, n(\mathbf{r},\mathbf{r}) = \int \mathrm{d}\mathbf{r} \int \mathrm{d}\omega\, \frac{e^{i\omega 0^+}}{2\pi i} G(\mathbf{r},\mathbf{r}',\omega), \tag{2.9}$$

The *Lehmann representation* for the Green's function is obtained by inserting the projector over the eigenstates of the $(N+1)$-particle Hamiltonian for the addition Green's function and the projector over the eigenstates of the $(N-1)$-particle Hamiltonian for the removal Green's function. The Lehmann representation of the time-ordered propagator reads

$$\begin{aligned} G(\mathbf{r},\mathbf{r}',\omega) = &\sum_s \frac{\langle GS|\hat{\psi}(\mathbf{r})|s,N+1\rangle\,\langle s,N+1|\hat{\psi}^\dagger(\mathbf{r}')|GS\rangle}{\omega-\epsilon_s+i\eta} \\ &+\sum_s \frac{\langle GS|\hat{\psi}^\dagger(\mathbf{r}')|s,N-1\rangle\,\langle s,N-1|\hat{\psi}(\mathbf{r})|GS\rangle}{\omega-\epsilon_s-i\eta}, \end{aligned} \tag{2.10}$$

where $\epsilon_s = E^s_{N+1} - E_N > \mu$ for the electron-addition energies (first term), and $\epsilon_s = E_N - E^s_{N-1} < \mu$ for the removal energies (second term). The orbital $\phi_s(\mathbf{r}) = \langle s,N-1|\hat{\psi}(\mathbf{r})|GS\rangle$ is called the Dyson orbital and represents the probability for the removal process to happen, and the same

[2] We assume $\eta \to 0^+$ in all the equations of the thesis unless stated otherwise. Furthermore, for integrals like $\int \mathrm{d}\omega\, \frac{e^{i\omega 0^+}}{2\pi i}$, it is understood that $\int \mathrm{d}\omega\, \frac{e^{i\omega 0^+}}{2\pi i} = \lim_{\eta\to 0^+} \int \mathrm{d}\omega\, \frac{e^{i\omega\eta}}{2\pi i}$.

holds for the electron addition. Throughout the thesis, we refer to poles below the Fermi energy as occupied poles and above as empty poles. Note that this terminology is only inherited from single-particle (free or mean-field) theories. With interacting particles, "occupied" should be read as "less than the Fermi energy" or "above the real axis", while "unoccupied" should be read as "greater than the Fermi energy" or "below the real axis" (see Secs 2.5 and 2.7 for further discussions).

From its definition in Eq. (2.7) or the Lehmann representation of Eq. (2.10), at a fixed frequency ω, it is possible to consider $G(\mathbf{r},\mathbf{r}',\omega)$ as the representation, in the position basis, of an operator $G(\omega)$ acting on the one-particle Hilbert space, i.e., $G(\mathbf{r},\mathbf{r}',\omega) = \langle \mathbf{r} | G(\omega) | \mathbf{r}' \rangle$. A rotation in the Fock space, $\hat{\psi}^\dagger(\mathbf{r}) = \sum_n \langle n|\mathbf{r}\rangle \hat{c}_n^\dagger$, induces the same change of representation for the operator $G(\omega)$. To see this, we take $G^{\mathrm{el}}(\omega)$ for simplicity and write

$$\begin{aligned} G^{\mathrm{el}}(\mathbf{r},\mathbf{r}',\omega) &= \langle GS|\hat{\psi}(\mathbf{r})\frac{1}{\omega-(\hat{H}-E_{GS})+i\eta}\hat{\psi}^\dagger(\mathbf{r}')|GS\rangle \\ &= \sum_{n,n'} \langle \mathbf{r}|n\rangle \langle GS|\hat{c_n}\frac{1}{\omega-(\hat{H}-E_{GS})+i\eta}\hat{c_{n'}}^\dagger|GS\rangle \langle n'|\mathbf{r}'\rangle = \sum_{n,n'} \langle \mathbf{r}|n\rangle G^{\mathrm{el}}_{nn'}(\omega) \langle n'|\mathbf{r}'\rangle, \end{aligned} \tag{2.11}$$

where indeed $\langle \mathbf{r}|n\rangle$ represents the change of basis in the one-particle Hilbert space. The same analysis holds for $G^{\mathrm{hl}}(\omega)$ and thus for $G(\omega)$.

Conveniently, using the fact mentioned above, it is possible to rewrite propagators as acting on the one-particle Hilbert space. For example, the the Lehmann representation of the Green's function of Eq. (2.10) can be rewritten as:

$$G(\omega) = \sum_s \frac{|\phi_s\rangle\langle\phi_s|}{\omega-\epsilon_s+i\eta\,\mathrm{sgn}(\epsilon_s-\mu)}, \tag{2.12}$$

where $|\phi_s\rangle$ are the Dyson orbitals of the system. Using the completeness of $|s,N+1\rangle$ and $|s,N-1\rangle$, one can see that the Dyson orbitals span the entire one-particle Hilbert space, $\sum_s |\phi_s\rangle\langle\phi_s| = 1$. Their number is equal to all the possible excitations of the $N+1$ and $N-1$ system—infinitely many in the thermodynamic limit—, and thus, the Dyson orbitals cannot be orthogonal or linearly independent.

A very important quantity directly related to the Green's function is the spectral function of the system, which is defined as

$$A(\mathbf{r},\mathbf{r}',\omega) = \sum_s \phi_s(\mathbf{r})\phi_s^*(\mathbf{r}')\delta(\omega-\epsilon_s), \tag{2.13}$$

and is related to the Green's function through

$$A(\omega) = \frac{1}{\pi}\mathrm{sgn}(\omega-\mu)\,\mathrm{Im}G(\omega), \tag{2.14}$$

where the imaginary part of the matrix G is given by $\mathrm{Im}G(\omega) = \frac{1}{2i}\left[G(\omega)-G^\dagger(\omega)\right]$.

Importantly, the sum rule for the normalization of the spectral function is given by

$$\int \mathrm{d}\omega\, A(\omega) = I, \tag{2.15}$$

which follows from the completeness relation of the Dyson orbitals, $\sum_s |\phi_s\rangle\langle\phi_s| = I$. Additionally, by combining Eq. (2.8) with the definition of the spectral function in Eq. (2.13), it is possible to obtain the density matrix of the system:

$$n(\mathbf{r},\mathbf{r}') = \int \mathrm{d}\omega\, \frac{e^{i\omega 0^+}}{2\pi i} G(\mathbf{r},\mathbf{r}',\omega) = \sum_s \int \mathrm{d}\omega\, \frac{e^{i\omega 0^+}}{2\pi i} \frac{\phi_s(\mathbf{r})\phi_s^*(\mathbf{r}')}{\omega - \epsilon_s + i\eta\,\mathrm{sgn}(\epsilon_s - \mu)} = \int_{-\infty}^{\mu} \mathrm{d}\omega\, A(\mathbf{r},\mathbf{r}',\omega). \tag{2.16}$$

Using Eq. (2.9), the number of particles is found to be

$$N = \int_{-\infty}^{\mu} \mathrm{d}\omega\ \mathrm{Tr}\, A(\omega)., \tag{2.17}$$

where Tr denotes the trace operation.

Differently from the one-particle non-interacting Green's function G_0, the *one-particle* Green's function G is *not* a Green's function for the interacting system since it does not satisfy $(i\partial_t - H)G(t-t') = \delta(t-t')$, or equivalently $(I\omega - H)G(\omega) = I$ in Fourier space. We can define the "total" Green's function for the system as

$$G_{\mathrm{tot}}(\omega) = (\omega - H)^{-1}, \tag{2.18}$$

which can be made time-ordered by adding $\pm i\eta$.

2.2 Embedding and self-energy

Let us suppose we have a system S embedded in a bath B. The two systems S and B interact with each other via a coupling Hamiltonian H_{SB}. The Schrödinger equation for the total Green's function, Eq. (2.18), can be written as:

$$\begin{pmatrix} I_S\omega - H_S & H_{SB} \\ H_{BS} & I_B\omega - H_B \end{pmatrix} \begin{pmatrix} G_S & G_{SB} \\ G_{BS} & G_B \end{pmatrix} = \begin{pmatrix} I_S & 0 \\ 0 & I_B \end{pmatrix} \tag{2.19}$$

This is a system of four equations and four variables. Focusing on the two equations:

$$(I_S\omega - H_S)\, G_S + H_{SB} G_{BS} = I_S, \tag{2.20}$$

$$H_{BS} G_S + (I_B\omega - H_B)\, G_{BS} = 0, \tag{2.21}$$

we can use the second to rewrite the first, resulting in:

$$G_S^{-1}(\omega) = I\omega - H_S - H_{SB} \frac{1}{\omega I_B - H_B} H_{BS}. \tag{2.22}$$

By introducing the self-energy for the system S, $\Sigma_S(\omega) = H_{SB}\,(I\omega_B - H_B)^{-1}\,H_{BS}$, we arrive at the *Dyson equation*:

$$G_S^{-1}(\omega) = G_0^{-1}(\omega) - \Sigma(\omega), \tag{2.23}$$

where $G_0^{-1}(\omega) = \omega - H_S$ is the propagator for the system S decoupled from the bath. In the thesis, we will analyze this equation in depth. Here, we limit the discussion to saying that solving Eq. (2.23) is not equivalent to solving the full system, i.e. Eq. (2.19). Indeed, the knowledge of the exact self-energy $\Sigma(\omega)$ is sufficient to obtain the exact Green's function of system S (we always assume that we know $G_0(\omega)$), but not enough to obtain G_{tot} since we have discarded Eq. (2.21) in the process. In fact, with Eq. (2.21) and the hypothesis of the hermiticity of the coupling, we can reconstruct G_{tot}.

Moving to the *one-particle* Green's function, the above construction can be used to embed a mean-field electron—an electron subject to a mean field—in the sea of the other $N-1$ electrons. The Hamiltonian for the system H_S is a mean-field Hamiltonian, i.e., the kinetic energy plus the external potential created by the background of nuclei, the Hartree term [39], and others if needed. In this way, we are specializing in the Dyson equation for the one-particle Green's function:

$$G^{-1}(\omega) = G_0^{-1}(\omega) - \Sigma(\omega), \tag{2.24}$$

where, as stated already, $G_0(\omega)$ comes from a mean-field approximation of the electronic problem, and the self-energy $\Sigma(\omega)$ takes care of all the "rest" of the correlation. From this approach, it is clear why we need a frequency-dependent self-energy to accurately describe correlations.

The Dyson equation can be seen as a geometric summation as

$$G(\omega) = G_0(\omega) + G_0(\omega)\Sigma(\omega)G_0(\omega) + G_0(\omega)\Sigma(\omega)G_0(\omega)G_0(\omega)\Sigma(\omega)G_0(\omega) + \dots. \tag{2.25}$$

Furthermore, the Dyson equation can be seen as a Volterra equation for G:

$$G(\omega) = G_0(\omega) + G_0(\omega)\Sigma(\omega)G(\omega), \tag{2.26}$$

together with its adjoint:

$$G(\omega) = G_0(\omega) + G(\omega)\Sigma(\omega)G_0(\omega). \tag{2.27}$$

It is useful to perform the anti-Fourier transform of the Dyson equation. Specifying the real-space indexes, and using a compact notation, $1 = (\mathbf{r}_1, t_1)$, the equations above can be written as

$$\begin{aligned} G(1,2) &= G_0(1,2) + G_0(1,3)\Sigma(3,4)G(4,2), \\ G(1,2) &= G_0(1,2) + G(1,3)\Sigma(3,4)G_0(4,2), \end{aligned} \tag{2.28}$$

where repeated contiguous indexes are summed over. By subtracting the second equation

from the first, one obtains [3]

$$G_0^{-1}(1,2)G(2,1^+) - G(1,2)G_0^{-1}(2,1^+) = \Sigma(1,4)G(4,1^+) - G(1,3)\Sigma(3,1^+). \tag{2.29}$$

Recalling that $G_0^{-1}(1,2) = \left(i\partial_{t_1} - h\right)\delta(t_1 - t_2)$—since it is defined by $(i\partial_t - h_0)G_0(t-t') = \delta(t-t')$— the equation above simplifies to

$$\left[i\left(\partial_{t_1} + \partial_{t_{1^+}}\right) + \frac{1}{2}\left(\nabla_1^2 - \nabla_{1^+}^2\right)\right] G(1,1^+) = \Sigma(1,4)G(4,1^+) - G(1,3)\Sigma(3,1^+), \tag{2.30}$$

where the external potential in h was dropped since it is diagonal and continuous in the limit $1 = 1^+$. Calling $t_1 \to t$ and $\mathbf{r}_1 \to \mathbf{r}$, the first term on the LHS of the equation above is:

$$i\left(\partial_t + \partial_{t^+}\right) G(\mathbf{r}, t; \mathbf{r}^+, t^+) = \left(\partial_t + \partial_{t^+}\right)\left\langle \hat{\psi}^\dagger(\mathbf{r}, t)\hat{\psi}(\mathbf{r}^+, t^+)\right\rangle = \frac{\partial n(\mathbf{r}, t)}{\partial t}, \tag{2.31}$$

and the second term is:

$$\frac{1}{2}\left(\nabla^2 - \nabla^{+2}\right) G(\mathbf{r}, t; \mathbf{r}^+, t^+) = \frac{1}{2}\left(\nabla + \nabla^+\right)\cdot\left(\nabla - \nabla^+\right) G(\mathbf{r}, t; \mathbf{r}^+, t^+) = \nabla\cdot\mathbf{J}(\mathbf{r}, t) \tag{2.32}$$

where $\mathbf{J}(\mathbf{r}, t) = -\frac{1}{2}\left(\nabla - \nabla^+\right) G(\mathbf{r}, t; \mathbf{r}^+, t^+)$ represents the current. Finally, if the source term $\Sigma(1,4)G(4,1^+) - G(1,3)\Sigma(3,1^+) = 0$, then Eq. (2.30) becomes:

$$\frac{\partial n(\mathbf{r}, t)}{\partial t} + \nabla\cdot\mathbf{J}(\mathbf{r}, t) = 0, \tag{2.33}$$

which is known as the "continuity" equation.

Eq. (2.33) is fundamental in field theories. When integrated, it ensures the conservation of the number of particles between G_0 and G. Indeed, by switching on interactions, the number of particles cannot change, and if G_0 obeys the continuity equation—which can be easily proven by writing down the equation of motion for G_0 and the adjoint—so must G.

When Σ results from the derivative of a (scalar) functional of the Green's function, which is invariant under scalar gauge transformations, i.e.

$$\frac{\delta\Phi[G]}{\delta G(2,1^+)} = \Sigma(1,2), \tag{2.34}$$

the source term

$$\int \mathrm{d}2\ \Sigma(1,2)G(2,1^+) - G(1,2)\Sigma(2,1^+) \tag{2.35}$$

is zero. Indeed, the invariance of Φ implies $\delta\Phi = 0 = \Sigma(1,2)\,\delta G(2,1^+)$, where the variation corresponds to $G(1,2) \to e^{i\Lambda(1)}G(1,2)e^{-i\Lambda(1)}$ for any scalar function Λ. Then,

$$\int \mathrm{d}1\,\mathrm{d}2\ \Lambda(1)\left[\Sigma(1,2)G(2,1^+) - G(1,2)\Sigma(2,1^+)\right] = 0, \tag{2.36}$$

[3] $1^+ = (\mathbf{r}_1, t_1^+) = \lim_{\eta_1\to 0^+}(\mathbf{r}_1, t_1 + \eta_1)$

which yields the condition in Eq. (2.35) for the arbitrariness of Λ. If a functional is diagrammatic, i.e., it can be written as a diagrammatic expansion, this gauge invariance is guaranteed. Since at each vertex of the diagram, labeled by $(\mathbf{r_1}, t_1)$, there is an incoming $G(\ldots;1^+)$ and an outgoing $G(1;\ldots)$, internal phases like $e^{i\Lambda(1)}$ cancel out. Since Φ is a scalar, diagrams have to be closed "bubbles", and consequently, all phases cancel out and the continuity equation is fulfilled. Similarly to what has been shown above, diagrammatic functional theories also provide the conservation of linear and angular momentum, total energy, and particle-hole symmetry. Those go beyond the scope of this thesis so are not treated here. In a later chapter, we will use the argument above to show that even if not diagrammatic the so-called dynamical Hubbard functional preserves particle symmetry.

2.3 Energy functionals

As seen before, the solution to the many-body problem via diagonalization of the N-particle Hamiltonian is a formidable task, providing not only the ground-state wave function of the system, but also all neutral excitations. To simplify the problem, we may rewrite it in terms of the density $n(\mathbf{r})$, the density matrix $n(\mathbf{r},\mathbf{r}')$, and the two-particle pair-correlation function $n_2(\mathbf{r},\mathbf{r}')$, and minimize the energy functional

$$E = \int \mathrm{d}\mathbf{r} \lim_{\mathbf{r}'\to\mathbf{r}} \left(-\frac{\nabla^2}{2} n(\mathbf{r},\mathbf{r}')\right) + \frac{1}{2}\int \mathrm{d}\mathbf{r}\,\mathrm{d}\mathbf{r}' \frac{n_2(\mathbf{r},\mathbf{r}')}{|\mathbf{r}-\mathbf{r}'|} + \int \mathrm{d}\mathbf{r}\, n(\mathbf{r})\, v_{\mathrm{ext}}(\mathbf{r}). \tag{2.37}$$

To obtain the equation above, it is sufficient to write the Hamiltonian in Eq. (2.1) in second quantization

$$\hat{H} = \int \mathrm{d}\mathbf{r}\, \hat{\psi}^\dagger(\mathbf{r},t)\left(-\frac{\nabla^2}{2} + v_{\mathrm{ext}}(\mathbf{r})\right)\hat{\psi}(\mathbf{r},t) + \frac{1}{2}\int \mathrm{d}\mathbf{r}\,\mathrm{d}\mathbf{r}'\, \hat{\psi}^\dagger(\mathbf{r}',t)\hat{\psi}^\dagger(\mathbf{r},t)\frac{1}{|\mathbf{r}-\mathbf{r}'|}\hat{\psi}(\mathbf{r},t)\hat{\psi}(\mathbf{r}',t), \tag{2.38}$$

and take the expectation value over the ground-state wave function to get the total energy, $E = \langle GS|\hat{H}|GS\rangle$. Finally, Eq. (2.37) holds by recognizing the three aforementioned quantities: the density matrix $n(\mathbf{r},\mathbf{r}') = \langle GS|\hat{\psi}^\dagger(\mathbf{r}',t)\hat{\psi}^\dagger(\mathbf{r},t)|GS\rangle$, the density $n(\mathbf{r}) = n(\mathbf{r},\mathbf{r})$, and the two-particle pair-correlation function

$$n_2(\mathbf{r},\mathbf{r}') = \langle GS|\hat{\psi}^\dagger(\mathbf{r}',t)\hat{\psi}^\dagger(\mathbf{r},t)\hat{\psi}(\mathbf{r},t)\hat{\psi}(\mathbf{r}',t)|GS\rangle\,. \tag{2.39}$$

Although the reduction in complexity provided by the minimization of the energy functional in Eq. (2.37) is impressive, the procedure is still impractical due to the constraints that have to be imposed on the variables.

On this matter, one should recall that the quantities $n(\mathbf{r},\mathbf{r}')$, $n(\mathbf{r})$, and $n_2(\mathbf{r},\mathbf{r}')$ are contractions of $\Psi^*(\mathbf{r}'_1,\ldots,\mathbf{r}'_N)\Psi(\mathbf{r}_1,\ldots,\mathbf{r}_N)$, which, e.g., integrates to N and must originate from an antisymmetric wave function.

For example, how to impose this latter N-representability condition on $n_2(\mathbf{r},\mathbf{r}')$ is a matter of

current research [40].

The simplest of the three variables is the density. Apart from depending only on $\mathbf{r}$, it has been found that its "N" representability conditions are that it should integrate to N, with its gradient being normalizable, and that it should be positive [41]. The problem is that the total electronic energy E is not readily a functional of the density. Nevertheless, it can be shown that (for non-degenerate ground states) there is an invertible map between the density, the N-particle wave function, and the external potential, i.e., $n(\mathbf{r}) \longleftrightarrow v_{\text{ext}}(\mathbf{r}) \longleftrightarrow |\Psi\rangle$. This means that if one takes a random wave function, $\left|\Psi'\right\rangle \longleftrightarrow n'(\mathbf{r})$, it is valid that

$$E' = \left\langle \Psi' \middle| H \middle| \Psi' \right\rangle = \left\langle \Psi'[n'] \middle| H \middle| \Psi'[n'] \right\rangle > E. \tag{2.40}$$

In other words, this shows that the total energy $E[n]$ is variational with respect to the density, i.e., $E[n] = E_{\text{GS}} \iff n(\mathbf{r})$ is the ground-state density of the system. The one-to-one relationship between the wave function and the density, together with the reformulation of the variational principle in terms of the density, constitutes the content of the Hohenberg-Kohn theorems [9].

It is natural to divide the energy functional into

$$E[n] = T[n] + W[n] + \int \mathrm{d}\mathbf{r}\, v_{\text{ext}}(\mathbf{r}) n(\mathbf{r}), \tag{2.41}$$

where the first two addends sum to the internal energy of the system, and the last is the coupling between the density and the external potential. The price to pay for reducing the problem of finding the ground state of the system to the minimization of a functional of the density is the explicit form of the functional. While $\langle\Psi|H|\Psi\rangle$ is explicit in $|\Psi\rangle$, one does not know the form for the kinetic energy $T[n]$ and the interaction energy $W[n]$. A huge simplification is brought by Kohn and Sham [42], who suppose that for each physical (N-representable) density, there is an external potential that reproduces them in a non-interacting system (v-representability condition), the so-called Kohn and Sham system. Then, the total energy is rewritten as

$$E[n] = T_0[n] + E_{\text{Hxc}}[n] + \int \mathrm{d}\mathbf{r}\, v_{\text{ext}}(\mathbf{r}) n(\mathbf{r}), \tag{2.42}$$

where T_0 is the internal energy, and $E_{\text{Hxc}}[n]$ is split into the electrostatic contribution to the internal energy $E_H[n] = \frac{1}{2}\int \mathrm{d}\mathbf{r}\,\mathrm{d}\mathbf{r}' \frac{n(\mathbf{r})n(\mathbf{r}')}{|\mathbf{r}-\mathbf{r}'|}$ and the rest, $E_{\text{Hxc}}[n] = E_{\text{H}}[n] + E_{\text{xc}}[n]$. Since the minimization is performed by varying the density of *non-interacting* systems, $n(\mathbf{r}) = \sum_i \left|\phi_i(\mathbf{r})\right|^2$, where the sum is performed over the occupied states, the minimization of $E[n]$ is equivalent to solving

$$h_{\text{KS}}[n]\phi(\mathbf{r}) = \left(-\frac{\nabla^2}{2} + v_{\text{ext}}(\mathbf{r}) + \int \mathrm{d}\mathbf{r}' \frac{n(\mathbf{r}')}{|\mathbf{r}-\mathbf{r}'|} + v_{\text{xc}}[n](\mathbf{r})\right)\phi(\mathbf{r}) = \epsilon_{KS}\phi(\mathbf{r}), \tag{2.43}$$

where $h_{\text{KS}}[n] = \frac{\delta E}{\delta n}$.[4] In other words, one can minimize with respect to each of the N-orbitals

[4] Note that the functional derivative is not constrain to have particle fixed. Indeed, with the variationality

$\phi_i^*(\mathbf{r})$ the functional $E[\phi_1, \phi_1^*, \ldots] - \sum_{i=1}^N \lambda_i \left(\langle \phi_i | \phi_i \rangle - 1\right)$, and the stationarity condition—or Euler equation—for the problem gives Eq. (2.43).

Up to now, only a rewriting of the entire problem has been presented. In fact, an explicit functional that can be minimized requires the explicit form for $E_{\mathrm{xc}}[n]$. Describing the numerous approximations and exact constraints in the exchange-correlation functionals employed in computational materials science is beyond the scope of this thesis. The DFT calculations in this thesis employ $E_{\mathrm{xc}}[n]$ from the Perdew-Burke-Ernzerhof exchange-correlation functional [10].

It is natural to ask whether one can build a variational energy functional for the one-particle Green's function $G(\mathbf{r}, \mathbf{r}', \omega)$. This was accomplished by Luttinger and Ward in Ref. [19], and subsequently by Klein [19] (see Appendix A.3 for details). To illustrate this, one can start with the expression for the energy as the *integration of the coupling constant*,

$$E = E_0 + \int_0^1 \frac{\mathrm{d}\lambda}{\lambda} \langle \Psi_\lambda | \lambda V_{\mathrm{ee}} | \Psi_\lambda \rangle , \tag{2.44}$$

which follows directly from the Hellmann-Feynman theorem, $\frac{\mathrm{d}E}{\mathrm{d}\lambda} = \frac{1}{\lambda} \langle \Psi_\lambda | \lambda V_{\mathrm{ee}} | \Psi_\lambda \rangle$, for a Hamiltonian $H = H_0 + \lambda V_{\mathrm{ee}}$.

It is possible to rewrite the interaction term in Eq. (2.44). We can start by writing the equation of motion for the field operator

$$i\partial_t \hat{\psi}(\mathbf{r}, t) = h_0(\mathbf{r}) \hat{\psi}(\mathbf{r}, t) + \int \mathrm{d}\mathbf{r}' \, v_{\mathrm{c}}(\mathbf{r}, \mathbf{r}') \hat{\psi}^\dagger(\mathbf{r}', t) \hat{\psi}(\mathbf{r}', t) \hat{\psi}(\mathbf{r}, t), \tag{2.45}$$

which solves the Heisenberg equation for the operators $i\dot{\hat{\psi}}(\mathbf{r}, t) = \left[\hat{\psi}(\mathbf{r}, t), \hat{H}\right]$. Then, multiplying by $\int \mathrm{d}\mathbf{r} \, \hat{\psi}^\dagger(\mathbf{r}, t)$ on the left, and bracketing with the ground state of the system $\langle GS | \cdot | GS \rangle$, we find:

$$2 \langle V_{\mathrm{ee}} \rangle = \int \mathrm{d}\mathbf{r} \lim_{\substack{t' \to t^+ \\ \mathbf{r}' \to \mathbf{r}}} \left[\partial_t + i h_0(\mathbf{r})\right] G(\mathbf{r}, t; \mathbf{r}', t') = \int \mathrm{d}\mathbf{r} \lim_{\mathbf{r}' \to \mathbf{r}} \int \mathrm{d}\omega \, \frac{e^{i\omega 0^+}}{2\pi i} \left(\omega - h_0(\mathbf{r})\right) G(\mathbf{r}, \mathbf{r}', \omega). \tag{2.46}$$

Thus,

$$\langle \Psi_\lambda | \lambda V_{\mathrm{ee}} | \Psi_\lambda \rangle = \frac{1}{2} \int \mathrm{d}\omega \, \frac{e^{i\omega 0^+}}{2\pi i} \mathrm{Tr}\{(\omega - h_0) G_\lambda\} = \frac{1}{2} \int \mathrm{d}\omega \, \frac{e^{i\omega 0^+}}{2\pi i} \mathrm{Tr}\{\Sigma_\lambda(\omega) G_\lambda(\omega)\}, \tag{2.47}$$

where in the last equality, we have used that $G_0^{-1} = \omega - h_0$, and the Dyson equation for the exact Green's function interacting with a coupling constant λ, $G_\lambda^{-1} = G_0^{-1} - \Sigma_\lambda$.

should be imposed on the functional $E[n] - \mu \int \mathrm{d}\mathbf{r} \, n(\mathbf{r})$, with μ a Lagrange multiplier and also equal to the chemical potential of the system.

To further our analysis, we can expand the self-energy in λ as follows:

$$\Sigma(\omega) = \sum_n \lambda^n \Sigma^{(n)}[G_\lambda, v_c](\omega), \tag{2.48}$$

Note that the dependence on λ has been extracted only from the Coulombic potential and not from the Green's function. This expansion, however, is not a standard Taylor expansion. Instead, it is related to a "dressed-propagator" expansion of the total energy with respect to the interaction. The idea of expanding the interaction energy $(E - E_0)$ in terms of the Green's function of the system originates from Luttinger and Ward's seminal paper [19] in particle physics.

In the paper, Feynman rules are derived for diagrammatic perturbation theory in the context of a two-particle interacting fermionic system. Here, we assume the Feynman rules to be valid. In the expansion of the two-point propagator G with respect to the electric charge e^2, the n-th order term is the sum of all possible ways to connect the two points using $2n$ vertices. Each vertex has a non-interacting propagator in G_0^{in} and out G_0^{out}, and an interaction line v_c. These n-th order diagrams can be categorized into two groups: those that by cutting a continuous (G_0) line give two lower-order propagator diagrams (improper), and those that do not (proper).

An improper diagram is always given by

$$G_0 \Sigma G_0, \tag{2.49}$$

where we have called the internal part Σ. Then, the entire propagator can be written as

$$G = G_0 + G_0 \Sigma G_0 + G_0 \Sigma G_0 \Sigma G_0 + \dots, \tag{2.50}$$

which, when summed, gives the Dyson equation and shows that Σ is equal to the self-energy of the system. Furthermore, from Eq. (2.49), one can see that an n-th order diagram $\Sigma^{(n)}$ for the self-energy is a closed loop (bubble) diagram with a continuous line removed. Calling skeletonic the diagrams formed with propagators that do not contain bubbles inside (i.e., the ones formed only with G_0), the self-energy (which has to contain those plus the ones that have) can be written as *the sum of all possible diagrams with G_0 replaced by G.*

What we have explained in the last paragraph is exactly the expansion of the self-energy in Eq. (2.48). $\Sigma^{(n)}[G_\lambda, v_c]$ is the skeletonic diagram of order n for the self-energy. This piece is crucial since it can be seen that $\Sigma^{(n)}$ does not depend on G_0; we have traded it to have a skeletonic partition of the diagrams. By combining Eq. (2.44) with Eq. (2.47) and Eq. (2.48), the total energy of the system reads

$$E = E_0 + \sum_n \int_0^1 \mathrm{d}\lambda \, \frac{\lambda^n}{2} \mathfrak{Tr}\left[\Sigma^{(n)}[G_\lambda, v_c] G_\lambda\right], \tag{2.51}$$

where $\mathfrak{Tr} = \int \mathrm{d}\omega \, \frac{e^{i\omega 0^+}}{2\pi i}$.

Using integration by parts,

$$E = E_0 + \Phi[G] - \sum_n \int_0^1 \mathrm{d}\lambda \frac{\lambda^n}{2n} \frac{\mathrm{d}}{\mathrm{d}\lambda} \mathfrak{Tr}\left[\Sigma^{(n)}[G_\lambda, v_c] G_\lambda\right]. \tag{2.52}$$

The term

$$\Phi[G] = \sum_n \frac{1}{2n} \mathfrak{Tr}\left[G\Sigma^{(n)}[G, v_c]\right], \tag{2.53}$$

is termed the Φ functional.

The beauty is that

$$\frac{\delta\Phi}{\delta G} = \Sigma\,. \tag{2.54}$$

To see this, first consider deriving a self-energy skeleton diagram of order n, $\Sigma^{(n)}$, with respect to G. Since there are $2n$ vertices each paired with two Green's functions, there must be $2n-1$ (dressed) Green's functions connecting the points—recall that $\Sigma^{(n)}$ comes from a closed linked bubble with $2n$ Green's functions, where one has removed a line. In the bubble, there are $2n-1$ ways of removing a line, all giving the same diagram D^n, thus $\Sigma^n = GD^n$. Counting correctly the multiplicities, the operation of removing a line is equivalent to a derivative. Indeed, in position representation, skeletonic diagrams are (matrix) polynomials of G. Thus, using the Leibniz rule, $\frac{\delta\Sigma^{(n)}}{\delta G} = (2n-1)D^n$.

This said, the derivative of the Φ functional reads

$$\frac{\delta\Phi}{\delta G} = \sum_n \frac{1}{2n}\left[\Sigma^{(n)} + G\frac{\delta\Sigma^{(n)}}{\delta G}\right] = \Sigma, \tag{2.55}$$

where the equality line is obtained by summing and using Eq. (2.48) at full interaction, $\lambda = 1$

For the same reasons, the second term of Eq. (2.52) can be rewritten

$$\begin{aligned}
\sum_n \int_0^1 \mathrm{d}\lambda \frac{\lambda^n}{2n} \frac{\mathrm{d}}{\mathrm{d}\lambda} \mathfrak{Tr}\left[\Sigma^{(n)}[G_\lambda, v_c] G_\lambda\right] &= \sum_n \int_0^1 \mathrm{d}\lambda \frac{\lambda^n}{2n} \mathfrak{Tr}\left[\frac{\mathrm{d}G_\lambda}{\mathrm{d}\lambda}\left(\frac{\delta\Sigma_\lambda^{(n)}}{\delta G_\lambda} G_\lambda + \Sigma_\lambda^{(n)}\right)\right] \\
&= \int_0^1 \mathrm{d}\lambda\, \mathfrak{Tr}\left[\Sigma_\lambda \frac{\mathrm{d}G_\lambda}{\mathrm{d}\lambda}\right] \\
&= \mathfrak{Tr}\left[\Sigma_\lambda G_\lambda\right] - \int_0^1 \mathrm{d}\lambda\, \mathfrak{Tr}\left[\frac{\mathrm{d}\Sigma_\lambda}{\mathrm{d}\lambda} G_\lambda\right],
\end{aligned} \tag{2.56}$$

where in the last equality, integration by parts has been used. Taking advantage of the Dyson equation at each λ, one can rewrite the full energy *Luttinger-Ward-Klein* functional as

$$E = E_0 + \Phi[G] - \mathfrak{Tr}\left[\Sigma[G]G\right] + \mathfrak{Tr}\ln\left(1 - G_0\Sigma[G]\right). \tag{2.57}$$

Taking into account Eq. (2.54), the derivative of the LW functional yields

$$\frac{\delta E}{\delta G} = -\frac{\delta \Sigma}{\delta G}\left[G - (1 - G_0\Sigma)^{-1} G_0\right], \tag{2.58}$$

and the stationary condition $\frac{\delta E}{\delta G} = 0$ gives the Dyson equation,

$$G^{-1} = G_0^{-1} - \Sigma[G]. \tag{2.59}$$

Thus, the LW functional is stationary when G, G_0, and Σ obey the Dyson equation, assuring that if the self-energy is the derivative of a Φ functional, the self-consistent solution of the Dyson equation (2.59) comes from a variational principle. Also, as shown in Sec. 2.2, if Φ is written in a diagrammatic way—following Feynman's rules—, then G that solves the Dyson equation (2.59) obeys several conservation laws.[5] n passing, it is relevant to note that the Dyson equation is not obeyed during the stationarization of the functional; instead, it is by obeying the Dyson equation that the functional becomes stationary.

It is interesting to compare the Luttinger-Ward functional with the energy functional of density functional theory. From Eq. (2.41), the DFT functional can be rewritten as

$$E[n] = E_{\text{Hxc}}[n] - \int \mathrm{d}\mathbf{r}\, v_{\text{Hxc}}(\mathbf{r})\, n(\mathbf{r}) + E_{\text{KS}}[n], \tag{2.60}$$

where one has summed and subtracted $\int \mathrm{d}\mathbf{r}\, v_{\text{Hxc}}(\mathbf{r})\, n(\mathbf{r})$ to get the energy of the (non-interacting) Kohn and Sham system E_{KS}. Simply rewriting the two equations with the terms aligned can help the analysis:

$$\begin{array}{ccccccc} E[n] & = & E_{\text{Hxc}}[n] & - & \int \mathrm{d}\mathbf{r}\, v_{\text{Hxc}}(\mathbf{r})\, n(\mathbf{r}) & + & E_{\text{KS}}[n] \\ E[G] & = & \Phi[G] & - & \mathfrak{Tr}\,[\Sigma[G]G] & + & E_0 + \mathfrak{Tr}\ln(1 - G_0\Sigma[G]). \end{array} \tag{2.61}$$

As said, the DFT functional is a functional of the electron density, while the LW functional is a functional of the one-particle Green's function. The Hartree-exchange-correlation term of DFT, E_{Hxc}, is replaced by the Φ functional in the LW. The term contains all the (exchange and) correlation effects of the system and has to be approximated. While the functional form of the exchange correlation functional is unknown, Φ as a functional of the Green's function (and the bare interaction) is known perturbativelydiagrammatically—as seen before, for a given order of the approximation one must draw all the bubble skeletonic diagrams following Feynman rules and replacing the non-interacting propagator with the Green's function G. The terms E_{KS} and $E_0 + \mathfrak{Tr}\ln(1 - G_0\Sigma[G])$ are the energy of the non-interacting Kohn and Sham system, and the energy of a system having a Green's function G *taken as if it were non-interacting*, since at the variational point, it holds $E_0 + \mathfrak{Tr}\ln(1 - G_0\Sigma[G]) = \mathfrak{Tr}\ln G$, as shown in Appendix A.3. Finally, the terms $\int \mathrm{d}\mathbf{r}\, v_{\text{Hxc}}(\mathbf{r})\, n(\mathbf{r})$ and $\mathfrak{Tr}\,[\Sigma[G]G]$ remove a double counting of the interaction.

[5] Though in Sec. 2.2, only the continuity equation is proven, one can show that also conservation of linear and angular momentum, along with the total energy, are respected by G.

Having analyzed the functional, we now focus on its derivative, the Dyson equation (2.59). This is an equation that can be solved self-consistently once the functional form $\Sigma[G]$, or equivalently of $\Phi[G]$, is determined. The same thing happens for the potential $v_{\mathrm{Hxc}}[n]$ in DFT. As soon as its dependence with respect to the density is known, one can solve the Kohn and Sham Eq. (2.43) self-consistently. Thus, as seen in the previous sections, *the Dyson equation replaces a Schrödinger-type equation in the context of Green's functions.*

Up to now, a perturbative diagrammatic theory has been used to construct Φ.However, this is not strictly necessary. Indeed, if we consider Σ as the derivative of the Φ functional, it is enough to guarantee the stationarity condition and, hence, the Dyson equation for G. Since it is not diagrammatic, one cannot be assured to have, for example, the continuity equation fulfilled. In the thesis, a *novel approximation* to the Φ functional is introduced, and particle conservation for the functional is also discussed.

2.4 Green's function theories vs linear response

In this section, we compare the dynamical origin of Green's functions with the frequency dependence of linear response quantities. It is argued that although both are dynamical frameworks, the frequency dependence has a very different origin.

In linear response, we are interested in the time evolution of states governed by a *time-dependent* Hamiltonian of the (second-quantized) form

$$\hat{H}(t) = \hat{H}_0 + F(t)\hat{B}, \tag{2.62}$$

where F is a scalar (time-dependent) coupling between $\hat{H}_0$ and $\hat{B}$.

Contrary to what happens for Green's function theory, in which one derives the propagator to compute expectation values of operators, in linear response, we focus directly on the operator for which we need the expectation values. Since this thesis does not focus on linear response, the full derivation of linear-response theory is referred to one of the many textbooks, e.g., Refs [20, 43].

The linear response function in (the Heisemberg picture in) time domain is

$$\chi(1,2) = -i\theta(t_1 - t_2)\langle GS|\left[\hat{A}(1), \hat{B}(2)\right]|GS\rangle \,., \tag{2.63}$$

where θ is the Heaviside step function. The Fourier transform in time of this object reads

$$\chi(\omega) = \sum_{nm} \frac{P_n - P_m}{\omega - \omega_{nm} + i\eta} A_{mn}B_{nm}, \tag{2.64}$$

where $\omega_{nm} = E_n^N - E_m^N$, and P_n is equal to 1 for the occupied states and 0 for the unoccupied ones (at zero temperature). Here, E_n^N are the energies of the system with N particles.

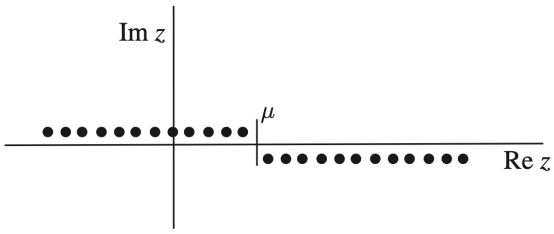

Figure 2.1: Analytic structure of the Green's function on the complex plane. Poles are located above the real axis for occupied states, below the chemical potential μ. Above μ, empty poles are located below the real axis. This can be seen from the Lehmann representation of the Green's function in Eq. (2.10). For a continuum of poles, the Green's function presents a branch cut above and below the real axis, following the poles' structure. Figure adapted from Ref. [20].

Thus, the response function χ can be calculated *only by knowing the system of N particles and its neutral excitations*. This comes from the fact that any operator ($\hat{A}$ or $\hat{B}$) depends on time via an even combination at equal time of $\hat{\psi}^\dagger(\mathbf{r}, t)\hat{\psi}(\mathbf{r}', t)$, in the position representation.

In summary, in linear response theory, the system never reaches an intermediate state with $N\pm 1$ particles but rather conserves the number of particles throughout the dynamics. Conversely, in the one-particle Green's function, excitations involve changes in the number of particles since the system transitions from N to $N \pm 1$ particles. From a free-particle perspective, negative frequencies correspond to ionizing the system from different valence levels, while positive frequencies correspond to adding an electron to the conduction band.

2.5 Time-ordering from an embedding perspective

In Green's function theories, time-ordering is a crucial property of dynamical propagators. The need for time-ordering arises from expressing the non-interacting Green's function $G_0(\mathbf{r}_1, t_1; \ldots; \mathbf{r}_{2n}, t_{2n})$ with $2n+1$ points using the one-particle non-interacting $G_0(\mathbf{r}, t; \mathbf{r}', t')$. This is accomplished by Wick's theorem, which, in the context of Fermions, proves that the (time-ordered) $2n+1$-point Green's function can be expressed as the Slater determinant of the one-particle (time-ordered) Green's function.

Although this perspective highlights the deep connection between time-ordered Green's functions and wave function theory, in this thesis, we will focus on how time-ordering is linked to embedding.

As mentioned earlier, the Dyson equation describes a system embedded in a bath, effectively replacing the Schrödinger equation as the fundamental equation of motion for the system. The nature of the embedding is irrelevant, and, as previously shown, embedding degrees of freedom to arrive at a single-particle problem from a many-body interacting Hamiltonian is allowed.

In frequency space, the Dyson equation yields a non-linear eigenvalue problem (as introduced in Ch. 4) that has solutionsat the resonant frequencies of the system, which are the poles of the Green's function. To each pole, only one state is assigned and termed the Dyson orbital for the system. The n stationary eigenstates of a non-interacting system are replaced by infinitely many Dyson orbitals, which cannot be (all) orthogonal to each other. Complex poles play the role of the eigenvalues. As in the non-interacting Schrödinger case, the Dyson orbitals can be occupied or empty. The sign of the imaginary part of the pole determines whether the orbital (or the pole) is occupied. From Eq. (2.5), one can see that (quasi)particles, i.e., occupied states, propagate forward in time, and the imaginary part of the poles is positive. For holes, the imaginary part is negative.

Over the complex plane, the *analytic* structure of the Green's function (in frequency) is shown in Fig. 2.1. Poles that describe occupied states lie in the upper part of the complex plane, whereas those describing holes lie in the lower part and occur after the chemical potential or Fermi energy.

2.6 Can the self-energy be static, real, or local?

As explained in Sec. 2.2, the Dyson equation arises from an embedding procedure that reduces the N-particle degrees of freedom to one in the context of interactions. This leads to a dynamic one-particle Dyson equation for the Green's function, with the self-energy serving as a complex-valued non-local potential. It is interesting to consider whether the self-energy can be simplified, such as by making it static, real, local, or some combination thereof.

A static one-particle self-energy would imply a Dyson equation of the form

$$G(\omega)^{-1} = \omega - h_0 - \Sigma(0), \tag{2.65}$$

i.e., a Schrödinger-like equation for the one-particle Green's function. As stated in Sec. 2.1, this equation of motion is satisfied only by non-interacting Green's functions for closed systems. Since the interaction is responsible for the self-energy, it is not possible for it to be static. Interestingly, and conversely, this thesis shows a way to write a Dyson equation with a static effective Hamiltonian that yields the exact Green's function of the system. The trick here is to introduce effective degrees of freedom. Thus, a more precise reformulation of the statement above is: *for a closed interacting system, the Dyson equation for the one-particle Green's function yields a dynamic self-energy that operates on the same degrees of freedom as* h_0.

In principle, a real self-energy would seem like a reasonable assumption. However, in non-interacting theories, complex Hamiltonians are present, e.g., to describe non time-reversal physics. In Green's function theories, a complex self-energy is needed to describe the finite lifetimes of quasi-particles (see also Sec. 2.7 for a discussion on quasi-particles). In an interacting system, since single particles do not exist, wave functions describing quasi-particles must decay in time, and a dynamic picture must be adopted. In such systems, quasi-particles

are continuously created and destroyed, and they are not stationary states of any Hamiltonian with real eigenvalues.

Before making any arguments about locality, it is best to introduce its meaning. As an example, both correlation and exchange interactions are in principle non local. Even at the Hartree-Fock level, where there is no correlation, non-locality is brought about by the exchange term. Though true, the exchange potential is not long-range when bracketed between far apart (in space) wave functions. The simplest way to see this is to represent the Hartree and exchange term in position:

$$\langle \mathbf{r} | \hat{V}_{\mathrm{H}} | \mathbf{r}' \rangle = v_{\mathrm{H}}(\mathbf{r})\delta(\mathbf{r}-\mathbf{r}'), \qquad \langle \mathbf{r} | \hat{V}_{\mathrm{ex}} | \mathbf{r}' \rangle = \frac{n(\mathbf{r},\mathbf{r}')}{|\mathbf{r}-\mathbf{r}'|}, \tag{2.66}$$

where $\hat{n}$ is the density matrix of the system. Thus, while the Hartree term is purely local, the exchange is regulated by the density matrix, which is non-local but short-range for $|\mathbf{r}-\mathbf{r}'|$. In insulators, the density matrix decays exponentially, making $\langle \mathbf{r} | \hat{V}_{\mathrm{ex}} | \mathbf{r}' \rangle$ short-range. In metals, the decay of the density matrix is polynomial, thus $\langle \mathbf{r} | \hat{V}_{\mathrm{ex}} | \mathbf{r}' \rangle$ does not strictly decay as an exponential, though faster than $\frac{1}{r}$. In realistic metals, this defiance of Hartree-Fock is cured by screening, which modifies the bare Coulomb potential into a short-range one. Early works of Thomas and Fermi suggest a Yukawa-type screened potential for metals, and from that, many works confirm that screening makes the interaction to become short-range [36].

On more general grounds, in a seminal paper, Kohn inferred that even in the quantum theory of solids, there is a principle of "near-sightedness", i.e., (effective) interactions decay fast in space [44, 45]. A very successful example of the application of these findings is the local density approximation for the exchange-correlation functional in density functional theory [9]. As mentioned in Ch. 2, the exact form for the exchange-correlation functional is unknown.[6]

The concept of near-sightedness may also apply to dynamical potentials, such as the self-energy in an interacting system. This was initially explored by Sham and Kohn in Ref. [48], but has since been revived, proven, and applied by Georges and coworkers to give rise to dynamical mean-field theory. In Ref. [49], Georges and Kotliar prove that, *in infinite dimensions*—that is, with an ever-increasing number of neighbors between the interacting particles–the self-energy is a local quantity. In materials, this *effectively decouples* a short-range "strongly correlated" region near the atom–termed impurity–from a long-range part which can be treated by a mean-field theory—called the bath. Similarly to the local density approximation of density functional theory, in dynamical mean-field theory the material is partitioned into a "sum of equivalent" impurities, that are embedded in a weakly interacting bath. Impurities and the

[6] For materials in which the density is slowly varying, the material can be partitioned into vanishing volumes, where the density is thought to be constant. If these small cubes are not interacting (near-sightedness), then the energy is the sum of the exchange and correlation energy of the electron gas at that particular density of the small volume. In a seminal article, Ceperley and Alder calculated the energy of the electron gas via a very accurate method, i.e., quantum Monte Carlo [46], and Perdew and Zunger fit it to a functional form [47]. After many years, these results are used in everyday DFT ab initio calculations, where the local density approximation is improved, e.g., by a semi-local approximation used in this thesis [10].

bath communicate via an effective dynamical potential, the *hybridization function*. Since the short-range part–describing strong correlation—of the self-energy has to be the same between the material and the impurity, a self-consistent cycle between the two is imposed and used to find the Green's function of the system. The problem of excluding interactions that are present both in the impurity and the mean-field, and that must not be counted twice, is termed the *double counting problem*, and is a matter of ongoing research [50]. Also, solving exactly the impurity embedded in the rest of the medium is still a very active branch of this theory [21]. Modern formulations of dynamical mean-field theory include DFT+DMFT or GW+DMFT, where the long-range interactions are accounted for by an approximate Kohn and Sham potential, or by a GW self-energy.

From this analysis, it is evident that to describe the *full* one-particle Green's function, a dynamical, complex, non-local self-energy is needed. A natural question arises: what if one does not want to describe the *full* one-particle Green's function but only "a part of it" exactly? In Ref. [51], Casida supposes to constrain the self-energy in the Luttinger-Ward functional to be static, real, and local. Interestingly, he finds that such a constraint leads to an approximate version of the Kohn and Sham potential, and thus is able to reproduce $G(\mathbf{r}, t; \mathbf{r}, t^+)$, i.e., the ground-state density of the system. In Ref. [52], a dynamical, real, and local self-energy has been shown to be flexible enough to describe the spectral density of the system, $|\mathrm{Im}G(\mathbf{r}, \mathbf{r}, \omega)|$.

In summary, it should be clear that to describe the full one-particle Green's function of a system, a dynamical, complex, and non-local self-energy has to be employed. One can reduce the complexity of the problem by either making approximations, e.g., DMFT, or by aiming to reproduce only a part of the full Green's function.

2.7 Linking the spectral function to angle-resolved photoemission spectroscopy

In this section, we will draw a link between spectral functions in the frequency domain and angle-resolved photoemission/absorption spectroscopy.

As can be seen from Eq. (2.13), the spectral function is peaked at the removal energies for occupied poles or additional energies for empty poles in the system. Thus, for example, in a molecule, the lowest energy to remove an electron is equal to the energy of the highest occupied pole (also called the highest occupied molecular orbital, HOMO), at which the spectral function is peaked. Furthermore, the amplitudes modulating the Dirac deltas in the diagonal part of the spectral function in Eq. (2.13) give the probability for the process to happen. For a deeper understanding of this, it is best to look at the spectral function in terms of creation-annihilation operators. By writing A as a function of G using Eq. (2.14), and using

the definition of G

$$\langle \mathbf{r} | A(\omega) | \mathbf{r}' \rangle = A(\mathbf{r}, \mathbf{r}', \omega) = \left| \mathrm{Im} G(\mathbf{r}, \mathbf{r}', \omega) \right| = \\ \mathrm{sgn}(\omega - \mu) \left[\int_0^{+\infty} \mathrm{d}\tau \, e^{i\omega\tau} \langle GS | \hat{\psi}(\mathbf{r}, \tau) \hat{\psi}^\dagger(\mathbf{r}', 0) | GS \rangle - \int_{-\infty}^0 \mathrm{d}\tau \, e^{i\omega\tau} \langle GS | \hat{\psi}^\dagger(\mathbf{r}', 0) \hat{\psi}(\mathbf{r}, \tau) | GS \rangle \right], \tag{2.67}$$

where μ is the chemical potential. The quantity

$$\mathrm{Im} \int_{-\infty}^0 \mathrm{d}\tau \, e^{i\omega\tau} \langle GS | \hat{\psi}^\dagger(\mathbf{r}', 0) \hat{\psi}(\mathbf{r}, \tau) | GS \rangle , \tag{2.68}$$

describes the process of a sample in its ground state $\langle GS|$, removing an electron at time 0 and position $\mathbf{r}'$, and returning to the equilibrium state after some time τ, having recovered an electron somewhere else. This has to be resonant at all electron removal energies and thus peaked at those, with a weight regulated by the probability of the process.

In a real angle-resolved photoemission experiment (ARPES), one does not control the position of the electron to be removed, but more realistically, the momentum (angle) of the electron that comes out. This is very convenient for crystals since momenta with values in the first Brillouin zone of added particles or holes are conserved. Indeed, the probability amplitude of momentum change in the addition or removal process is zero. This can be seen from the fact that the spectral function $A(\omega)$ is diagonal in the momentum space, i.e., $\langle \mathbf{k} | A(\omega) | \mathbf{k}' \rangle = \delta_{\mathbf{k},\mathbf{k}'} A(\mathbf{k}, \omega)$, where it is clear that the added or removed electron to the initial state has the same momentum as the one removed or added to the final state.

With non-interacting electrons, the proof of this would be the Bloch theorem [36]. In fact, the theorem states that the non-interacting Dyson orbitals in the Lehmann representation of Eq. (2.12), i.e., the eigenstates of the Hamiltonian, are also eigenstates of the translations of the material, making $\mathbf{k}$ a quantum number:

$$G(\omega) = \sum_{\mathbf{k},l} \frac{|\phi_{\mathbf{k}l}\rangle \langle \phi_{\mathbf{k}l}|}{\omega - \epsilon_{\mathbf{k}l} + i\eta \, \mathrm{sgn}(\epsilon_{\mathbf{k}l} - \mu)}, \tag{2.69}$$

where l is the band index.

For interacting electrons, the proof is more complex since, in general, the total Hamiltonian of the system $\hat{H}$ does not commute with the lattice translations of single electrons, but with all the electrons together. The problem is actually the same when analyzing the commutation between the Hamiltonian for a multi-electron atom, e.g., Helium, and the angular momentum operators for the two electrons. Indeed, due to the electron-electron interaction, the Hamiltonian commutes with the sum of the operators (total angular momentum) and not with each one singularly.

To prove the diagonality of the spectral function in momentum space, we start by writing the Green's function in the momentum basis. Taking into account Eq. (2.10) and Eq. (2.11), we

have

$$G(\mathbf{k},\mathbf{k}',\omega) = \sum_s \frac{\langle GS|\hat{c}_{\mathbf{k}}|s,N+1\rangle\,\langle s,N+1|\hat{c}^{\dagger}_{\mathbf{k}'}|GS\rangle}{\omega-\epsilon_s+i\eta} + \sum_s \frac{\langle GS|\hat{c}^{\dagger}_{\mathbf{k}'}|s,N-1\rangle\,\langle s,N-1|\hat{c}_{\mathbf{k}}|GS\rangle}{\omega-\epsilon_s-i\eta}. \tag{2.70}$$

The Bloch theorem for a many-particle system states that an eigenstate of the Hamiltonian for a fixed number of particles has to obey

$$\Phi_{\mathbf{K}}(\mathbf{r}_1+\mathbf{R},\ldots,\mathbf{r}_N+\mathbf{R}) = T_{\mathbf{R}}\Phi_{\mathbf{K}}(\mathbf{r}_1,\ldots,\mathbf{r}_N) = e^{i\mathbf{K}\cdot\mathbf{R}}\Phi_{\mathbf{K}}(\mathbf{r}_1,\ldots,\mathbf{r}_N), \tag{2.71}$$

since the Hamiltonian commutes with all the translations of the lattice,

$$T_{\mathbf{R}}H_N = H_N T_{\mathbf{R}}. \tag{2.72}$$

The total momentum $\mathbf{K}$ is then a good quantum number, and we can use it to label the $|s,N+1\rangle$ and $|s,N-1\rangle$ states, having $|\mathbf{K},i,N+1\rangle$ and $|\mathbf{K},i,N-1\rangle$, respectively. By using the anti-commutation relations, it is possible to prove that

$$T_{\mathbf{R}}\,\hat{c}_{\mathbf{k}}\,|\mathbf{K},i,N+1\rangle = e^{i(\mathbf{K}-\mathbf{k})\mathbf{R}}\,\hat{c}_{\mathbf{k}}\,|\mathbf{K},i,N+1\rangle\,, \quad\Rightarrow\quad \hat{c}_{\mathbf{k}}\,|\mathbf{K},i,N+1\rangle = |\mathbf{K}-\mathbf{k},i,N+1\rangle\,, \tag{2.73}$$

and that

$$T_{\mathbf{R}}\,\hat{c}^{\dagger}_{\mathbf{k}}\,|\mathbf{K},i,N-1\rangle = e^{i(\mathbf{K}+\mathbf{k})\mathbf{R}}\,\hat{c}^{\dagger}_{\mathbf{k}}\,|\mathbf{K},i,N-1\rangle\,, \quad\Rightarrow\quad \hat{c}^{\dagger}_{\mathbf{k}}\,|\mathbf{K},i,N-1\rangle\,|\mathbf{K}+\mathbf{k},i,N-1\rangle\,. \tag{2.74}$$

Assigning a total momentum $\mathbf{K}_0$ to the ground state $|GS\rangle$ and using the orthonormality between eigenstates of different eigenvalues (of the unitary operators $T_{\mathbf{R}}$), the Green's function is rewritten as:

$$G(\mathbf{k},\mathbf{k}',\omega) = \left(\sum_i \frac{\langle GS|\hat{c}_{\mathbf{k}}|\mathbf{K}_0+\mathbf{k},i,N+1\rangle\,\langle\mathbf{K}_0+\mathbf{k},i,N+1|\hat{c}^{\dagger}_{\mathbf{k}}|GS\rangle}{\omega-\epsilon_i+i\eta} + \sum_i \frac{\langle GS|\hat{c}^{\dagger}_{\mathbf{k}}|\mathbf{K}_0-\mathbf{k},i,N-1\rangle\,\langle\mathbf{K}_0-\mathbf{k},i,N-1|\hat{c}_{\mathbf{k}}|GS\rangle}{\omega-\epsilon_i-i\eta}\right)\delta_{\mathbf{k},\mathbf{k}'} = G(\mathbf{k},\omega)\,\delta_{\mathbf{k},\mathbf{k}'}, \tag{2.75}$$

where $\mathbf{k}$ is restricted to the first Brillouin zone due to periodic boundary conditions. As a consequence, the spectral function $A(\omega)$ is diagonal in the crystal momentum space.

Equation (2.75) is basically the Bloch theorem for many-particle systems translated into the language of Green's functions. Before delving into the ARPES experiments, there is one final remark to be made. In a later section, we will analyze in depth the solution of the Dyson equation and the fact that, in general, the number of poles of the Green's function does not need to be constrained by the dimension of the Hilbert space of the Kohn and Sham Hamiltonian. In fact, the occupied poles for a non-interacting Green's function, e.g., of Eq. (2.69), have to be equal to the number of particles. In an interacting system, it is clear that

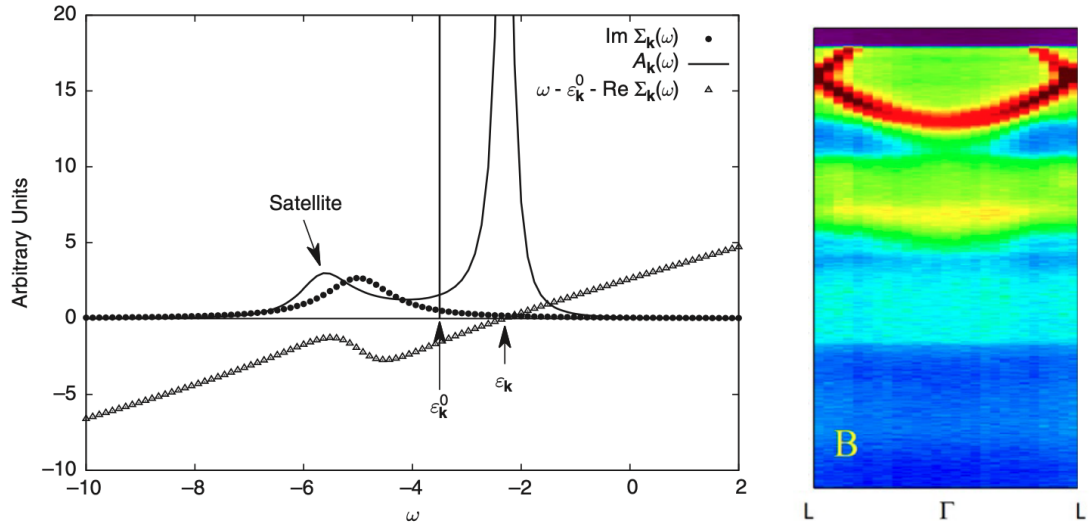

(a) Spectral function example

(b) ARPES on aluminum.

Figure 2.2: Panel (a). Example of momentum-resolved spectral function at fixed momentum. The Solid line represents the spectral function. The circles represent the self-energy, while the triangles represent the inverse of the Green's function. The main peak for the spectral function is at the quasi-particle energy $\epsilon_{\mathbf{k}}$, which is shifted by the self-energy from $\epsilon^0_{\mathbf{k}}$. The other peak is termed a satellite and has a purely dynamical origin. Figure taken from Ref. [20]. Panel (b). Angle-resolved photoemission experiment on aluminum. The color map goes from high (red) to low (green and blue). Figure taken from Ref. [3].

the number of occupied poles is equal to the number of excitations of the system with $N-1$ particles. At the thermodynamic limit, this is infinite and results in an infinite and infinitely dense set of poles in the Green's function for an interacting system. This is the heuristic reason why Green's functions develop a branch cut above the real axis for occupied states and below for unoccupied ones. For a nice and complete review of the exact mathematical details and implications, see Ref. [53]. Since there are some parts of the spectrum in which there is an accumulation of poles, the peaked structure of the spectral function from Eq. (2.13) is summed and becomes a smoother function with broad peaks.

The single element of the momentum-resolved spectral function $A_{ii}(\mathbf{k},\omega)$—with i labelling a state of the non-interacting Bloch Hamiltonian at $\mathbf{k}$, same as in Eq. (2.75)—is shown by the solid line in Fig. 2.2a. The main peak is the quasi-particle peak and is centered at $\epsilon_{\mathbf{k}}$, shifted from the non-interacting energy $\epsilon^0_{(i)\mathbf{k}}$. The lifetime of the quasi-particle is long but not infinite, expressed by the broadening of the peak which originates from the accumulation of poles of the Green's function around $\epsilon_{\mathbf{k}}$. The other, more broadened peak is termed the *satellite* and has a purely dynamical origin. In a non-interacting theory, $A_{ii}(\mathbf{k},\omega)$ can only have one delta peak, whereas in an interacting system, due to the linear dependence of the Dyson orbitals, $A_{ii}(\mathbf{k},\omega)$ can have multiple peaks.

In an ARPES experiment, the different elements of the spectral function at fixed momentum

are not resolved, and thus the function to be studied is $A(\mathbf{k},\omega) = \sum_i A_{ii}(\mathbf{k},\omega)$. Due to the sum rule $\int \mathrm{d}\omega\, A(\omega) = 1$ (see Sec. 2.1 for details), the equality $\int \mathrm{d}\omega\, A(\mathbf{k},\omega) = 1$ holds at each fixed momentum. For a particular path in the Brillouin zone, the spectral function $A(\mathbf{k},\omega)$ looks as in Fig. 2.2b. This is a real ARPES experiment on Aluminum along the $\Gamma - L$ path of the Brillouin zone. The red quasi-particle (free-like) band is evident along with the satellite with much less dispersion.

3 SOP for dynamical operators

In this Chapter we introduce the sum-over-poles representation for dynamical operators. Since frequency is crucial in this framework, finding a suitable representation of dynamical (frequency-dependent) operators is hard by construction. Taking for example the Green's function, from the Lehmann representation of Eq. (2.12), it can be deduced that it is "at best" diverging on a finite number of poles along the real axis. Thus, performing integrals on the real axis is challenging. The content of this Section is based on my article [34]. In Ref. [34]all operators are diagonal in the same basis because homogeneous systems are treated, i.e., the plane-wave basis. This said, the scope of the thesis is to address both homogeneous and non-homogeneous (crystalline) systems, thus we make the distinction from scalars to matrices only when needed

Throughout the whole Chapter we use the symbols G to indicate a generic (time-ordered) propagator and A for its spectral function.

3.1 Introducing the sum over poles representation

In this Section we introduce the sum-over-poles representation for dynamical propagators. The goal is to find a suitable representation over frequency that takes into account their pole-like analytic structure (see Sec. 2.5), respects the properties of dynamical propagators, e.g., the sum rules, and ease the computation of frequency integrated quantities.

For this purpose, we express frequency-dependent propagators and self-energies, as well as polarizabilities or screened Coulomb interactions, in a sum-over-poles (SOP) form:

$$G(\omega) = A_0 + \sum_{i=1}^{N} \frac{A_i}{\omega - z_i}, \tag{3.1}$$

where the constant term A_0 may be present for self-energies and potentials. We consider the residues A_i as operators acting on the Hilbert space of G, and the scalar poles $z_i = \epsilon_i + i\delta_i$ where $\epsilon_i, \delta_i \in \mathbb{R}$. To ensure the correct analytical structure respecting time-ordering, we take

$\delta_i \gtrless 0$ when $\epsilon_i \lessgtr \mu$, where μ is the effective chemical potential of the propagator. For a Green's function, μ is the Fermi energy of the system; for a polarizability or a screened potential, $\mu = 0$. The parameter N is the number of poles and is treated as a convergence parameter. This is well-discussed in Ref. [54], where the authors show that time-ordered propagators can always be written as a continuous fraction, for which the SOP representation with a finite N corresponds to a truncation. The procedure for choosing a representative SOP for a given propagator, i.e., the number of poles, poles, and amplitudes, is the subject of the next sections.

3.2 Spectral representations

Following Ref. [55], we consider the spectral representation of a propagator (here the Green's function for simplicity), where G is expressed in terms of its spectral function A as:

$$G(\omega) = \int_{\mathscr{C}} \frac{A(\omega')}{\omega - \omega'} d\omega'. \tag{3.2}$$

This is done by performing a time-ordered Hilbert transform (TOHT), where $\mathscr{C}$ is a time-ordered contour which is shifted above/below the real axis for $\omega' \lessgtr \mu$ (see also Sec. 2.5), and the shift is sent to zero after the integral is computed. Accordingly, the inverse relation to go from G to A is given by:

$$A(\omega) = \frac{1}{2\pi i} \left[G(\omega) - G^{\dagger}(\omega) \right] \operatorname{sgn}(\mu - \omega). \tag{3.3}$$

To represent the spectral function on a finite basis set $\{b_j(\omega)\}_{1,\dots,M}$, we have:

$$A(\omega) = \sum_{j=1}^{M} a_j b_j(\omega) \operatorname{sgn}(\mu - \epsilon_j) = \sum_{j=1}^{M} a_j \left| b_j(\omega) \right|. \tag{3.4}$$

Here, $b_j(\omega)$ is centred on ϵ_j and is positive (negative) for $\epsilon_j \lessgtr \mu$. The matrices a_j are positive definite ($a_j > 0$), acting on the Hilbert space of A.

We can induce a representation of G by introducing a discrete time-ordered Hilbert transform (D-TOHT) as:

$$G(\omega) = \sum_{j=1}^{M} a_j \int \frac{\left| b_j(\omega') \right|}{\omega - \omega' - i0^+ \operatorname{sgn}(\mu - \epsilon_j)} d\omega'. \tag{3.5}$$

The sign chosen for b_j in Eq. (3.4) gives, by construction, the time-ordered analytic structure of the Green's function.

In the case where all b_j become Dirac delta functions and M becomes infinitely large (continuum representation limit), Eq. (3.5) becomes the standard TOHT of Eq. (3.2) (with $\mathscr{C}$ shifted by $\pm i0^+$).

A natural choice is to use a basis of Lorentzian functions centered at different frequencies ϵ_j,

given by:

$$|b_j(\omega)| = \mathscr{L}_{\delta_j}(\omega - \epsilon_j) = \frac{1}{\pi}\frac{|\delta_j|}{(\omega-\epsilon_j)^2+\delta_j^2}, \tag{3.6}$$

where the D-TOHT for the single element is analytical, yielding a pole function $1/(\omega - z_j)$ with $z_j = \epsilon_j + i\delta_j$. The sign convention for δ_j is defined as discussed above according to time ordering. Thus, choosing b_j as in Eq. (3.6) induces a SOP representation for G according to Eq. (3.1), with $A_i = a_i \in \mathbb{R}$ and $N = M$. Once the SOP representation of G is known, i.e. poles and amplitudes are known, the grid evaluation (inverse of the above) is trivial and amounts to performing the finite sum in Eq. (3.1). This approach ensures a full-frequency treatment of the propagator (approaching the continuum representation limit when Lorentzians become delta functions), while preserving an explicit knowledge of the analytical structure and continuation of G.

One drawback of using Lorentzians to represent G is related to the slowly decaying tails ($1/\omega^2$ for $\omega \to \infty$) induced in the spectral function when using finite broadening values δ_j. In order to improve on this, we introduce here n-th order generalized Lorentzians to obtain fast-decay basis functions. These are defined as:

$$\left|b_j(\omega)\right| = \mathscr{L}^n_{\delta_j}(\omega - \epsilon_j) = \frac{1}{N_n\pi}\frac{|\delta_j|^{2n-1}}{(\omega-\epsilon_j)^{2n}+(\delta_j)^{2n}}, \tag{3.7}$$

where $N_n = \left[n\sin\left(\frac{\pi}{2n}\right)\right]^{-1}$ is the normalization factor (see Appendix B.1). The D-TOHT of $\mathscr{L}^n_\delta$ remains analytic and still yields a SOP representation for G (see Appendix B.1):

$$\int_{\mathscr{C}} d\omega' \frac{\mathscr{L}^n_{\delta_j}(\omega'-\epsilon_j)}{\omega-\omega'-i0^+\,\mathrm{sgn}(\mu-\epsilon_j)} = \sum_{m=0}^{n-1}\frac{\alpha_m}{\omega-\zeta_{j,m}}, \tag{3.8}$$

with residues α_m and poles $\zeta_{j,m}$ given by:

$$\alpha_m = \frac{1}{iN_n n}e^{i\frac{\pi}{2n}(1+2m)}, \tag{3.9}$$

$$\zeta_{j,m} = \epsilon_j + e^{i\frac{\pi}{2n}(1+2m)}\delta_j. \tag{3.10}$$

Importantly, α_m are complex and the residues in the SOP representation of Eq. (3.1) become $A_i = a_j\alpha_m$, i being a combined index and $N = M \times n$. Thus, the spectral function of this SOP has a contribution from both the real and imaginary parts of each Lorentzian pole $1/(\omega - \zeta_{j,m})$, resulting in an overall decay faster than each single Lorentzian. Also, it is worth noting that, as for standard Lorentzians, a normalized n-th order Lorentzian approaches a Dirac delta for $\delta_j \to 0^+$.

Owing to their fast decay and the aforementioned property, using a SOP for G_0 in terms of n-th order Lorentzians provides faster convergence for $\delta \to 0^+$ compared to a SOP representation built on ordinary Lorentzians, as will be shown later.

While using n-th order generalized Lorentzians to represent the spectral function $A(\omega)$ provides faster decay in the imaginary part of the propagator, it results in a multiplication of the number of poles in the SOP for G (by the degree of the Lorentzian). As shown in Sec. 3.4, the decay properties are useful for evaluating the moments of a SOP representation, ensuring absolute convergence up to order $2(n-1)$.

Alternatively to n-th order Lorentzians, one could consider using Gaussian functions to represent $A(\omega)$, and consequently $G(\omega)$, as done in Refs. [56, 55]. Gaussian functions also allow for an analytical expression of the D-TOHT. However, this comes at the cost of invoking the Dawson [57] or Faddeeva [58] functions to evaluate the real part of the propagator. As a result, SOP expressions are not available, and basic operations involving propagators (such as those described in Sec. 3.4) cannot be evaluated analytically and need to be worked out in other ways, such as numerically or by recasting the expressions in terms of propagator spectral functions [56]. Furthermore, the algorithmic inversion method discussed in Sec. 4.2 is not available when using Gaussian basis sets to describe $A(\omega)$.

3.3 Transforming to a sum over poles

After introducing the SOP representation, the next important step is to numerically determine the SOP coefficients A_i in Eq. (3.1), given an evaluation of the propagator on a frequency grid $G(\omega)$. Since in this thesis, we mainly perform the transformation to scalar propagators of the HEG—such as P or Σ, as detailed in Chapter 6—or $U(\omega)$—an average of the matrix elements of $W(\omega)$, as detailed in Ch. 5—we limit the treatment to scalar propagators. The extension of the algorithms to the matrix case can be easily done by applying them element-wise, while keeping the same poles for all elements to handle scalar poles only.[1]

3.3.1 SOP from the spectral function

According to the discussion in Sec. 3.2, the SOP representation can be equivalently viewed as a representation for either the propagator $G(\omega)$ or the spectral function $A(\omega)$.

As a first case, we consider representing the spectral part of the propagator $A(\omega)$ according to Eq. (3.4) and using the basis of n-th order generalized Lorentzians introduced in Eq. (3.7). To obtain the coefficients a_j of the representation, we perform a non-negative least squares (NNLS) fit [59, 58], which ensures the positivity (or positive definiteness for operators) of all a_j. We then use Eqs. (3.9) and (3.10) to obtain the SOP representation for the propagator.

Although the position and broadening (ϵ_j, δ_j) of the n-th order Lorentzians could also be optimized by means of a non-linear NNLS fit, we consider them centered at $\epsilon_j = \frac{1}{2}\left(\omega_j + \omega_{j-1}\right)$ and broadened with $\delta_j = \left|\omega_j - \omega_{j-1}\right|$, and we only linearly optimize a_j. For numerical reasons,

[1] This is not strictly necessary for the algorithmic inversion method, but considering such cases goes beyond the scope of this thesis.

we prefer to work with the bare imaginary part of G instead of the actual spectral function $A(\omega)$, without imposing the sign factor of Eq. (3.3), as this function is smoother near the Fermi level. We illustrate this approach in Sec. 3.5.1 and use it for the calculations on the HEG.

3.3.2 SOP from the propagator

Alternatively, one could consider the basis representation induced on the propagator directly, via Eq. (3.1), in order to obtain the A_i and z_i coefficients (residues and poles). Here, we obtain the coefficients using a mixed linear and non-linear least square minimization of the cost function given by:

$$C = \sum_j \left| U(\omega_j) - \sum_l \frac{A_l}{\omega_j - g_l} \right|^2 . \tag{3.11}$$

At each step of the minimization, we find the real coefficients A_l using a generalized linear least square approach [60], and the complex (time-ordered) poles g_l using simulated annealing on C with the newly found amplitudes. Due to its non linearity, this algorithm requires an initial guess of the real (position) and imaginary (broadening) parts of the poles, and, at each step, moves them at most by 10% of their value. This algorithm is demonstrated in Sec. 3.5.2 and used in the calculations on $SrVO_3$.

Interestingly, the SOP representation in Eq. (3.1) is a special case of a Padè approximant, written as the ratio of polynomials of order $N-1$ and N, respectively. Because of this, one can exploit Padè-specific approaches to determine (A_i, z_i), such as, for instance, Thiele's recursive scheme [61]. We found that this leads to a very efficient method when few tens of poles are considered, becoming numerically unstable beyond. For a recent exploitation of Padè and related techniques in the context of GW using a multi-pole approximation, see also our work on Ref. [62]. Moreover, since the residues are not constrained to be real and positive (in fact, A_i are complex), there is no control over the time-ordered position of the poles, and the procedure is non-trivial to extend to the case of n-th order Lorentzians.

3.4 Analytical expressions

Once the SOP representation of a dynamical propagator is available, several analytical expressions hold. For instance, the convolution of propagators, such as those involved in the evaluation of the independent-particle polarizabilities in terms of the Green's functions, can be directly evaluated using Cauchy's residue theorem:

$$\begin{aligned}\int_{-\infty}^{+\infty} \frac{d\omega'}{2\pi i} G(\omega+\omega')\tilde{G}(\omega')d\omega' &= \sum_{i,j} \int_{-\infty}^{+\infty} \frac{d\omega'}{2\pi i} \frac{A_i}{\omega+\omega'-z_i} \frac{\tilde{A}_j}{\omega'-\tilde{z}_j} \\ &= \sum_{\substack{i,j \\ \mathrm{Im}\{z_i\}<0 \\ \mathrm{Im}\{\tilde{z}_j\}>0}} \frac{A_i\tilde{A}_j}{\omega+\tilde{z}_j-z_i} - \sum_{\substack{i,j \\ \mathrm{Im}\{z_i\}>0 \\ \mathrm{Im}\{\tilde{z}_j\}<0}} \frac{A_i\tilde{A}_j}{\omega+\tilde{z}_j-z_i},\end{aligned} \tag{3.12}$$

where A_i and $\tilde{A}_j$ are matrices.

Using the SOP for G, the following integrals can also be computed explicitly:

$$E_m[G] = \oint_\Gamma \frac{dz}{2\pi i} e^{iz0^+} z^m G(z) = \sum_{\substack{i \\ \mathrm{Im}\{z_i\}>0}} A_i z_i^m, \tag{3.13}$$

where we refer to the term $E_m[G]$ as the m-th (regularized) moment of G. Here, Γ is a closed contour in the upper-half complex plane that includes the real axis plus the enclosing arc. We note that for the $m = 0$ and $m = 1$ moments, Γ can be reduced to the real axis by using propagators G that decay as $O(1/\omega)$. We underline that if one uses an n-th order Lorentzian basis to represent $G(\omega)$ on SOP, the first $2(n-1)$ regularized moments coincide with the moments of its occupied spectral function $\int_{-\infty}^{\mu} d\omega\, \omega^{2(n-1)} A(\omega)$. For higher moments the the integral $\int_{-\infty}^{\mu} d\omega\, \omega^l A(\omega)$, with $l > 2(n-1)$, diverges, while the corresponding regularized m-th moment in Eq. (3.13) converges. This analysis is deepened in Appendix B.2.

3.5 Examples of representation on SOP

In this section, we present example cases in which we use either the algorithm in Sec. 3.3.1, which exploits the spectral part to obtain a SOP for the propagator, or the algorithm in Sec. 3.3.2, which finds a SOP for a propagator on a grid directly.

3.5.1 Algorithm using the spectral function

We consider a target propagator G with a spectral function $A(\omega) = g_1(\omega) + \frac{1}{5} g_1(\omega+4) + \frac{1}{3} g_1(\omega-5)$, where $g_\sigma(\omega)$ is a normalized Gaussian centered at zero with variance σ^2. The propagator G can be obtained using the expression for the Faddeeva function [58], assuming the Fermi level to be far enough that the retarded HT be used.

The goal of this validation is to represent the target G as a sum-over-poles and compare the results obtained using 1st and 2nd order Lorentzian basis elements. Additionally, we will study the mean-square error of the SOP-represented G as compared to the exact G, as a function of the number of poles used for the SOP. We will also examine the absolute error of the mean and variance.

Following Sec. 3.3, we represent the spectral function A via a non-negative least squares (NNLS) fit on 1st (ordinary) and 2nd order Lorentzian basis and use Eqs. (3.9) and (3.10) to obtain the sum-over-poles representation of G. Here, we use the n-th Lorentzian centered on an equally spaced grid with a broadening equal to the distance between two subsequent centers. In Figs. 3.1 (a) and (b), we use 50 basis elements to represent the target G sampled on 50 points. The real (panel (a)) and imaginary (panel (b)) parts of the target propagator are represented as black dots. The continuous lines represent the SOP obtained for G using 1st order (orange) and 2nd order (green) Lorentzian basis elements. Qualitatively, it is possible

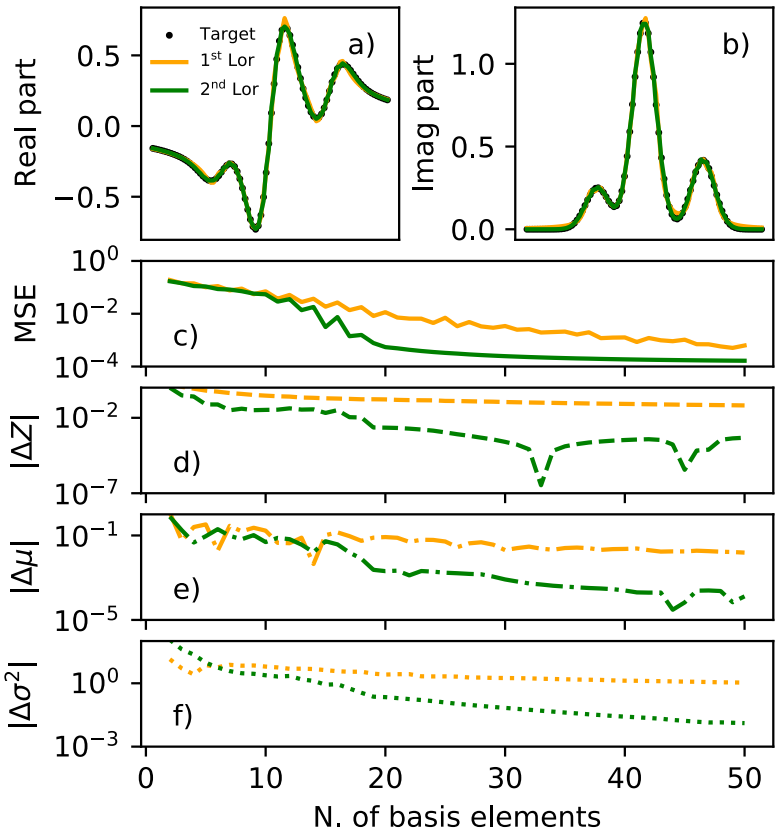

Figure 3.1: Numerical example of a transformation to a SOP form. The target propagator is chosen to have a spectral function as a linear combination of three Gaussians, sampled using 50 points (black dots). We represent the trial spectral function on 1st (orange) and 2nd (green) order Lorentzian basis elements —each centred on the midpoint between adjacent grid points and broadened with the size of the interval—, and get real and imaginary parts of the propagator analytically afterward (see Sec. 3.3 for details). We plot the result in the panels (a) and (b). In panel (c) we study the mean-square error (MSE) of the fitted propagator against the target as a function of the number of basis elements used for the representation. The last value on this graph represents the MSE of the (sum of the) panels (a) and (b) between the fitted and the target values. All the other points in panel (c) are obtained placing the Lorentzians uniformly in the given interval with a broadening equal to the distance between two consecutive functions. In the panels (d), (e), and (f) the same study is repeated for the absolute difference between the normalization of the target function and the one of the fitted propagator, its mean, and its variance. The y-scales of the graphs (c), (d), (e), and (f) are logarithmic.

to see that 2nd order Lorentzians perform better. To obtain a more quantitative comparison, Fig. 3.1 (c) shows the mean square error as a function of the number of basis elements used in the representation (and consequently in the SOP). In Figs. 3.1 (d), (e), and (f), we consider the absolute difference between the exact moment, mean, and variance of A and those obtained from the SOP. In all the graphs, a basis made of second order Lorentzians is found to perform

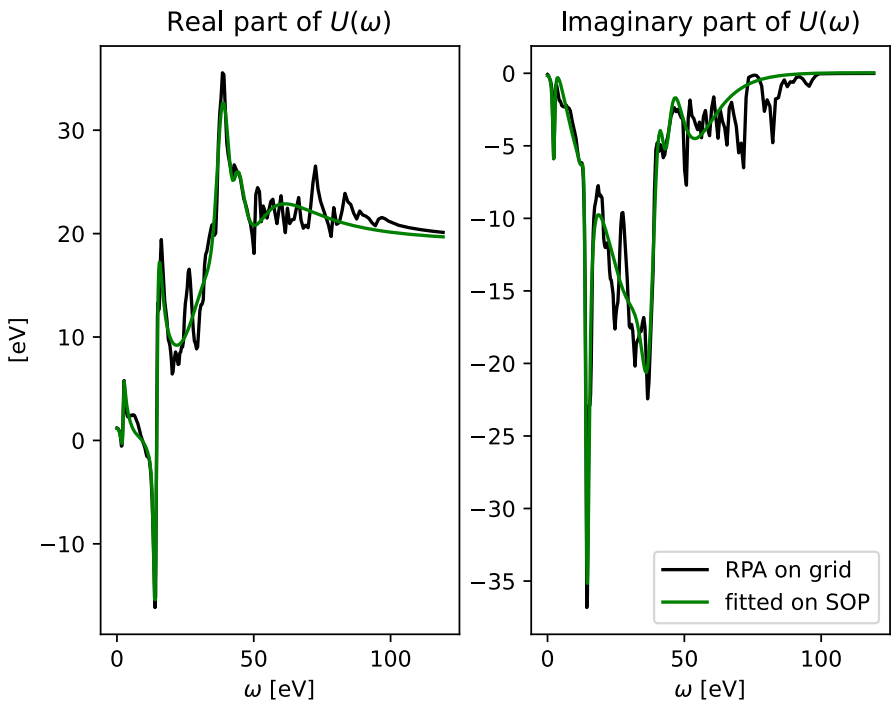

Figure 3.2: Real and imaginary part of the localized screened interaction $U(\omega)$ (for details see Ch. 5) calculated on a frequency grid using the random-phase approximation (black line) compared to its representation in a sum-over-poles form (green line) obtained the algorithm describe in the Section.

better.

It is worth noting that in order to represent the spectral function, we use a NNLS minimization to obtain the coefficients (amplitudes) of the n-th Lorentzian basis set. This results in the need to solve a linear system of equations with a positive constraint on the solution. It is possible to improve this approach by using a non-linear least squares minimization of the center and broadening of the n-th Lorentzians, optimizing not only the coefficients but also the basis (similarly to what we do in Sec. 3.3.2 and 3.5.2).

3.5.2 Algorithm using the propagator

We consider a target propagator $U(\omega)$ in the frequency domain. The details on how to obtain such a screened interaction and how to exploit it in the big scheme of the algorithmic-inversion method on sum over poles, combined with the novel dynamical Hubbard functional, are discussed in Ch. 7. In contrast to Sec. 3.5.1, here we find the SOP directly by minimizing the cost function in Eq. (3.11).

In Fig. 3.2, we show the real (left) and imaginary (right) parts of the calculated RPA screened interaction (black lines) compared to the result of the fitting procedure (green lines) with 10

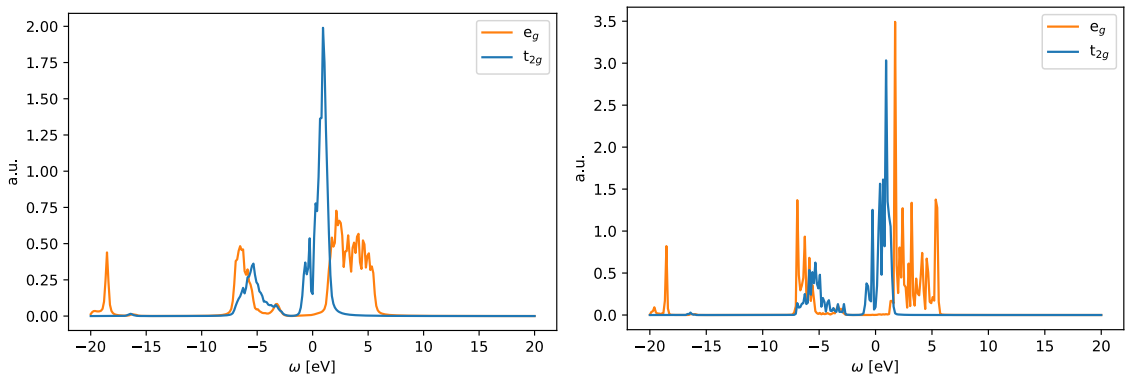

(a) Not condensed (b) Condensed

Figure 3.3: Comparison between not condensed 3.3a and condensed 3.3b spectral functions projected on the t_{2g} (blue) and e_g (orange) orbitals for $SrVO_3$. The threshold for the condensation is fixed at the value of the broadening of the merged pole. The number of poles is reduced to 1/6 of the initial number.

poles for the fit. The agreement is excellent at lower energies ($\omega < 25$ eV) and slightly worsens afterwards. Still, the error in the two limits $\omega \to 0$ and $\omega \to \infty$ (300 eV) is of the order of 10 meV, and thus quite low with respect to the energy scales of the plots in the figure. The algorithm takes minutes to run using a Python implementation.

3.6 Pole condensation

In this section, we describe an algorithm for reducing the number of poles in a SOP. Suppose we have obtained the SOP representation of a generic dynamical (time-ordered) propagator, i.e., we know the matrix residues A_i and the scalar poles z_i, but we want to reduce them to ease computational cost, as the cost of the operations scales with the number of poles in the SOP. The algorithm we design is essentially a pole condensation, as it merges poles based on certain criteria and provides a new residue from the merging.

Inevitably, when condensing the poles, some information is lost. This loss can be directly evaluated by representing both the original propagator and the condensed propagator on a frequency grid and evaluating the difference in errors, as we did in Sec. 3.5.1. Additionally, we can perform this error analysis directly on the momenta of the propagator, as we did in Sec. 3.5.1. In Ch. 7, we assess the loss in precision by examining the error in the total energy of the calculation.

Importantly, the pole condensation algorithm preserves the first moment and occupied momenta (see Sec. 6.3) of the propagator. This is very desirable since, in Ch. 7, we condense the Kohn and Sham Green's function of $SrVO_3$ — projected onto the Hubbard manifold (see the related Chapter for details) — without altering either the normalization of the spectral function or the number of particles in the system (see Sec. 2.1). Here, we limit the treatment of SOPs to

standard Lorentzians, although the generalization for n-th order generalized Lorentzians (see Sec. 3.3 for their definition) can be readily done since we consider only the spectral function and we use its center and broadening in the algorithm, weather coming from a simple or an n-th order Lorentzian makes no conceptual difference.

In order to condense the poles, we adopt a strategy inspired by the weighted mean of N random variables. Each j-th Lorentzian in the representation of the spectral function (which yields the SOP for the propagator after the D-TOHT) of Eq. (3.4) can be considered a distribution function for a random variable. This is centered around ϵ_j and has a variance of δ_j.[2] If the overlap of two Lorentzians is greater than a threshold, the two poles can be regarded effectively as one.

In particular:

- We sequentially browse the (ordered) pole array.
- We compare the weighted-mean of the first two (real part of the) poles — having a weight equal to each broadening — with the first.
- If the separation between the position (real part) of the two poles is less than a threshold, we replace them with a newly defined pole, with a position equal to the weighted mean, broadening as the weighted mean variance, and residue (or amplitude [34]) as the sum of the two.
- We continue with the rest of the poles.

We perform this procedure separately for the four quarters of the complex plane, defined by the real axis and the position of the chemical potential. [3] Please note that this procedure preserves the normalization of the Green's function — since we are summing the amplitudes —, and preserves the total number of particles since we are doing it for occupied and empty poles separately.

In Fig. 3.3, we compare the spectral functions projected onto the t_{2g} orbitals ($3d_{xy}, 3d_{yz}, 3d_{zx}$ of Vanadium) and e_g orbitals ($3d_{z^2}, 3d_{x^2-y^2}$ of Vanadium). The condensation reduces the number of poles from 3286 to 512, i.e., 1/6 of the initial number. The value of the threshold corresponds to the broadening of the merged pole. As detailed in Sec. 7, this threshold already guarantees an accuracy of the order of 10 meV per atom on the total energy calculated with the dynamical Hubbard functional introduced in Ch. 5.

[2] It should be noted that a Lorentzian is not a distribution function due to its diverging variance. To perform the weighted mean we use the variance of the distribution, in the method we use the broadening of the Lorentian.

[3] Taking into account the analytic form of the propagator (Sec. 2.5) would be sufficient to perform the algorithm separately, before and after the Fermi level, since there are no poles in the bottom/above parts of the complex plane below/after the chemical potential. Here, we consider having poles also on the "forbidden" parts of the spectrum because we apply a smearing to the Green's function (see Sec. D.2 for details).

4 Algorithmic inversion of dynamical potentials

As seen multiple times in this thesis, dynamical potentials are needed to predict accurate spectral, transport, and embedding properties of materials. The frequency fundamentally changes the problem to be solved, transitioning from the diagonalization of an operator, such as the Kohn and Sham Hamiltonian in density-functional theory, to a Dyson inversion of a self-energy. In this chapter, we develop a novel treatment of frequency-dependent potentials capable of solving Dyson-like equations.

First, we discuss Dyson-like equations involving dynamical potentials as a nonlinear generalization of the Schröedinger equation for open embedded systems, drawing a link with the mathematical formulation of nonlinear eigenvalue problems.

On this basis, we introduce the algorithmic-inversion method to solve the Dyson equation by mapping the interacting system into a non-interacting "fictitious" system, with augmented degrees of freedom. The sum-over-poles representation of the self-energy, together with the static contribution to the Hamiltonian, is used to build a (larger) effective Hamiltonian. This effective Hamiltonian has the excitation energies of the system as eigenvalues and the Dyson orbitals as a projection of the eigenvectors. Furthermore, the fictitious and real systems share the same Green's function once the spurious degrees of freedom are traced away. Thus, the sum over poles for the Green's function of the system is obtained, allowing for the computation of the spectral and thermodynamic properties.

We treat the homogeneous (scalar) case first in Sec. 4.2, and then we extend the method to a general operatorial case to be applied to crystals in Sec. 4.3.

The content of Section 4.2 is based on my article in Ref. [34], while Sections 4.1 and 4.3 are mainly based on my article in Ref. [35].

4.1 The Dyson equation as a nonlinear eigenvalue problem

In this section, we introduce a general framework to solve the Dyson equation $G(\omega) = [\omega I - h_0 - \Sigma(\omega)]^{-1}$. This task can be seen as the generalization to embedded (open) systems of the diagonalization of a Hamiltonian for closed systems. Assuming Σ to be analytical in a connected subset of the complex plane, one can exactly map [63] the solution to the Dyson equation into the nonlinear eigenvalue problem (usually shortened as NLEP):

$$\left[h_0 + \Sigma(\omega)\right] \left|\psi^R\right\rangle = \omega \left|\psi^R\right\rangle, \tag{4.1}$$

where (z_s, ψ_s^R) are the corresponding (discrete) eigenvalues and right eigenvectors. In particular, it is possible to show that the eigenvalues z_s are the poles of the resolvent $G(\omega)$, and, when poles are first-order (not granted in general), the right/left eigenvectors $\left|\psi_s^R\right\rangle\left\langle\psi_s^L\right|$ provide their residues.

Under the above hypotheses, which are fully treated in Ref. [63] and its references, we prove the above statement by showing that:

$$[\omega - h_0 - \Sigma(\omega)]^{-1} = \sum_s \frac{\left|\psi_s^R\right\rangle\left\langle\psi_s^L\right|}{\omega - z_s} + R(\omega), \tag{4.2}$$

where $R(z)$ is a smooth function without poles, and

$$[z_s - h_0 - \Sigma(z_s)] \left|\psi_s^R\right\rangle = 0, \tag{4.3}$$

with the corresponding left equation for $\left\langle\psi_s^L\right|$.

We start by expanding the operator $[\omega - h_0 - \Sigma(\omega)]$ around z_s:

$$\omega - h_0 - \Sigma(\omega) = z_s - h_0 - \Sigma(z_s) + \left[1 - \Sigma'(z_s)\right](\omega - z_s) + o(\omega - z_s), \tag{4.4}$$

where it is understood that the coefficient of each order of $o(\omega - z_s)$ is a linear operator (or matrix in a basis).

Using the definition of the inverse

$$\left\langle\bar{\psi}_i^L\right|[\omega - h_0 - \Sigma(\omega)]^{-1}[\omega - h_0 - \Sigma(\omega)]\left|\bar{\psi}_s^R\right\rangle = \left\langle\bar{\psi}_i^L\middle|\bar{\psi}_s^R\right\rangle, \tag{4.5}$$

where we denote $\bar{\psi}_s^R$ the nonlinear eigenvectors normalized to the unity, i.e., $\left\langle\bar{\psi}_s^L\middle|\bar{\psi}_s^R\right\rangle = 1$. Note that the vectors $\left|\bar{\psi}_s^R\right\rangle$, together with $\left\langle\bar{\psi}_s^L\right|$, form a complete non-orthogonal set since they solve a different eigenvalue problem at each z_s. By inserting the completeness of the

(nonlinear) eigenvectors into the above equation

$$\begin{aligned}\langle\bar{\psi}_i^L|\bar{\psi}_s^R\rangle &= \sum_j [\omega - h_0 - \Sigma(\omega)]^{-1}{}_{ij}\ [\omega - h_0 - \Sigma(\omega)]_{js} \\ &= \sum_j [\omega - h_0 - \Sigma(\omega)]^{-1}{}_{ij}\ \left[z_s - h_0 - \Sigma(z_s) + \left[1 - \Sigma'(z_s)\right](\omega - z_s) + o(\omega - z_s)\right]_{js} \\ &= \sum_j [\omega - h_0 - \Sigma(\omega)]^{-1}{}_{ij}\ \left[1 - \Sigma'(z_s)\right]_{js}(\omega - z_s)\left[1 + O_{js}(\omega - z_s)\right],\end{aligned} \tag{4.6}$$

where we used Eq. (4.3) to arrive to the last line. Multiplying by $\left[1 - \Sigma'(z_s)\right]^{-1}{}_{sl}$ and summing over s we get

$$\langle\bar{\psi}_i^L|[\omega - h_0 - \Sigma(\omega)]^{-1}|\bar{\psi}_l^R\rangle = \langle\bar{\psi}_i^L|\sum_s \frac{|\bar{\psi}_s^R\rangle\langle\bar{\psi}_s^L|\left[1 - \Sigma'(z_s)\right]^{-1}}{\omega - z_s} + O(\omega - z_s)|\bar{\psi}_l^R\rangle, \tag{4.7}$$

and consequently

$$[\omega - h_0 - \Sigma(\omega)]^{-1} = \sum_s \frac{|\bar{\psi}_s^R\rangle\langle\bar{\psi}_s^L|\left[1 - \Sigma'(z_s)\right]^{-1}}{\omega - z_s} + \sum_s O(\omega - z_s). \tag{4.8}$$

Finally, by defining

$$|\psi_s^R\rangle\langle\psi_s^L|\left[1 - \Sigma'(z_s)\right] = |\bar{\psi}_s^R\rangle\langle\bar{\psi}_s^L| \tag{4.9}$$

we have proven Eq. (4.2).

Also, in agreement with Ref. [63], by performing the trace over Eq. (4.9), the definition for $|\psi_s^R\rangle$ (and $\langle\psi_s^L|$) implies the (generalized) normalization

$$\langle\psi_s^L|1 - \Sigma'(z_s)|\psi_s^R\rangle = 1 \tag{4.10}$$

4.2 Scalar case for homogeneous systems

In this Section we introduce the algorithmic-inversion method for homogeneous systems. Here, we suppose all propagators are diagonal on the same basis, thus the framework is limited to scalars. As an example, all one-particle propagators—like the polarizability P, the screened potential W, the self-energy Σ, and the Green's function G— are diagonal in the plane wave basis for the homogeneous electron gas. The extension to the general (non-homogeneous) operatorial case is presented in Sec. 4.3.

Though the operatorial case is general, as it includes scalars, it is useful to treat the simpler homogeneous case as an introduction to the framework and formalism. As it is more natural, we draw the link to nonlinear eigenvalue problems (see Sec. 4.1) only in the general case of Sec. 4.3, although a similar analysis can be done here.

Let us suppose to have the SOP representation of the self-energy $\Sigma(\omega)$ and the non-interacting

Green's function $G_0(\omega)$ given by

$$\Sigma(\omega) = \sum_{i=1}^{N} \frac{\Gamma_i}{\omega - \sigma_i}, \qquad G_0 = \frac{1}{\omega - \epsilon_0}, \tag{4.11}$$

where any static part of the self-energy has been adsorbed in ϵ_0 for simplicity. Taking advantage of these expressions, the Dyson equation can be rewritten as

$$G(\omega) = \left[G_0^{-1}(\omega) - \Sigma(\omega)\right]^{-1} = \frac{1}{\omega - \epsilon_0 - \Sigma(\omega)} = \frac{(\omega - \sigma_1)\cdots(\omega - \sigma_N)}{T_N(\omega)}, \tag{4.12}$$

in which the $N+1$ roots of the polynomial

$$T_N(\omega) = (\omega - \epsilon_0) \prod_{i=1,N} (\omega - \sigma_i) - \sum_{j=1,N} \Gamma_j \prod_{\substack{i=1,N \\ i\neq j}} (\omega - \sigma_i) \tag{4.13}$$

are the $N+1$ poles of the Green's function (as expected when the self-energy has N poles).

The key statement of this Section is that the roots of T_N can be obtained as the eigenvalues of the $(N+1)\times(N+1)$ matrix

$$H_{\text{AIM}} = \begin{pmatrix} \epsilon_0 & \sqrt{\Gamma_1} & \dots & \sqrt{\Gamma_N} \\ \sqrt{\Gamma_1} & \sigma_1 & 0 & 0 \\ \vdots & 0 & \ddots & 0 \\ \sqrt{\Gamma_N} & 0 & \dots & \sigma_N \end{pmatrix}. \tag{4.14}$$

We prove this statement by observing that the characteristic polynomial of H_{AIM} is $T_N(\omega)$, and we proceed by induction. Since the $N=1$ case is trivial we move to the N-th case: using the Laplace expansion on the last line, the characteristic polynomial of the N-th case can be written as

$$\begin{aligned} p_{H_{\text{AIM}}}(\omega) &= \begin{vmatrix} \omega - \epsilon_0 & -\sqrt{\Gamma_1} & \dots & -\sqrt{\Gamma_N} \\ -\sqrt{\Gamma_1} & \omega - \sigma_1 & 0 & 0 \\ \vdots & 0 & \ddots & 0 \\ -\sqrt{\Gamma_N} & 0 & \dots & \omega - \sigma_N \end{vmatrix} = \\ &= (\omega - \sigma_N) T_{N-1}(\omega) + (-1)^N \sqrt{\Gamma_N} \times \begin{vmatrix} -\sqrt{\Gamma_1} & \dots & -\sqrt{\Gamma_{N-1}} & -\sqrt{\Gamma_N} \\ \omega - \sigma_1 & 0 & 0 & 0 \\ 0 & \ddots & 0 & 0 \\ 0 & \dots & \omega - \sigma_{N-1} & 0 \end{vmatrix} \end{aligned} \tag{4.15}$$

where we have used the induction hypotheses in the first term of the rhs. Applying the same procedure to the last column of the second term, and making use of the definition in Eq. (4.13),

we obtain

$$p_{H_{\mathrm{AIM}}}(\omega) = (\omega - \sigma_N) T_{N-1}(\omega) - \Gamma_N \prod_{i=1,N-1} (\omega - \sigma_i) = T_N(\omega),$$

which completes the proof.

Labelling z_i the poles of G, we calculate the residues by equating

$$G(\omega) = \sum_{i=1}^{N+1} \frac{A_i}{\omega - z_i} = \frac{(\omega - \sigma_1)\cdots(\omega - \sigma_N)}{(\omega - z_1)\cdots(\omega - z_{N+1})}, \tag{4.16}$$

and performing the limit $\lim_{\omega \to z_i} (\omega - z_i)$ on both sides (Heaviside cover-up method [64]), we obtain:

$$A_i = \frac{\prod_{k=1}^{N} (z_i - \sigma_k)}{\prod_{j=1,\, j\neq i}^{N+1} (z_i - z_j)}. \tag{4.17}$$

We have thus proven that by knowing $\Sigma(\omega)$ represented in SOP, we can find the SOP expression of G by diagonalizing the AIM-SOP matrix H_{AIM} and then evaluating the residues using Eq. (4.17).

It is worth noting that the H_{AIM} matrix can be made Hermitian under special conditions. This happens, for example, when we solve the Dyson equation for the retarded/advanced case in which the self-energy has poles with the same imaginary part $\mp\delta$, real and positive residues, and an equal broadening $\mp\delta$ for G_0 is assumed. Then, it is possible to include the imaginary part of the poles in the frequency variable ω, and solve the Dyson equation on the resulting complex path γ' (shifted by $\mp\delta$), yielding a symmetric H_{AIM}. After having found the SOP for G on γ', to obtain $G(\omega \in \mathscr{R})$ we analytically continue the solution to the real axis, obtaining $\mathrm{Im}(z_i) = \mp\delta$ for the retarded $(-)$ or advanced $(+)$ case.

We also stress that, given a self-energy represented on SOP, the solution provided by the algorithmic-inversion procedure is exact at all frequencies. This ensures that the Green's function fulfills all the sum-rules implied by the Dyson equation, including e.g. the normalization of the spectral weight, and the first and second moment sum rules of the spectral function derived in Ref. [56]. This result is crucial when evaluating frequency-integrated quantities of a Green's function, such as the number of particles or the total energy (see Sec. 6.3).

Besides the solution of the Dyson equation for G, the AIM-SOP can also be used to solve the Dyson equation for the screened Coulomb interaction $W(\omega)$,

$$W(\omega) = v_c + v_c P(\omega) W(\omega) = \frac{1}{1 - v_c P(\omega)} v_c = \epsilon^{-1}(\omega) v_c,$$

i.e., to compute the SOP representation of $W(\omega)$ once a SOP for the irreducible polarizability $P(\omega)$ is provided. Here v_c is the Coulomb potential (recalling that we are suppressing the

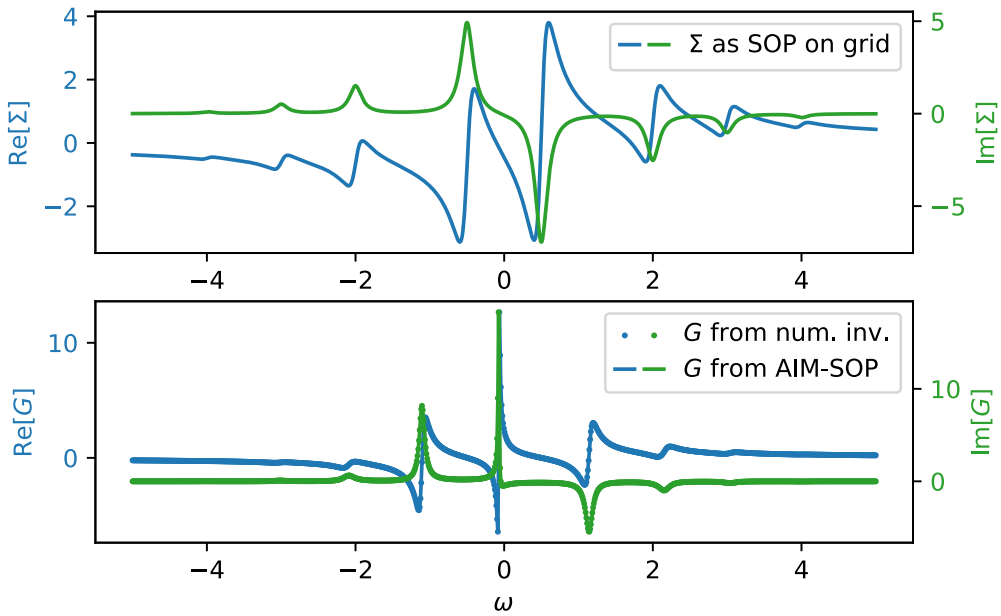

Figure 4.1: Numerical example for the algorithmic inversion method on sum over poles. Upper panel: Real (blue) and imaginary (green) part of a time-ordered self-energy, including 8 poles (the occupied pole of G_0 is not shown). Lower panel: Dyson-inverted propagator G obtained with a numerical inversion on a grid (dotted) compared with the SOP representation obtained using AIM-SOP and evaluated on the same grid (solid line). Same color code for real and imaginary parts as in the upper panel.

momentum dependence for simplicity). By letting $P(\omega) = \sum_i \frac{S_i}{\omega - g_i}$, we can write:

$$\omega v_c P(\omega) = \sum_i \omega \frac{v_c S_i}{\omega - g_i} = v_c \sum_i S_i + \sum_i \frac{v_c g_i S_i}{\omega - g_i} := c_0 - C(\omega), \tag{4.18}$$

and following Eq. (4.18) (multiplied by $\frac{\omega}{\omega}$) we have

$$\epsilon^{-1}(\omega) = \frac{1}{1 - v_c P(\omega)} = \frac{\omega}{\omega - c_0 - C(\omega)}, \tag{4.19}$$

for which the AIM-SOP matrix can be used to find the poles of $\epsilon^{-1}(\omega)$ and $W(\omega)$. The amplitudes of W are easily found using Eq. (4.17), where we note that Eq. (4.16) has to be modified taking into account frequency-constant shift of W by v_c, i.e., substituting $W(\omega) - v_c$ for G. Note that by multiplying ϵ^{-1} by $\frac{\omega}{\omega}$ in Eq. (4.19), we have inserted an extra zero in the denominator (at $\omega = 0$) which we need to discard from the eigenvalues of the AIM matrix (before applying the residue formula of Eq. (4.17)) since it simplifies with the ω factor at the numerator of Eq. (4.19). Consequently, P, ϵ^{-1}, and W all have the same number of poles, in contrast to the solution of the Dyson equation for G, where the number of poles of G is increased by one with respect to Σ.

As a numerical test for AIM-SOP, we consider the Dyson equation for G within an example of a

time-ordered self-energy built with 8 poles, as shown in the upper panel of Fig. 4.1 (the single pole of G_0 is not shown). In the lower panel, we compare the Green's function G obtained from the numerical Dyson inversion on the grid (which involves evaluating Σ on the grid and then inverting) against the Green's function obtained with the algorithmic inversion and evaluated on the frequency grid. The results are identical to the precision of the calculated eigenvalues of the AIM-SOP matrix, since the amplitude calculation of Eq. (4.17) is typically very well-conditioned. Notably, this procedure has been tested in cases where hundreds of poles are used for the self-energy without any numerical instabilities.

4.3 General operatorial case for crystals

In this section, we generalize the algorithmic-inversion method to the non-homogeneous operatorial case. In contrast to Section 4.2, where we dealt with scalars, i.e., commutative objects, here we handle non-commutative operators. These operators include the Hamiltonian h_0, the self-energy $\Sigma(\omega)$, and the Green's function $G(\omega)$.

Mathematically, the algorithmic-inversion method can be viewed as a special case of the linearization treatment of NLEP using rational functions [63]. Note that, in this context, linearization is not used in a perturbative sense. This term is borrowed from the NLEP literature and means building a linear problem that yields the exact solution of the nonlinear one. Although general algorithms to solve the NLEP problem exist, we consider here the self-energy to be meromorphic (with isolated poles) over the entire complex plane and to have only first-order poles.

This amounts to writing the dynamical part of the self-energy (the static contribution being included in h_0) as a sum over poles (SOP):

$$\Sigma(\omega) = \sum_{m=1}^{N} \frac{\Gamma_m}{\omega - \Omega_m}, \tag{4.20}$$

as done in Sec. 4.2.

In Eq. (4.20), the amplitudes Γ_m are operators that act on the one-particle Hilbert space defined by h_0, and $\Omega_m = \omega_m + i\delta_m$ are scalars that satisfy the time-ordering condition $\delta_m \gtrless 0$ when $\Omega_m \gtrless \mu$. Here, μ denotes the chemical potential of the system. Under these assumptions, $G(\omega)$ can also be expressed exactly as a SOP, and the algorithmic inversion method (AIM) will enable us to compute the coefficients of this representation.

Introducing a factorization of the self-energy residues $\Gamma_m = \bar{V}_m^\dagger V_m$, the Dyson equation for the Green's function reads:

$$G(\omega) = \left[\omega I - h_0 - \sum_m \bar{V}_m^\dagger (\omega - \Omega_m)^{-1} V_m\right]^{-1}. \tag{4.21}$$

This equation corresponds to embedding a non-interacting system h_0 and N non-interacting fictitious degrees of freedom (baths), each having a Hamiltonian $\Omega_i I_i$—with I_i being the identity on the i-th bath—and coupled to h_0 by$\bar{V}_i^\dagger$ and V_i.

In order to see this, we introduce the vectorial representation

$$\mathcal{V} = (V_1, \dots, V_N), \qquad \bar{\mathcal{V}}^\dagger = \begin{pmatrix} \bar{V}_1^\dagger \\ \vdots \\ \bar{V}_N^\dagger \end{pmatrix}, \qquad H_B = \begin{pmatrix} \Omega_1 I_1 & \dots & 0 \\ \vdots & \ddots & \vdots \\ 0 & \dots & \Omega_N I_N \end{pmatrix}, \tag{4.22}$$

and Eq. (4.21) is rewritten as

$$G(\omega) = \left[\omega I - h_0 - \bar{\mathcal{V}}^\dagger (\omega I_B - H_B)^{-1} \mathcal{V}\right]^{-1}, \tag{4.23}$$

with I_B defined as the identity matrix for H_B. The above equation is formally identical to Eq. (2.22). In fact, the first element of the Green's function matrix in Eq. (2.19), there noted as G_s, is the one-particle Green's function for the system G.

Consequently, the total Hamiltonian for the "fictitious" non-interacting system

$$H_{\text{AIM}} = \begin{pmatrix} h_0 & V_1 & \dots & V_N \\ \bar{V}_1^\dagger & \Omega_1 I_1 & 0 & 0 \\ \vdots & 0 & \ddots & 0 \\ \bar{V}_N^\dagger & 0 & \dots & \Omega_N I_N \end{pmatrix}, \tag{4.24}$$

yields the Green's function of the interacting system by $G(\omega) = P_0(\omega I_{\text{tot}} - H_{\text{AIM}})^{-1} P_0$, with P_0 projecting onto the h_0 Hilbert space.

Notably, the factorization of Γ_m is not unique. A natural choice for this is $V_m = \bar{V}_m^\dagger = \Gamma_m^{1/2}$, and in this case $I_i = I$ for all the baths. Alternatively, the factorization can be provided by the singular value decomposition (SVD) of Γ_m. Importantly, the freedom in the factorization of Γ_m can be exploited to minimize the dimension of the subspaces corresponding to $I_1, \dots, I_N$ (i.e., making V_m and $\bar{V}_m$ as rectangular as possible, e.g., via SVD), thereby reducing the overall dimension of the H_{AIM} matrix.

At this point, even though $G(\omega)$ can be expressed exactly as a SOP, it may still have higher-order poles. This is directly related to whether H_{AIM} is diagonalizable (i.e., whether it admits a complete spectral representation). In the language of nonlinear eigenvalue problems, the eigenvalues of Eq. (4.1) need to be semisimple, i.e., the algebraic and geometric multiplicities are always equal [63], for the GF to have only simple poles. This, in turn, depends on the nature of the self-energy. For instance, when the poles of the self-energy Ω_m are real (with an infinitesimal offset from the real axis), and their residues Γ_m are Hermitian, the AIM matrix is Hermitian, which is a sufficient (but not necessary) condition for diagonalizability.

Throughout the thesis, the latter is assumed.

Thus, the diagonalization of H_{AIM} yields the desired SOP expression for the Green's function:

$$G(\omega) = \sum_{s=1}^{N+1} \frac{\left|\psi_s^R\right\rangle\left\langle\psi_s^L\right|}{\omega - z_s}, \tag{4.25}$$

where $|\psi_s^{R/L}\rangle$ are the right/left eigenvectors of Eq. (4.1), computed, according to the above discussion, as the projections of the linear H_{AIM} eigenvectors on the P_0 manifold, z_s being their eigenvalues. We have turned a nonlinear eigenvalue problem into a linear one in a larger space. Hence, starting from the poles and residues of the self-energy this procedure—the algorithmic inversion method—provides the excitation energies, lifetimes, and amplitudes (Dyson orbitals) of the system, i.e., the real and imaginary part of the poles and their residues. Furthermore, the knowledge of the Green's function as SOP allows for the analytic calculations of its moments and thus for the evaluation of integrated thermodynamic quantities [34].

Importantly, in Ref. [65] a similar construction was used to efficiently invert the Dyson equation in the context of DMFT, with applications in Refs. [32, 66, 67]. Though the building of the effective Hamiltonian H_{AIM} starting from the poles of the self-energy is similar, in the references the connection with nonlinear eigenvalue problems is only hinted. Conversely, in Sec. 4.1, we establish a clear connection between this formalism and the framework of nonlinear eigenvalue problems. This connection also allows for exploring other strategies to tackle the solution of the Dyson equation. Related approaches have also appeared recently to efficiently compute the GW self-energy and solve the Bethe-Salpeter equation [68, 69]. For example, in Ref. [68], the authors exploits the algebraic structure of the GW equations to construct a "super-matrix" $\boldsymbol{H}$ that has the same structure as the H_{AIM} presented in this work. Although the case in the reference seems relevant to the GW formalism, we have shown here that this approach is entirely general and essentially requires the self-energy to be represented as a SOP.

As already mentioned for the scalar case, the solution of the Dyson equation using the algorithmic-inversion method guarantees the exact solution of the equation given a self-energy summed over poles. This translates to a Green's function fulfilling all the sum rules implied by the Dyson equation, such as the correct normalization of the spectral function $A(\omega)$. Moreover, knowing the sum over poles for the Green's function allows us to analytically compute all the integrals necessary to calculate the frequency-integrated thermodynamic properties (see Secs. 3.4, 6.3, and 7.3 for further details and applications). Indeed, these integrals are very difficult to compute numerically, as the spectral function is a peaked function on the real axis and requires a fine sampling of frequencies. Thus, inverting the Dyson equation at each frequency can suffice to calculate accurate spectral properties [70], but it is computationally unfeasible for obtaining precise frequency-integrated properties.

Similarly to Sec. 4.2, we provide a numerical example of the extension of the AIM to the operatorial case in this section. We construct a time-ordered self-energy with four poles

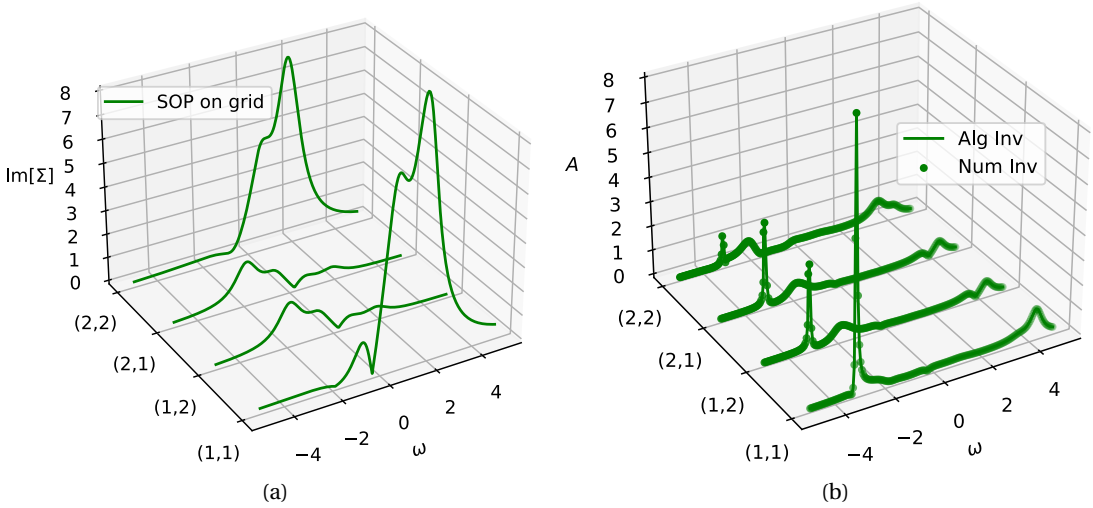

Figure 4.2: Numerical example of the extension of the algorithmic inversion method on sum over poles to the operatorial case. In panel 4.2a the spectral part of the self-energy matrix element having 4 poles. In panel 4.2b the matrix elements of the solution of the Dyson equation on grid (dotted) compared to the SOP form found with the algorithmic-inversion method and then represented on grid (continuous line).

and display its matrix elements in Fig. 4.2a. In Fig. 4.2b, we compare the matrix elements of the spectral function A obtained from the numerical (matrix-based) inversion of the Dyson equation on a grid, which is done by evaluating Σ on the grid and then inverting it, with the Green's function obtained through the algorithmic-inversion method and evaluated on the frequency grid. As in Sec. 4.2, the results are identical.

As a final note, the procedure for solving the Dyson equation for the polarizability to obtain the screened potential of Sec. 4.2 readily generalizes to the operatorial case, with scalars becoming matrices. Also, as discussed in Sec. 4.2, the AIM solves the Dyson equation exactly and thus respects all the sum rules implied by the equation.

5 Dynamical Hubbard functional

In this chapter, we introduce a novel functional of the Green's function that combines the precision of DFT for ground-state properties with the accuracy of GW for spectroscopic predictions. In particular, we design an approximation to the exchange-correlation part of the Klein functional that is the dynamical generalization of DFT+U to host a frequency-dependent screening $U(\omega)$. Furthermore, we show that the resulting self-energy comes from a localization of GW plus a double counting term. In Ch. 7, we make use of the algorithmic inversion method on the sum over poles to implement the functional form for Φ and Σ to compute the spectrum and thermodynamics of $SrVO_3$. The content of this chapter is mainly adapted from my article in Ref. [35]. Also, please note that in Ch. 2.1, we introduced the Luttinger-Ward functional. Here, we switched to the Klein functional and provide a summary of the differences in Appendix A.3. For an introduction to the DFT+U functional, please see Appendix A.5.

5.1 Hubbard manifolds

As in DFT+U, the functional that we introduce has arbitrariness in the choice of the Hubbard manifold. Indeed, the functional that we are going to design will not directly depend on the Green's function but on the projection of the Green's function onto the Hubbard manifold, $\boldsymbol{G} = P_H G P_H$, where P_H projects down to the manifold. Here, there is an exact analogy to the density matrix for DFT+U, whereas the DFT+U energy functional does not depend on the full density matrix but only on the occupations of the orbitals in the manifold.

Another important remark is that we want to maintain the rotational invariance of the functional. As mentioned in Appendix A.5, this is crucial to ensure that the functional's dependence is on the manifold and not on the specific orbitals we use to span the manifold. The easiest way to maintain such gauge is to build the functional as the trace over the degrees of freedom of the manifold, such that it is invariant under any rotation within the manifold.

The fact that the functional can only be defined if one has identified a localized manifold in the

material can be seen as a pro or a con, depending on the point of view. As also pointed out in Appendix A.5, the a priori knowledge of a region of space in which short-range interactions will be stronger than other parts of the material can be used to simplify the many-body problem. Much in the spirit of DMFT, addressing the interactions in the Hubbard (correlated) region differently from the rest of the (weakly correlated) material can improve the accuracy of the prediction while keeping the cost of the overall procedure feasible.

On the contrary, the fact that there must be a localized sub-space limits the range of application of the functional. For example, in Sec. 5.2 we see that the self-energy (of the functional) comes from a localization of GW if we can discard long-range interactions between the manifold and the rest of the material, i.e., if the (occupied) orbitals in the manifold are sufficiently localized. In practice, like in DFT+U, we apply the dynamical Hubbard functional to solids that have partially occupied d or f shells, which contribute mostly to the frontier bands [1]. Indeed, as mentioned in Appendix A.5, bands with d or f character are usually flatter compared to the others, possibly indicating that the subspace spanned is correlated, and the electrons within it are localized.

5.2 From GW to localized-GW

In this Section we want to derive a localized form for the GW self-energy starting from GW. This approach has been adapted from Ref. [71] and is similar to Refs. [72, 73].

In Appendix A.4, we derived the functional form for the GW self-energy. From Eq. A.17, we have

$$\Sigma_{GW}(\boldsymbol{r},\boldsymbol{r}',\omega) = -\int \mathrm{d}\omega' \, \frac{e^{i\omega' 0^+}}{2\pi i} G(\boldsymbol{r},\boldsymbol{r}',\omega+\omega') W(\boldsymbol{r},\boldsymbol{r}',\omega'). \tag{5.1}$$

Now, we aim to obtain a localized form of this self-energy. For simplicity, we limit the treatment to a single Hubbard site I, and the extension to multiple Hubbard sites will be discussed at the end.

Let's start by rewriting with explicit space index the Lehmann representation of the Green's function (see Sec. 2.1),

$$G(\boldsymbol{r},\boldsymbol{r}',\omega) = \sum_s \frac{\psi_s(\boldsymbol{r})\psi_s^*(\boldsymbol{r}')}{\omega - \epsilon_s \pm i0^+}, \tag{5.2}$$

where $\psi_s(\boldsymbol{r})$ are the Dyson orbitals, ϵ_s the charged excitations of the material, and $\pm i0^+$ provide the correct time ordering of the propagator. On a localized basis around a site I (labelled here with Greek letters like α, β, γ) the self energy reads

$$\langle \alpha | \Sigma(\omega) | \beta \rangle = -\sum_s \int \frac{\mathrm{d}\omega'}{2\pi i} e^{i\omega' 0^+} \int \mathrm{d}\boldsymbol{r}\, \mathrm{d}\boldsymbol{r}' \, \frac{\psi_s(\boldsymbol{r})\alpha^*(\boldsymbol{r})\, W(\boldsymbol{r},\boldsymbol{r}',\omega)\, \beta(\boldsymbol{r}')\psi_s^*(\boldsymbol{r}')}{\omega+\omega'-\epsilon_s \pm i0^+}. \tag{5.3}$$

[1] By frontier bands, we mean the bands around the Fermi surface or the gap of the material.

Introducing the four-point notation for the screened potential [20]

$$W^{ss}_{\alpha\beta}(\omega) = \langle \alpha s | W(\omega) | s\beta \rangle = \int \mathrm{d}\boldsymbol{r}\,\mathrm{d}\boldsymbol{r}'\,\alpha^*(\boldsymbol{r})\psi^*_s(\boldsymbol{r}')W(\boldsymbol{r},\boldsymbol{r}',\omega)\psi_s(\boldsymbol{r})\beta(\boldsymbol{r}'), \tag{5.4}$$

the self-energy can be rewritten as

$$\langle \alpha | \Sigma(\omega) | \beta \rangle = -\sum_s \int \frac{\mathrm{d}\omega'}{2\pi i} e^{i\omega' 0^+} \frac{W^{ss}_{\alpha\beta}(\omega)}{\omega + \omega' - \epsilon_s \pm 0^+}. \tag{5.5}$$

Then, as in Refs. [71, 73, 72], we separate each Dyson orbital into an itinerant (delocalized) component and a localized one, $|\psi_s\rangle = |s_{\mathrm{it}}\rangle + \sum_\gamma |\gamma\rangle\langle\gamma|s\rangle$. The screened potential is separated in

$$W^{ss}_{\alpha\beta}(\omega) = \left\langle \alpha \left(\langle s_{\mathrm{it}}| + \sum_\gamma \langle s|\gamma\rangle\langle\gamma| \right) \middle| W(\omega) \middle| \left(|s_{\mathrm{it}}\rangle + \sum_{\gamma'} \langle\gamma'|s\rangle|\gamma'\rangle \right) \beta \right\rangle \tag{5.6}$$

$$= W^{s_{\mathrm{it}}s_{\mathrm{it}}}_{\alpha\beta}(\omega) + \sum_\gamma \left[W^{\gamma s_{\mathrm{it}}}_{\alpha\beta}(\omega) + W^{s_{\mathrm{it}}\gamma}_{\alpha\beta}(\omega) \right] + \sum_{\gamma,\gamma'} W^{\gamma\gamma'}_{\alpha\beta}(\omega), \tag{5.7}$$

where, since we suppose the screened interaction to be short-range, we discard the first three terms. Owing to the localization of the basis of the site, we can approximate the fourth term as [73]:

$$W^{\gamma\gamma'}_{\alpha\beta}(\omega) = \int \mathrm{d}\boldsymbol{r}\,\mathrm{d}\boldsymbol{r}'\,\alpha^*(\boldsymbol{r})\gamma^*(\boldsymbol{r}')W(\boldsymbol{r},\boldsymbol{r}')\gamma'(\boldsymbol{r})\beta(\boldsymbol{r}') \approx \delta_{\alpha\gamma'}\delta_{\gamma\beta}W^{\beta\alpha}_{\alpha\beta}(\omega). \tag{5.8}$$

Discarding the first three terms in Eq. (5.7), and using Eq. (5.8), we can write the localized form of the self-energy from Eq. (5.5)

$$\langle \alpha | \Sigma_{GW_{\mathrm{Loc}}}(\omega) | \beta \rangle = -\sum_s \int \frac{\mathrm{d}\omega'}{2\pi i} e^{i\omega' 0^+} \frac{\langle \alpha|s\rangle\langle s|\beta\rangle}{\omega + \omega' - \epsilon_s \pm i0^+} W^{\beta\alpha}_{\alpha\beta}(\omega). \tag{5.9}$$

By specifying explicitly the site-orbital dependence, $|\alpha\rangle = |I,m\rangle$ and $|\beta\rangle = |J,m'\rangle$, and focusing on on-site contributions—off site contributions would give a $+V$-like term [71]—, the equation above can be rewritten as

$$\langle I,m | \Sigma_{GW_{\mathrm{Loc}}}(\omega) | I,m' \rangle = -\sum_s \int \frac{\mathrm{d}\omega'}{2\pi i} e^{i\omega' 0^+} \frac{\langle I,m|s\rangle\langle s|I,m'\rangle}{\omega + \omega' - \epsilon_s \pm i0^+} W^{Im',Im}_{Im,Im'}(\omega). \tag{5.10}$$

Similarly to the context of DFT+U of Refs. [73, 71], by introducing the average

$$U(\omega) = \frac{1}{(2l+1)^2} \sum_{m,m'} W^{Im',Im}_{Im,Im'}(\omega), \tag{5.11}$$

the above equation reads approximately:

$$\langle I,m | \Sigma_{GW_{\mathrm{Loc}}}(\omega) | I,m' \rangle = -\sum_s \int \frac{\mathrm{d}\omega'}{2\pi i} e^{i\omega' 0^+} \frac{\langle I,m|s\rangle\langle s|I,m'\rangle}{\omega + \omega' - \epsilon_s \pm i0^+} U(\omega). \tag{5.12}$$

Finally summing over the s-index and recalling the Lehmann representation for the Green's function, for a single site the localized-GW self-energy reads

$$\boldsymbol{\Sigma}_{GW_{\text{Loc}}} = -\int \frac{\mathrm{d}\omega'}{2\pi i} e^{i\omega' 0^+} U(\omega') \boldsymbol{G}(\omega+\omega'), \tag{5.13}$$

where $\boldsymbol{G}_{mm'} = \langle I, m | G | I, m' \rangle$ or $\boldsymbol{G} = P_H G P_H$, as in the rest of the Chapter.

5.3 Functional for Localized GW

In this section, we introduce the localized-GW functional designed in this thesis. We focus on building a Φ functional that yields the localized-GW self-energy derived in Sec. 5.2.

As explained in Sec. 2.3 and Appendix A.4, the Φ functional is such that

$$\frac{\delta \Phi}{\delta G(\omega)} = 2\pi i \Sigma(\omega). \tag{5.14}$$

If we partition the space into a Hubbard manifold and an orthogonal remainder, in full generality, the Green's function operator can be written as

$$G = \begin{pmatrix} P_H G P_H & 0 \\ 0 & P_R G P_R \end{pmatrix}. \tag{5.15}$$

Due to the orthogonality between the two spaces, any variation over G of a functional f is split into

$$\frac{\delta f}{\delta G(\omega)} = P_H \frac{\delta f}{\delta \boldsymbol{G}} P_H + P_R \frac{\delta f}{\delta (P_R G P_R)} P_R, \tag{5.16}$$

where we have used the definition of $\boldsymbol{G} = P_H G P_H$ in agreement with the rest of the chapter. Thus, a functional Φ that depends only on $\boldsymbol{G}$ yields a self-energy which is nonzero only in the manifold,

$$\frac{\delta \Phi[\boldsymbol{G}]}{\delta G(\omega)} = P_H \Sigma P_H. \tag{5.17}$$

From the argument above and a direct derivation, the functional

$$\tilde{\Phi}_{GW_{\text{Loc}}}[\boldsymbol{G}] = -\frac{1}{2} \int \frac{d\omega}{2\pi i} \frac{d\omega'}{2\pi i} e^{i\omega 0^+} e^{i\omega' 0^+} U(\omega') \operatorname{Tr}\{\boldsymbol{G}(\omega+\omega')\boldsymbol{G}(\omega)\} \tag{5.18}$$

yields the localized-GW self-energy of Eq. 5.13 within the manifold and zero outside.

Notably, the functional $\tilde{\Phi}_{GW_{\text{Loc}}}$ is particle-conserving since it reduces to GW_0 (see Appendix A.4 for details) within the Hubbard manifold and is zero outside. Furthermore, the continuity equation derived in Sec. 2.2 is a local property.

Though true, if we want to use this functional as a corrective term for semi-local DFT, we face a double counting problem. Both the approximate DFT functional and the localized-GW

self-energy model the electron-electron interaction in the Hubbard manifold. This is similar to, e.g., DFT+U, as shown in Appendix A.5. Thus, the strategy to estimate a double counting term is to make a mean-field approximation to the functional we have designed, as we did in Appendix A.5 for the Hubbard functional.

To make the functional static, we may consider a static screening $U(\omega) = U_c$. By performing the integrations,$\tilde{\Phi}_{GW_{\text{Loc}}}$ with a static screening reduces to:

$$\tilde{\Phi}_{GW_{\text{Loc}}}[\boldsymbol{G}] \approx -\frac{U_c}{2}\,\text{Tr}\{\boldsymbol{n}^2\}, \tag{5.19}$$

where, as in Appendix A.5, $\boldsymbol{n}$ is the projection of the density matrix on the Hubbard manifold, i.e., $\boldsymbol{n} = \int \frac{d\omega}{2\pi i} e^{i\omega' 0^+} \boldsymbol{G}(\omega)$. By direct comparison to the definition of the double-counting for the DFT+U functional from Equations (A.21) and (A.22), the double counting for the localized-GW functional is:

$$E^{\text{dc}}_{GW_{\text{Loc}}} \approx \frac{U_c}{2}\,\text{Tr}\,\boldsymbol{n}. \tag{5.20}$$

Writing the above term as the integral of the Green's function of the manifold, the full localized-GW functional reads

$$\Phi_{GW_{\text{Loc}}}[\boldsymbol{G}] = \frac{1}{2}\int \frac{d\omega}{2\pi i}\frac{d\omega'}{2\pi i}\, e^{i\omega 0^+} e^{i\omega' 0^+} U(\omega')\,\text{Tr}\{\boldsymbol{G}(\omega+\omega')\,[\delta(\omega - c)\boldsymbol{I} - \boldsymbol{G}(\omega)]\}, \tag{5.21}$$

where c is the constant that adjusts the double counting.

Please note that this functional:

(i) is rotationally invariant,

(ii) with a static screening it simplifies to the DFT+U functional of Dudarev, et al., of Ref. [33],

(iii) yields a localized-GW self-energy plus a double counting term.

For all these reasons we call $\Phi_{GW_{\text{Loc}}}$ a dynamical Hubbard functional.

The full derivative of the dynamical Hubbard functional reads:

$$\boldsymbol{\Sigma}^c_{GW_{\text{Loc}}}(\omega) = -\int \frac{d\omega'}{2\pi i} e^{i\omega' 0^+} U(\omega')\boldsymbol{G}(\omega+\omega') + \frac{1}{2}U(c)\boldsymbol{I}, \tag{5.22}$$

where $U(c)$ helps to adjust the double counting, and we have put a label c to distinguish it from $\boldsymbol{\Sigma}_{GW_{\text{Loc}}}$ of Eq. (5.13), which is the same but without the double counting term.

5.4 Adjusting the double counting

In this section, we provide a final expression for the Dynamical Hubbard functional and its self-energy, $\Phi_{GW_{\text{Loc}}}$ and $\boldsymbol{\Sigma}_{GW_{\text{Loc}}}$, by fixing the gauge for the double counting.

As stated in Sec. 5.3, we can estimate the double counting by calculating the average of the mean-field limit of the functional, either on $\Phi_{GW_{\text{Loc}}}$ or on $\boldsymbol{\Sigma}_{GW_{\text{Loc}}}$. Since it is a GW approximation on the manifold, as can be verified by inspection from Eq. (5.12) the mean-field limit for $\boldsymbol{\Sigma}_{GW_{\text{Loc}}}(\omega)$, defined as $\omega \to \infty$, is the Fock term,

$$\boldsymbol{\Sigma}_{GW_{\text{Loc}}}(\omega) \xrightarrow[\omega\to\infty]{} \boldsymbol{n} U_\infty. \tag{5.23}$$

Then, the average,

$$\left\langle \boldsymbol{\Sigma}_{GW_{\text{Loc}}} \right\rangle \approx \langle \boldsymbol{n} \rangle U_\infty, \tag{5.24}$$

would yield an approximately mean-field double counting with U_∞ as the U coupling.

To see this, we perform the limit $c \to \infty$ in the expression for $\Phi_{GW_{\text{Loc}}}$ of Eq. (5.21):

$$\bar{\Phi}_{GW_{\text{Loc}}} = \Phi^{c\to\infty}_{GW_{\text{Loc}}} = \frac{U_\infty}{2} \operatorname{Tr} \boldsymbol{n} + \tilde{\Phi}_{GW_{\text{Loc}}}. \tag{5.25}$$

Calling $n = \operatorname{Tr} \boldsymbol{n}$, in agreement with Appendix A.5, and adding and subtracting an n^2 term, the equation above becomes

$$\bar{\Phi}_{GW_{\text{Loc}}} = \left(\frac{U_\infty}{2} n^2 + \tilde{\Phi}_{GW_{\text{Loc}}} \right) - E_{\text{dc}}, \tag{5.26}$$

with $E_{\text{dc}} = \frac{U_\infty}{2} n(n-1)$. Thus, as mentioned in Appendix A.5, if we replace the 1 with the average $\langle \boldsymbol{n} \rangle$, we obtain the around mean-field double counting.

Indeed, the derivative of the functional $\bar{\Phi}^{\text{AMF}}_{GW_{\text{Loc}}}$ where we have used an around mean field double counting, $E^{\text{AMF}}_{\text{dc}}$, yields the self-energy:[2]

$$\boldsymbol{\Sigma}_{GW_{\text{Loc}}}(\omega) + U_\infty \langle \boldsymbol{n} \rangle \boldsymbol{I}. \tag{5.27}$$

In this thesis, we have chosen the fully localized limit double counting. Nevertheless, we have understood that a good choice to fix the c gauge of $\Phi_{GW_{\text{Loc}}}$ is $c \to \infty$ or $U(c) = U_\infty$. This amounts to a double counting of Fock-like interactions, as seen from the fully localized limit perspective.

Finally, the functional that we use in this thesis is $\bar{\Phi}_{GW_{\text{Loc}}} = \Phi^{c\to\infty}_{GW_{\text{Loc}}}$ as defined in Eq. (5.25) and its self-energy,

$$\bar{\boldsymbol{\Sigma}}_{GW_{\text{Loc}}}(\omega) = -\int \frac{d\omega'}{2\pi i} e^{i\omega' 0^+} U(\omega') \boldsymbol{G}(\omega + \omega') + \frac{1}{2} U_\infty \boldsymbol{I}. \tag{5.28}$$

[2] taking into account the 1/2 difference in the derivative wrt the fully localized limit, as in the note in Appendix A.5.

6 AIM-SOP for homogeneous systems in GW

In this chapter, we use the algorithmic inversion method on the sum over poles (AIM-SOP) to compute spectroscopic and thermodynamic quantities of the homogeneous electron gas at the G_0W_0 level for several densities of the gas.

Drawing a parallelism with standard implementations of semi-local DFT for materials science, where numerically accurate spectral and thermodynamic quantities are computed, the fundamental goal of the AIM-SOP approach is to provide a similar framework in a Green's function (dynamical) formalism.

A test case example of how the AIM-SOP framework can be shaped and applied to the study of the homogeneous electron gas is the scope of the next sections, also highlighting the difference from the other approaches in the field. We stress that the AIM-SOP framework is designed to be applied to any type of Green's function formalism and is not limited to G_0W_0 calculations. Here, we do not make use of the functional developed in Ch. 5, which is instead used for the calculations on a real crystal in Ch. 7.

As already stated in the thesis, the electron gas is a simplified case study for the AIM-SOP since all one-particle (dynamical) operators are diagonal on the plane-wave basis, resulting in a treatment of scalar functions over frequency instead of operators.

Since we calculate propagators on the real axis, we can easily access spectral (frequency-dependent) properties (see Sec. 6.4.1). The calculation of frequency-integrated ground-state quantities, such as occupation numbers, total energies, and thermodynamic quantities in general, can be obtained directly from the SOP representation of the spectral quantities computed in the procedure (see Sec. 6.4.2). While thermodynamic properties are usually obtained via additional calculations on the imaginary axis [74, 75, 76], here spectral properties and integrated quantities are obtained simultaneously using the SOP representation of propagators computed on the real axis (see Sec. 6.1).

Although some quantities computed using the free-propagator G_0 have known analytical expressions, such as the irreducible polarizability P_0 expressed via the Lindhard function [77,

43], here we explicitly recompute all the quantities needed to evaluate the GW self-energy, making the treatment suitable also for self-consistent calculations. Therefore, in the following, the only assumption we make is to consider the Green's function as represented on SOP.

The content of this Chapter is mainly taken from my article [34].

6.1 Computing spectral and thermodynamic quantities jointly

We would like to point out that due to the complexity of dealing with dynamical quantities, different methodological approaches have been developed for calculating spectral and thermodynamic quantities (such as energies, number of particles, and chemical potentials). Real-axis calculations are commonly used to compute frequency-dependent spectral properties [78, 79, 80], while imaginary-axis formalism is typically employed for computing frequency-integrated thermodynamic properties [76, 81, 30, 82, 83, 84].

The difference between the two approaches originates from the analytical structure of the Green's function, specifically its branch cuts on the real axis [53]. This results in the spectral function varying strongly for real frequencies and making its integration difficult. Thus, real-axis approaches are often limited to predicting spectral properties. Conversely, sampling the Green's function along the imaginary axis (i.e., away from its poles) is a good way to obtain fast-converging frequency integrals, but has drawbacks when attempting to obtain the function on the real axis by analytic continuation.

In this context, methods for performing analytic continuation range from the use of Padè approximants [74, 85, 84, 62] to maximum-entropy methods [86, 87], usually with a stochastic sampling of the Green's function in the latter case.

As an example, in a recent work on the homogeneous electron gas [43], Kutepov et al. [85] managed to obtain a precise quasi-particle band using Padè approximants (although with larger error bars on the position of satellites). Additionally, in a series of papers [56, 55, 88, 89], von Barth and coworkers have proposed a formalism that can handlespectra and thermodynamics together for the homogeneous electron gas by modeling the spectral function in frequency-momentum space using Gaussians with k-parametrized centers (quasi-particle energies), broadening (weights), and satellites. However, due to its model nature, the approach does not easily offer the flexibility to target realistic systems or extend it to embedding problems in general.

As mentioned, in this chapter, we use the algorithmic-inversion method on sum over poles to address the simultaneous calculation of accurate spectral and thermodynamic quantities. Within AIM-SOP, dynamical (frequency-dependent) self-energies are represented as a sum over poles (see Ch. 3), and the exact solution of the Dyson equation at all frequencies is found via a matrix diagonalization (see Ch. 4). The transformation of a frequency-dependent propagator into a SOP via a representation of its spectral function on a target basis set is

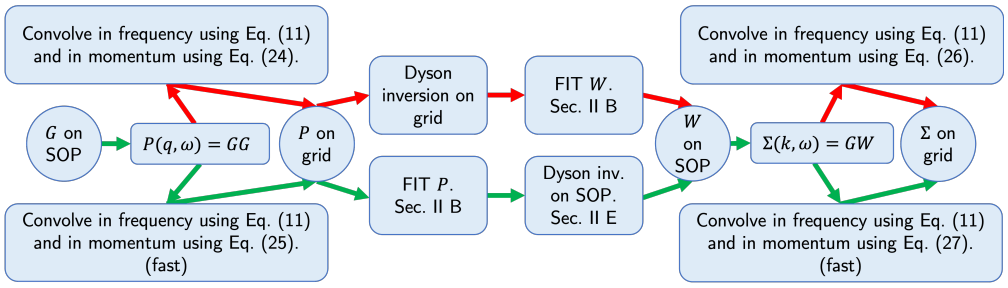

Figure 6.1: Flow chart representing different strategies for the calculation of the self-energy given a Green's function G on SOP as input for the `heg_sgm.x` code. The strategy used in this article is highlighted with green lines.

greatly improved with the use of n-th order generalized Lorentzians as a basis with improved decay properties (Sec. 3.3). The SOP form allows one to compute convolutions and moments of propagators analytically for the calculation of spectral and thermodynamic properties (Sec. B.2). Due to the fulfillment of all sum rules implied by the Dyson equation (Sec. 4.2), we show that the AIM-SOP method is crucial for obtaining accurate frequency-integrated quantities in a real-axis (spectrally oriented) formalism. We consider the paradigmatic case of the homogeneous electron gas (HEG), treated at the G_0W_0 level for r_s ranging from 1 to 10 [90, 91, 92].

6.2 HEG propagators on the real frequency axis

In order to solve a one-shot G_0W_0 cycle for the spin-unpolarized HEG, we first need to compute the irreducible polarizability at the independent-particle (or RPA) level, according to the integral (see also Appendix A.4 for an introduction to GW):

$$P(q,\omega) = 2\int \frac{d\mathbf{k}}{(2\pi)^3}\int \frac{d\omega'}{2\pi i}\, G(|\mathbf{k}+\mathbf{q}|,\omega+\omega')G(k,\omega'), \tag{6.1}$$

where $k = |\mathbf{k}|$ and $q = |\mathbf{q}|$ are the moduli of the electron and transferred quasi-momenta, respectively.

To compute Eq. (6.1), the frequency integral (convolution) is performed analytically according to Eq. (3.12). Then, we integrate numerically in spherical coordinates by performing the variable change $x = |\mathbf{k}+\mathbf{q}|$ on the azimuthal angle of $\mathbf{k}$:

$$P(q,\omega) = \frac{2}{q(2\pi)^2}\int_0^{+\infty} dk\, k \int_{|k-q|}^{|k+q|} dx\, x \int \frac{d\omega'}{2\pi i}\, G(x,\omega+\omega')G(k,\omega'), \tag{6.2}$$

which allows for the pre-calculation of the analytical convolutions on the two-dimensional (x,k) grid, instead of on the three-dimensional (k,q,θ) space. Exploiting the parity of $P(\omega)$, it is also possible to limit the $\mathbf{k}$ integration to the occupied states (see Appendix C.2). The

numerical integration on the momentum is performed using the trapezoidal rule, which, despite its simplicity, ensures exponential convergence for decaying functions [93].

In order to have a SOP representation for the screened potential W, we transform the polarizability calculated on a frequency grid (at a fixed momentum q) to a SOP using a NNLS fitting, following the procedureoutlined in Sec. 3.3. We then solve the Dyson equation using the algorithmic inversion for the polarizability (see Sec. 4.2) to obtain a SOP for W and use it for the GW integral.

An alternative approach would be to solve the Dyson equation on a grid (which, due to homogeneity, is an algebraic inversion) and then transform W to a SOP representation. However, even assuming an exact interpolation for the SOP of W on the calculated frequencies (where the Dyson equation is solved on th grid), this SOP would suffer from not having solved the Dyson equation for all other frequencies. Instead, the SOP obtained from the algorithmic inversion provides an exact solution of the Dyson equation at all frequencies (see Ch. 4). Thus, the sum rules implied by the Dyson equation (e.g., moments of the spectral function) are all obeyed by the SOP obtained from the algorithmic inversion, being the exact solution at all frequencies. Conversely, this is not true for the grid inversion where the solution is exact only for isolated frequencies.

Concerning the self-energy integral

$$\Sigma(k,\omega) = \Sigma_x(k) + \frac{1}{(2\pi)^3}\int d\mathbf{q}\int_{-\infty}^{+\infty}\frac{d\omega'}{2\pi i}\,G(|\mathbf{k}+\mathbf{q}|,\omega+\omega')\,W_{\text{corr}}(q,\omega'), \tag{6.3}$$

where $W_{\text{corr}} = W - v_c$, we can still use Eq. (3.12) since we have the SOP representation of W. Again, in Eq. (6.3), we perform the $x = |\mathbf{k}+\mathbf{q}|$ change of variable, obtaining

$$\Sigma(k,\omega) = \Sigma_x(k) + \frac{1}{k(2\pi)^2}\int_0^{+\infty} dq\,q\int_{|k-q|}^{|k+q|} dx\int\frac{d\omega'}{2\pi i}\,G(x,\omega+\omega')\,W_{\text{corr}}(q,\omega'), \tag{6.4}$$

which allows for fewer convolutions (as for the polarizability integral) and uses trapezoidal weights as in Eq. (6.2) for the momentum integration. The solution of the Dyson equation for the Green's function using the algorithmic inversion, and the calculation of frequency-integrated (thermodynamic) quantities, is discussed in the next section.

In Fig. 6.1, we show the overall flow chart that describes the process of going from the knowledge of the initial Green's function to the calculation of the corresponding self-energy (for the HEG in the GW approximation) as implemented in the `heg_sgm.x` program of the `AGWX` suite [94], using the SOP approach. In the red path, the Dyson equations are solved on grids, while in the green path, we highlight the protocol followed in the present work. The crucial difference between the two approaches is the use of the algorithmic-inversion method to solve the Dyson equation exactly

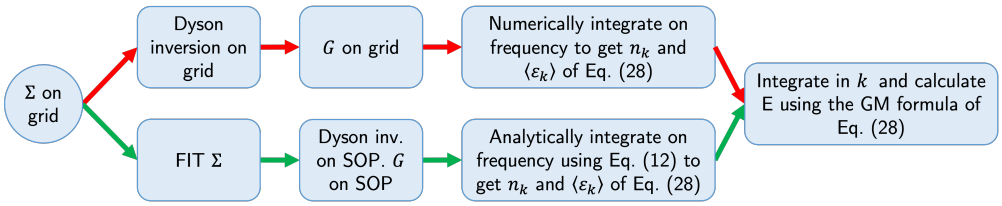

Figure 6.2: Flow chart representing different strategies for the calculation of the total-energy given a self-energy Σ, or a spectral function A, on a frequency grid as input for the `heg_sgm.x` code. The strategy used in this article is highlighted with green lines.

6.3 Frequency-integrated quantities and thermodynamics

Having obtained the self-energy on a frequency grid following the procedure described in Sec. 6.2, we can evaluate the Green's function together with some related frequency-integrated quantities. As mentioned, the SOP approach plays a central role here, enabling the possibility of performing analytical integrals for the moments of G, such as those involved in the Galitskii-Migdal expression for the total energy [see Eq. (6.5) below], and thus obtaining accurate thermodynamic (frequency-integrated) quantities. Moreover, the use of the algorithmic-inversion method allows for the exact solution of the Dyson equation for the Green's function at all frequencies. Indeed, the conservation of all sum rules (implied by the Dyson equation, see Sec. 3.1) guaranteed by the AIM-SOP is fundamental when calculating the occupied moments of the spectral function.

As an example, the normalization condition of the spectral function is automatically satisfied when G on SOP is obtained using the algorithmic inversion, and this allows us to avoid fitting constraints that would be required if a grid inversion were used. Moreover, the exact solution of the Dyson equation provided by the algorithmic inversion yields an equality between the renormalization factor Z calculated via the derivative of the self-energy at $k = k_f$ and $\omega = \epsilon_f$, and the value obtained using the discontinuity of the occupation factor n_k at $k = k_f$, given by the moment of the occupied spectral function.

In order to use the AIM-SOP to obtain G represented as SOP, we obtain the SOP representation of the self-energy by performing a NNLS fitting of $\mathrm{Im}\Sigma(\omega)$ (see Sec. 3.3). Then, to compute the total energy from the knowledge of the Green's function G, we use the Galitski-Migdal expression (see Appendix A.2 for details),

$$\begin{aligned}\frac{E}{V} &= \int \frac{d\mathbf{k}}{(2\pi)^3}\left[\int_{-\infty}^{\mu} d\omega\, \omega A(k,\omega) + \frac{k^2}{2}\int_{-\infty}^{\mu} d\omega A(k,\omega)\right] \\ &= \int \frac{d\mathbf{k}}{(2\pi)^3}\left[\langle\epsilon_k\rangle + \frac{k^2}{2} n_k\right],\end{aligned} \tag{6.5}$$

in Hartree units. In this expression, the frequency integrals are performed using the SOP for G, and exploiting Eq. (3.13) with $m = 1$ and $m = 0$ for the first and second terms, respectively. Here, n_k is the k-resolved occupation function, which sums to the total number of particles when

integrated over momentum, and $\langle \epsilon_k \rangle$ is the occupied band energy, i.e., the first momentum of the occupied spectral function.

For both $m = 0$ and $m = 1$ moments, the equality between the moments of the Green's function and the moments of the occupied spectral function, Eq. (3.13) and Eq. (B.5), is assured by having used the algorithmic inversion when obtaining the SOP for the Green's function. Indeed, the knowledge of the self-energy on SOP and the use of the algorithmic inversion for solving exactly the Dyson equation ensures that the spectral function

$$A = \frac{1}{\pi} \frac{|\mathrm{Im}\Sigma(\omega)|}{[\omega - \epsilon_0 - \mathrm{Re}\Sigma(\omega)]^2 + [\mathrm{Im}\Sigma(\omega)]^2}, \tag{6.6}$$

decays at least as $\frac{\mathrm{Im}\Sigma}{\omega^2} = o(\omega^{-3})$, thereby making the first two occupied moments (see Sec. 3.4) converge. Additionally, even if we do not use the algorithmic inversion method to get G from Σ, the use of 2nd-order Lorentzians from the representation of the spectral function A provides the identity between Eq. (3.13) and Eq. (B.5), as the zeroth and first moments are well-defined (see Sec. 3.4 for further reference).

Similarly to the discussion in Sec. 6.2, the SOP approach combined with the algorithmic inversion allows one to follow the workflow highlighted by the green path in Fig. 6.2. The results presented in Sec. 6.4 are obtained using an implementation of the above approach in the `-heg_sgm.x` program of the `AGWX` suite [94].

6.4 Results at $r_s = 4$

In this section, we discuss the results obtained by applying the SOP approach to the one-shot G_0W_0 calculation in the HEG. First, we extensively discuss the $r_s = 4$ case, which is also one of the most studied in the literature. Then, in Sec. 6.5, we provide results for densities ranging from $r_s = 1$ to $r_s = 10$.

6.4.1 Spectral propagators on the real axis

We start by considering the screened potential $W(q,\omega)$ computed at the G_0 level. In Fig. 6.3, we compare the imaginary part of W (divided by π and taken without sign), calculated following the procedure described in Sec. 6.3 (right panel), with its analytic expressions at zero broadening ($\delta = 0$, left panel) and at finite Lorentzian broadening ($\delta = 10^{-5}\,\epsilon_f$, center panel). While for $\delta = 0$ the analytic expression for the polarizability (and consequently for W) is well-known [77], at finite δ, the derivation of an analytic time-ordered form for W is given in Sec. C.1 of the Appendix. Notice that at $\delta = 0$, the plasmonic band for small q-vectors (dashed line) has to be calculated numerically since it comes from a set of delta functions [95]. The computation of the plasmonic band of Fig. 6.3 for $q/k_f < 1$ is obtained by numerically finding the roots of the plasmonic equation (e.g., Eq. 15.11 of Ref. [77]), using the analytic form for the polarizability at zero broadening.

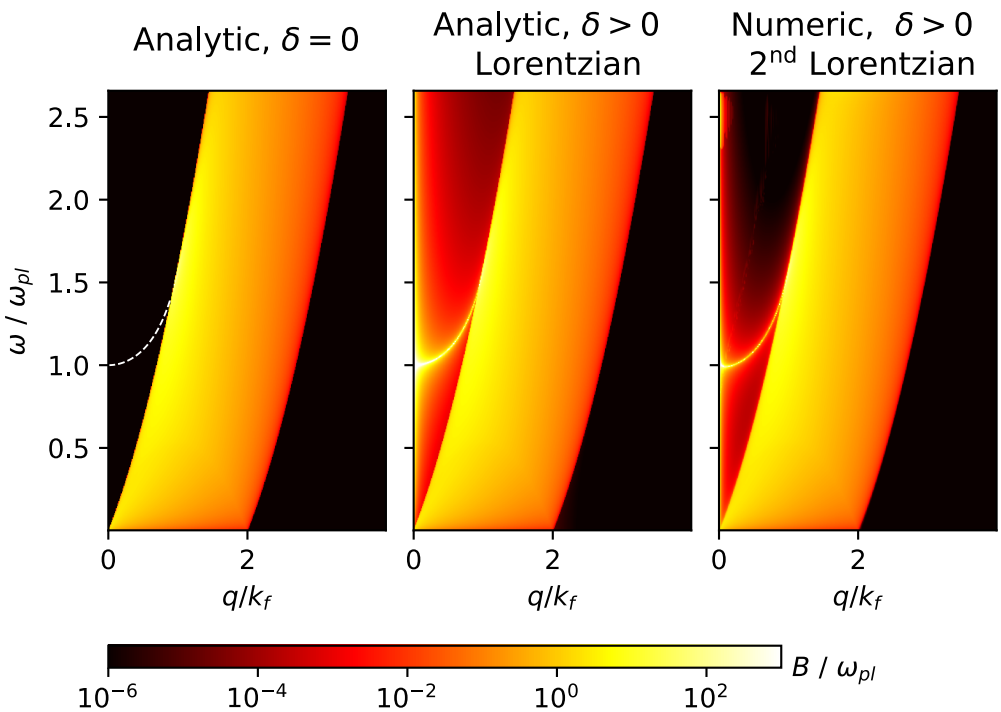

Figure 6.3: Imaginary part (divided by π and taken without sign) of the screened potential of the HEG at $r_s = 4$ in a one-shot G_0W_0 calculation. Momenta are in units of the Fermi momentum and energies in units of the plasma frequency of the gas at the specified density. The color map is logarithmic, and values $< 10^{-6}$ and $> 10^3$ are mapped to 10^{-6} and 10^3, respectively. Left panel: analytic result at zero broadening ($\delta = 0$). The functional form for the color plot is taken from Ref. [77]. The plasmonic band (dashed line) is calculated numerically, see Sec. 6.4.1 for details. Central panel: analytic result at finite (Lorentzian) broadening ($\delta = 10^{-5}\,\epsilon_f$), see Sec. C.1 of the Appendix for details. Right panel: numerical results obtained using SOP with 2nd order Lorentzians ($\delta = 0.000741\,\epsilon_f$), following the flow chart of Fig. 6.1, and then representing it on grid.

Overall, based on the plot comparison, we can qualitatively infer that the SOP approach, along with its numerical implementation, is effectively computing and representing the dynamical screened potential across a range of different values of q. The plot also shows that the numerically calculated W using second-order Lorentzians ($\delta = 0.000741\,\epsilon_f$) is sharper than the analytic form with a simple Lorentzian broadening ($\delta = 10^{-5}\,\epsilon_f$), despite the latter having a smaller δ. This further emphasizes that the use of second-order Lorentzians for G_0 can be viewed as a convergence accelerator to the $\delta \to 0$ limit (see Sec. 3.2).

Next, we examine the numerical procedures for the self-energy by directly looking at the G_0W_0 spectral function in Fig. 6.4. This is obtained by evaluating Eq. (6.4), which represents the self-energy on SOP with 2nd order Lorentzians, using the algorithmic inversion for the self-energy, and then evaluating the Green's function on a frequency grid. Focusing on the lower satellite as well as the quasi-particle band, we can see that Fig. 6.4 compares well with Refs. [95, 83].

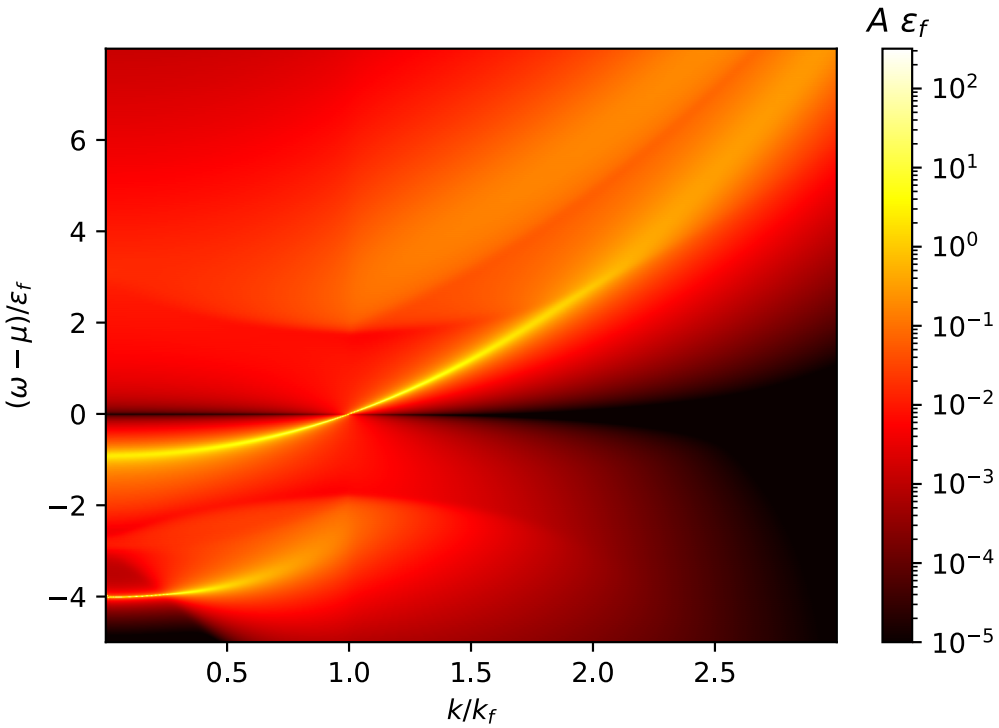

Figure 6.4: Spectral function of the HEG at $r_s = 4$ from a G_0W_0 calculation. The Fermi energy is $\epsilon_f = \frac{k_f^2}{2m_e}$ with k_f the Fermi momentum. $\mu = \epsilon_f(1-0.0545)$ is the chemical potential. The scale of the color-map is logarithmic.

Note that, unlike Ref. [83], we use a logarithmic scale to represent the intensity of the spectral function to highlight its structure. The plasmaron peak [95] is very visible for small momenta where the quasi-particle band broadens, while the satellite band in the occupied-frequency range ($\omega < \mu$) is sharper. As k approaches k_f, the plasmaron broadens, and the quasi-particle band becomes more peaked. At $k = k_f$, the spectral function presents the typical metallic divergence along the quasi-particle band, and occupied and empty satellites are almost of the same weight (see also Fig. 6.6 for details of the spectral functions at selected k), in agreement with Ref. [56]. For $k > k_f$, satellites coming from empty states ($\omega > \mu$) become dominant along with the quasi-particle band.

6.4.2 Frequency integrated quantities and thermodynamics

We now study the convergence and stability of the total energies. Following the prescription of Sec. 6.3, we use the spectral function on SOP obtained in Sec. 6.4.1, Eq. (3.13), to get analytically the occupation number n_k and the occupied-band energy ϵ_k (see Sec. 6.3). Finally, we numerically integrate the momenta of Eq. (6.5) to obtain the total energy.

To perform the convergence study on the total energy, we follow the approach described in Appendix C.4, which consists of converging all parameters for the calculation separately. Being

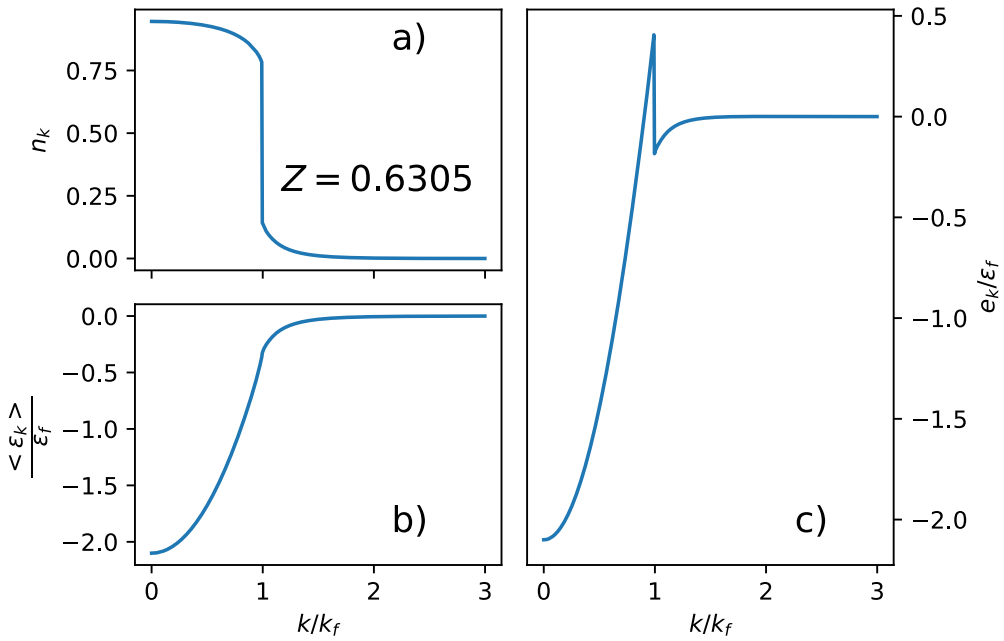

Figure 6.5: Selected frequency integrated quantities from a G_0W_0 calculation of the HEG at $r_s = 4$. Panel (a): the occupation number in arbitrary units as a function of the momentum k together with the renormalization factor (discontinuity of n_k). Panel (b): the occupied band energy $\langle\epsilon_k\rangle$ as a function of k (see Sec. 6.3 for details). Panel (c): the Galitzki-Migdal total-energy resolved over k-contributions e_k, according to the rhs of Eq. (6.5) as function of the momentum k. k_f and ϵ_f are the Fermi momentum and energy respectively.

the HEG a metal, the use of the algorithmic-inversion method to obtain a spectral function that obeys all sum rules (implied by the Dyson equation, see Sec. 4.2 for details), including the normalization condition for the spectral function, is crucial for obtaining well-converged results. Indeed, the Luttinger discontinuity of n_k makes the value of the total energy from the Galitzki-Migdal very sensitive to the converging parameters.

In Fig. C.3, we show the convergence study for the correlation energy per particle (total energy minus Fock-exchange): the convergence value for $r_s = 4$ is 0.0381 ± 0.0003 Ha, in agreement with Refs. [76] (with a difference of 0.0003 Ha), where calculations were done along the imaginary axis. In panel (a) of Fig. 6.5, we plot n_k, and in panel (b), $\langle\epsilon_k\rangle$ (as defined in Sec. 6.3). The occupation number n_k presents a sharp Luttinger discontinuity, which indicates that the broadening used in Eq. (6.4) is well-controlled and does not spoil the quality of the results. The renormalization factor in panel (a), $Z = 0.6305$, (calculated using the frequency derivative SOP self-energy at $k = k_f$ and $\omega = \epsilon_f$, see Sec. 6.3) compares well with Refs. [90, 56, 88, 96] (where we extrapolate Z from graphs when necessary).

In panel (c) of Fig. 6.5, we plot the total energy resolved over k-contributions e_k [rhs of Eq. (6.5)]. As previously mentioned, due to the presence of the Luttinger discontinuity, this function is sharp and thus difficult to integrate, in contrast to, for example, the RPA-Klein-energy

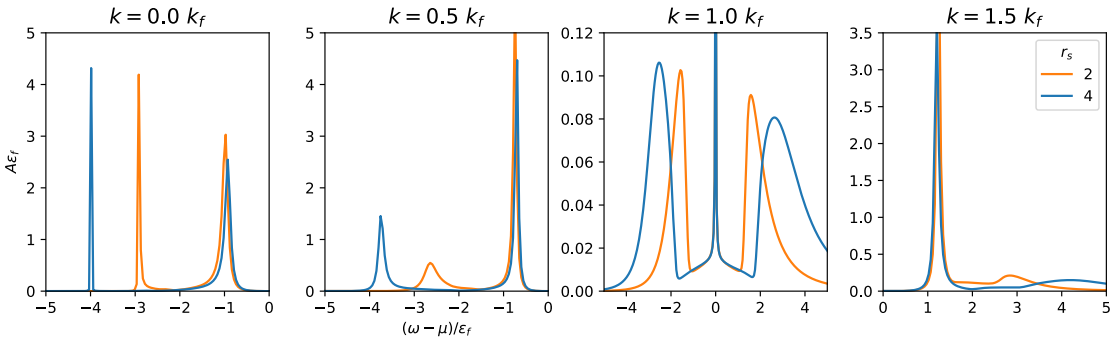

Figure 6.6: Spectral functions of the HEG at selected k points (indicated on top) for $r_s = 2$ and $r_s = 4$. Energies are in units of ϵ_f and momenta of k_f.

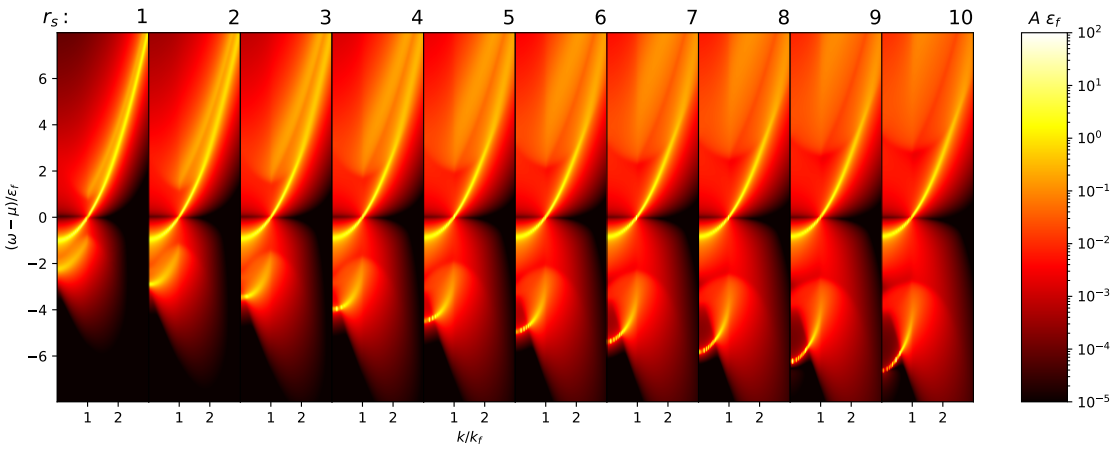

Figure 6.7: Spectral functions of the HEG at several densities. At the top r_s specifies the density. The Fermi energy is $\epsilon_f = \frac{\hbar^2 k_f^2}{2m_e}$ with k_f the Fermi momentum. μ is the chemical potential. The color map is logarithmic.

functional, which is expected to be smoother [29]. Additionally, we made attempts to obtain the total energy via a frequency-grid (brute-force) strategy to perform the integral of Eq. (6.5), but we found the grid-spacing parameter to be critical. We accounted for this numerical instability as being due to the non-smooth structure of the spectral function, especially near the chemical potential at k_f, where it has a discontinuity. Nevertheless, in Refs. [97, 98], the authors obtain an accurate frequency integration of the GM formula on the real axis, with results in very good agreement with this work and with the literature already cited.

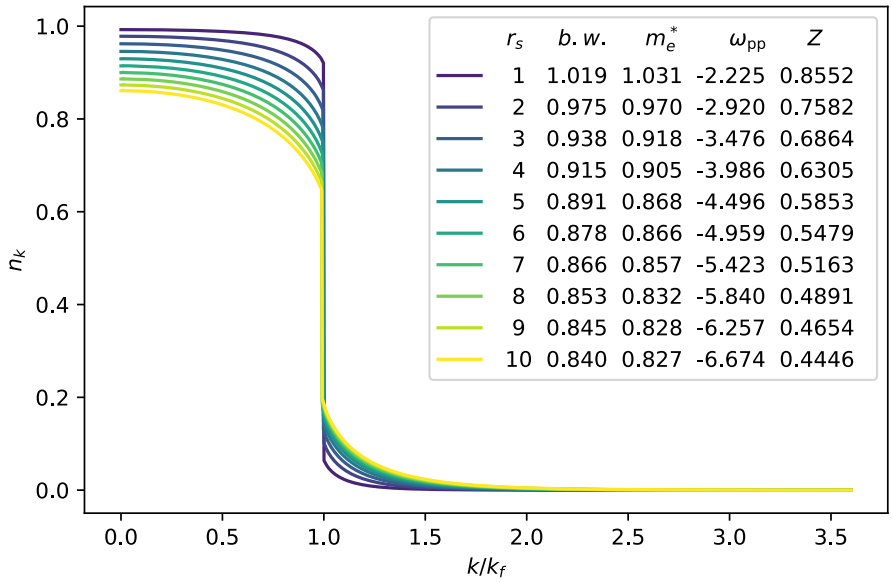

Figure 6.8: Occupation factors in arbitrary units for several densities (r_s from 1 to 10). k_f is the Fermi momentum. In the inset we display the band-width $b.w.$ in units of ϵ_f, the effective mass m_e^* in units of $2m_e$, the plasmaron frequency ω_{pp} in units of ϵ_f, and the renormalization factor in arbitrary units at each density.

HEG: G_0W_0 Correlation Energies $\lvert E_{\mathbf{corr}}\rvert$			
r_s	**This work**	**Ref.** [89]	**Ref.** [76]
1	0.0749 (±0.0015)	0.0722	0.0690
2	0.0545 (±0.0003)	0.0539	0.0530
3	0.0451 (±0.0008)	0.0448	-
4	0.0381 (±0.0003)	0.0382	0.0378
5	0.0333 (±0.0002)	0.0355	0.0331
6	0.0297 (±0.0002)	-	-
7	0.0268 (±0.0002)	-	-
8	0.0245 (±0.0002)	-	-
9	0.0226 (±0.0002)	-	-
10	0.0210 (±0.0002)	-	0.0207

Table 6.1: Correlation energies as function of r_s for the HEG at the G_0W_0 level. Energies are in Hartree units.

6.5 G_0W_0 for a broad range of HEG densities

In this section, we report results for the HEG with r_s ranging from 1 to 10 studied at the G_0W_0 level, following the same approach used for $r_s = 4$. In Fig. 6.6, we show the computed data for the spectral function obtained with the AIM-SOP approach for specific momenta k and

γ	β_1	β_2
−0.1929	1.1182	0.4609
Covariance matrix of the fit		
0.00022	−0.00277	−0.00011
	0.03497	0.00123
		0.00014

Table 6.2: Parameters of the correlation energy fit in Hartree, Eq. (6.7) (same functional form as in [47]), using the data of Table 6.1, and the covariance matrix of the fit. The fitted function is plotted in Fig. 6.9.

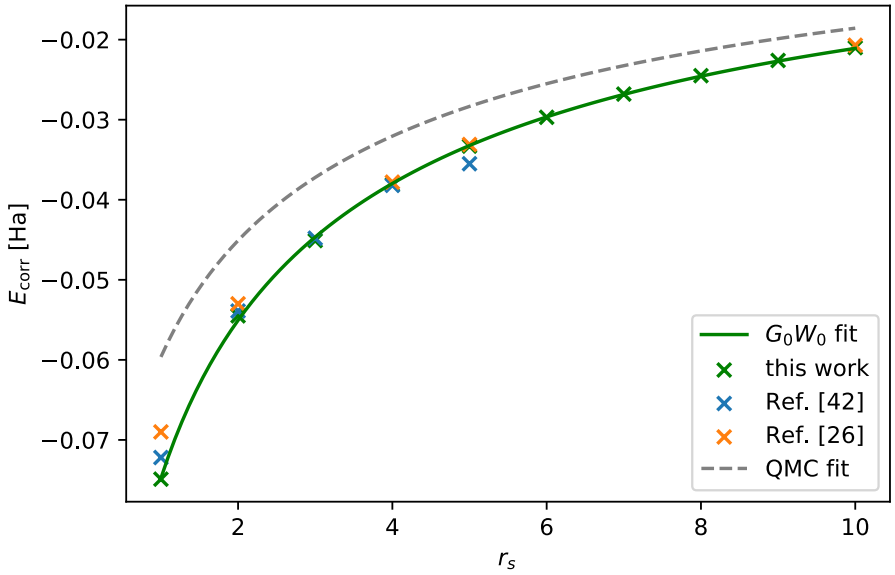

Figure 6.9: Correlation energy in Hartree units for several densities within the G_0W_0 approximation in the HEG. In green we show the results found in this work (see Sec. 6.5) compared with those found in [89] in blue, and with [76] in orange. In green we plot the correlation energy fit of Eq. (6.7) (same functional form as in [47]) on the present (green) data. For reference, in dashed grey we add also the Quantum Monte Carlo data obtained by Ceperley and Alder [46] in the fit made by Perdew and Zunger [47].

densities ($r_s = 2, 4$). For $k = 0$, we take the actual grid point $k = 0.0028 k_f$ since the exact zero point is forbidden in our implementation of Eq. (6.4). At the available momenta $k/k_f = 0.5$, 1.0, and 1.5, and density $r_s = 4$, the spectral function compares qualitatively well with Refs. [56, 88].

In Fig. 6.7, we show the computed data for the spectral function obtained with the AIM-SOP approach. In the chosen units (ϵ_f for the energy and k_f for the momentum), the spectral function for increasing r_s shows an increase in the separation between the quasi-particle band and the satellite occupied and empty bands. Indeed, in these units, r_s controls the interaction

strength – see Eq. (3.24) of Ref. [77] – with the limits of the non-interacting gas obtained for $r_s \to 0$, and the strongly interacting gas corresponding to $r_s \to \infty$. Accordingly, the plasmaron peak of the satellite band at small momenta is weakened for smaller r_s. The same behavior can be observed in the occupation factors of Fig. 6.8 for the different densities. For $r_s \to 0$, the HEG approaches the non-interacting limit, and the occupation number drops from 1 to 0 at k_f. Going towards $r_s = 10$, the jump becomes smaller since the quasi-particle is reduced due to the more evident satellite bands, as can be seen in Fig. 6.7.

The resulting renormalization factors Z are displayed in the last column of the inset of Fig. 6.8 and compare well with the literature [96]. In addition, in the same inset, we show the bandwidth ($b.w.$), effective mass (m_e), and plasmaron frequency (ω_{pp}) at each density, all in units of ϵ_f. We calculate the bandwidth, effective mass, and plasmaron frequency from the spectral function on the (k,ω) grid at each density, using a simple algorithm to find local maxima of the function at fixed momentum. At $k = 0$, we start the local optimization from $-10\,\epsilon_f$ to find the plasmaron peak frequency, ω_{pp}. The quasi-particle band is obtained by collecting optimization results from the different momenta k, each started at μ. Then, a symmetric parabola (for $k < 0.6k_f$) is fitted to estimate the curvature (effective mass, m_e^*) and the y-intercept (bandwidth, $b.w.$).

In Table 6.1, we report the corresponding total energies computed at the different densities, together with some available results in the literature. Moreover, results not explicitly reported in Table 6.1, e.g., from Refs. [97, 98], are overall in very good agreement with those computed in this work. Since calculations in Ref. [76] were done on the imaginary axis, we consider them to be the most accurate for comparison. We refer to Sec. C.3 of the Appendix for the convergence studies of total energies for different densities. We find the largest discrepancy (0.0059 Ha) with respect to the data of Ref. [76] at $r_s = 1$. This can be rationalized by noting, e.g., that n_k is a steeper function, thereby enhancing the numerical issues of the Galitzki-Migdal expression discussed in Sec. 6.3. To deepen the understanding of this numerical discrepancy, aside the convergence study of Fig. C.2 provided in the Appendix, we performed an additional calculation increasing the refinement parameter Δ by 20%, aiming at increasing the accuracy in the integral grids, to target the steeper character of that density. The result, 0.0736 Ha (against 0.0749 Ha of Tab. 6.1), is acceptable, considering the error of 0.0015 Ha reported in the table. Most importantly, we stress that, in contrast to Ref. [76], our procedure provides not only accurate frequency-integrated quantities (e.g., the total energy) but also precise spectral properties on the real axis (key quantities for spectroscopy).

In Fig. 6.9, we plot the correlation energy of Table 6.1 as a function of r_s, including the Perdew-Zunger (PZ) fit of the Quantum Monte Carlo (QMC) Ceperley-Alder data as a reference [47, 46]. We also use the same functional form as PZ to fit our data, providing γ, β_1, and β_2 for the fitting function of the correlation energy in the HEG (in Hartree) in Table 6.2:

$$E_{\text{corr}}(r_s) = \frac{\gamma}{1 + \beta_1\sqrt{r_s} + \beta_2 r_s}, \tag{6.7}$$

together with the covariance matrix of the fit. In Fig. 6.9, we plot the result of the fit as a green line. Given the fit accuracy in Table 6.2, this may be considered an effective parametrization of the G_0W_0 correlation energy of the electron gas.

6.6 Summary of the work on the HEG

In order to provide a working example of the AIM-SOP approach, we apply it to the paradigmatic case of many-body perturbation theory at the G_0W_0 level for the HEG at several densities (r_s from 1 to 10). With AIM-SOP, we are able to obtain accurate spectra and precise frequency-integrated quantities (such as occupation numbers and total energies). At the available densities, we find very good agreement with Refs. [95, 83] for the spectral function. In addition, we provide an in-depth study of the stability and convergence of our results for the total energy, finding quantitative agreement with Ref. [76] for the available r_s, where the calculations were performed on the imaginary axis.

Although in this work, we study a homogeneous system as a test case, the AIM-SOP approach aims to treat realistic non-homogeneous systems in the more general framework of dynamical embedding theories. In Ch. 7 we apply the AIM-SOP approach to a real crystal, thus exploiting the generalization to the operatorial case of the algorithmic-inversion method of Sec. 4.3.

7 AIM-SOP for crystals using dynamical Hubbard

In this chapter, we combine the algorithmic-inversion method for the sum over poles and the dynamical Hubbard functional, both developed in this thesis, to compute accurate spectroscopic and thermodynamic quantities of materials.

We make use of the localized-GW Klein functional, introduced in Ch. 5, which generalizes the DFT+U energy functional of Dudarev et al. [33] to host a dynamical screened potential $U(\omega)$, rather than a static U. The resulting Dyson equation is treated as a nonlinear eigenvalue problem and is solved via an exact mapping to a non-interacting system, exploiting the non-homogeneous version of the algorithmic inversion method on the sum-over-poles for the case of real crystals (see Ch. 4 for details). Within this approach, the single-particle Green's function, along with the Dyson orbitals and excitation energies of the system, are obtained and used to calculate accurate spectral and thermodynamic properties of the material. Owing to the exactness of the solution of the Dyson equation and the SOP representation, the framework does not suffer from problems with avoided crossing in the quasi-particle solution of the Dyson equation [70] or numerical difficulties when integrating the Green's function to obtain thermodynamic quantities [34].

We develop an in-house PYTHON code to implement the exchange-correlation part and the resulting self-energy, $\Phi_{GW_{\mathrm{Loc}}}$ and $\Sigma_{GW_{\mathrm{Loc}}}$ [Eqs. (5.25) and (5.28)].[1] We solve the resulting Dyson equation using the algorithmic-inversion method.

We apply the framework to the paradigmatic case study of $SrVO_3$, finding results in very good agreement with experiments and state-of-the-art methods for the spectrum, bulk modulus, and phonons, at a greatly reduced computational cost compared to established approaches.

The contents of this chapter are based on my article in Ref. [35].

[1] For simplicity of notation, we lose the upper bar for the quantities $\Phi_{GW_{\mathrm{Loc}}}$ and $\Sigma_{GW_{\mathrm{Loc}}}$, even though they refer to having fixed the gauge for the double counting with the prescription of Sec. 5.4, i.e., $c \to \infty$.

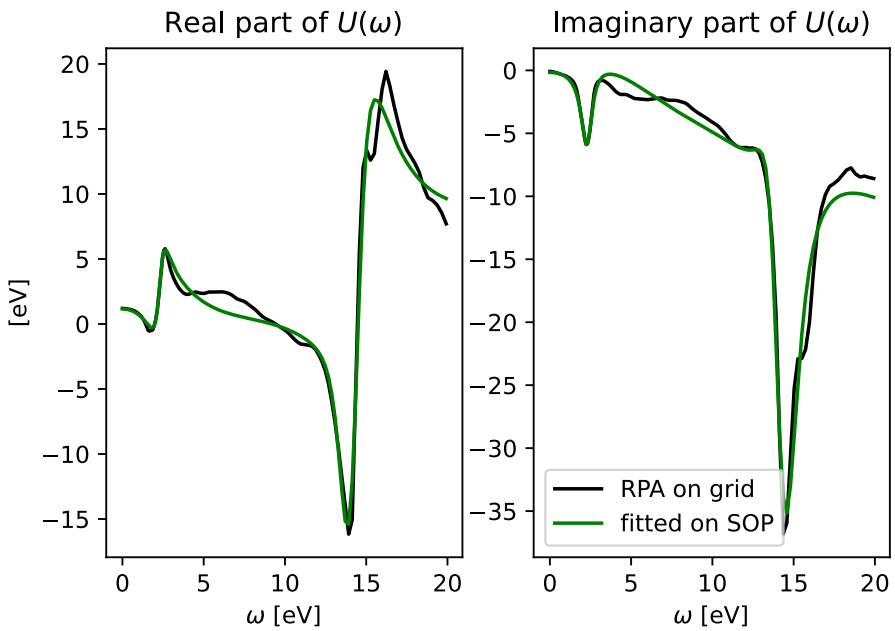

Figure 7.1: Real and imaginary parts of the average screened interaction $U(\omega)$ on the localized t_{2g}+e_g manifold of $SrVO_3$, calculated on a frequency grid using the random-phase approximation (black line). The solid green line shows its SOP representation computed with the algorithm in Sec. 3.3.2. Frequencies are limited to 20 eV with respect to Fig. 3.2.

7.1 Dynamical screening $U(\omega)$ from RPA

In this Section we compare the choice of an RPA screening with another from c-RPA.

Given the localized-GW nature of the functional, we calculate the screening $U(\omega)$ in the RPA approximation. Although appealing, using the c-RPA approximation to calculate the screening $U(\omega)$, as in GW+DMFT [99], is not a perfect fit in the dynamical Hubbard framework. In GW+EDMFT, the screened potential is partitioned into short and long-range, and both are calculated separately. Since the solver already takes into account the excitations inside the localized manifold, the additional screening that one should apply must come from the other electrons, thus implying a c-RPA-type screening that must be calculated for the GW region of the material. In the dynamical Hubbard, we calculate the screening only once, and this has to take into account all the excitations of the material. In particular, the excitations within the manifold are crucial since they depend on the low-energy plasmons that are the origin of interesting physics in correlated metals like $SrVO_3$ (see also Sec. 7.5.1).

In Fig. 7.1, we show the RPA screening for $SrVO_3$ localized on the t_{2g}+e_g manifold (the d-orbitals of the vanadium), $U(\omega)$. The low-energy plasmon at $\simeq 4$ eV comes from excitations within the manifold, while the big peak (in the imaginary part) at $\simeq 10$ eV describes a major (collective) plasmon for the material. As mentioned earlier, the c-RPA, where one has removed the t_{2g}+e_g excitations, would look similar to Fig. 7.1, but without the 4 eV peak in the imaginary

part.

The value of the unscreened potential on the localized orbitals averages to $U_\infty \sim 18$ eV, as can be seen from the asymptotic behavior of the real part of $U(\omega)$ in the right panel of Fig. 3.2.

7.2 Spectral quantities using AIM-SOP for dynamical Hubbard

In this section, we provide a detailed explanation of the calculation of the self-energy $\Sigma_{GW_{\text{Loc}}}$ as a SOP expression, as well as the solution of the Dyson equation to obtain G using the algorithmic-inversion method.

Since the framework is designed for self-consistent calculations, we can assume that we are at any level of the self-consistent cycle with Green's function G_s, and evaluate $\Sigma_{GW_{\text{Loc}}}[G_s]$. Without loss of generality, we can use the SOP form for G_s in the framework. At any level of self-consistency, the SOP representation of G_s is known: starting the cycle with the Kohn and Sham Green's function G_{KS}, we can calculate the SOP form of the self-energy as shown below. [2] We can then solve the resulting Dyson equation using the algorithmic-inversion method to obtain a SOP for G. This cycle can be repeated until self-consistency is achieved.

From Eq. (5.28), the self-energy $\boldsymbol{\Sigma}_{GW_{\text{Loc}}}$ is given by:

$$\boldsymbol{\Sigma}_{GW_{\text{Loc}}}[\boldsymbol{G}_s](\omega) = -\int \frac{d\omega'}{2\pi i} e^{i\omega' 0^+} U(\omega')\boldsymbol{G}_s(\omega+\omega') + \frac{1}{2}U_\infty \boldsymbol{I}, \tag{7.1}$$

where $\boldsymbol{G}_s = P_H G_s P_H$, and P_H are the projectors over the Hubbard manifold, in agreement with Ch. 5. We use the expression for the SOP convolution in Eq. (3.12), where the right propagator is a matrix (on the Hubbard manifold) and the left one is a scalar.

Then, we calculate the full self-energy of the crystal using

$$\Sigma_{GW_{\text{Loc}}} = \sum_{m,m'} |\phi_m\rangle \boldsymbol{\Sigma}^{mm'}_{GW_{\text{Loc}}}(\omega) \langle\phi_{m'}| = \sum_{p,m,m'} \frac{|\phi_m\rangle \boldsymbol{\Gamma}^{mm'}_p \langle\phi_{m'}|}{\omega-\Omega_p} + \frac{U_\infty}{2}P_H = \sum_p \frac{\Gamma_p}{\omega-\Omega_p} + \frac{U_\infty}{2}P_H, \tag{7.2}$$

where $\sum_m \frac{\boldsymbol{\Gamma}_p}{\omega-\Omega_p}$ is the SOP form found for $\boldsymbol{\Sigma}_{GW_{\text{Loc}}} - \frac{U_\infty}{2}\boldsymbol{I}$.

The Dyson equation for the full crystal,

$$G(\omega) = \left[\omega I - \left(h_{\text{KS}} + \frac{U_\infty}{2}P_H + \mu I\right) - \sum_p \frac{\Gamma_p}{\omega-\Omega_p}\right]^{-1}, \tag{7.3}$$

can be solved using the generalization to the operatorial case of the algorithmic-inversion method of Sec. 4.3, where $h_0 = h_{\text{KS}} + \frac{U_\infty}{2}P_H$, I the identity of the Hilbert space of h_0, and μ the chemical potential.

[2] For this step, we also use the SOP representation for $U(\omega)$, discussed in Sec. 7.1.

Since the chemical potential is not known but should obey Eq. (2.17), we first solve the Dyson equation in (7.3) with $\mu = 0$. Then, we calculate μ by solving Eq. (2.17),

$$N = \int_{-\infty}^{\mu} \mathrm{d}\omega \, \mathrm{Tr}\, A(\omega), \tag{7.4}$$

where μ is unknown. Importantly, using the formula for the occupied moments of Eq. (B.5), the above expression can be easily calculated in SOP. [3] Finally, we solve the Dyson equation in (7.3) again with the chemical potential found.

This strategy has proven effective for the one-shot calculations performed here. However, at self-consistency, any strategy would suffice since μ is known from the previous self-consistent step and should not change its value when performing further steps.

7.3 Thermodynamics using AIM-SOP for dynamical Hubbard

In this section, we detail the calculation of $\Phi_{GW_{\mathrm{Loc}}}$. Similar to Sec. 7.2, we assume that we are at any step of the self-consistent cycle and, in particular, we know the SOP of the Green's function G_s of the current step.

To calculate $\Phi_{GW_{\mathrm{Loc}}}[\boldsymbol{G}_s]$ (at any step of the cycle), we rewrite Eq. (5.25) as follows:

$$\Phi_{GW_{\mathrm{Loc}}}[\boldsymbol{G}_s] = \frac{U_\infty}{2}\mathrm{Tr}_\omega \boldsymbol{G}_s - \frac{1}{2}\mathrm{Tr}_\omega \left[\boldsymbol{\Sigma}_{GW_{\mathrm{Loc}}}[\boldsymbol{G}_s]\boldsymbol{G}_s\right], \tag{7.5}$$

where $\mathrm{Tr}_\omega = \int \frac{d\omega'}{2\pi i} e^{i\omega' 0^+}\,\mathrm{Tr}$.[4] The quantities $\boldsymbol{G}_s$ and $\boldsymbol{\Sigma}_{GW_{\mathrm{Loc}}}[\boldsymbol{G}_s]$ are calculated as described in Sec. 7.2.

Since the product of two SOPs is a SOP, we can use the formula for the moment 3.13 (with $m = 0$) to calculate the second term analytically, and thus accurately.

For a generic Green's function, the evaluation of the total energy requires the calculation of the full Klein functional:

$$E_{GW_{\mathrm{Loc}}}[G] = E_H[\rho] + E_{xc}[\rho] + \Phi_{GW_{\mathrm{Loc}}}[\boldsymbol{G}] - \mathrm{Tr}_\omega\left[G_0^{-1}G\right] + \mathrm{Tr}_\omega \mathrm{Log}\, G_0^{-1}G + \mathrm{Tr}_\omega[h_0 G_0]. \tag{7.6}$$

Here, $\rho(\boldsymbol{r}) = \int \frac{d\omega}{2\pi i} e^{i\omega 0^+} G(\omega, \boldsymbol{r}, \boldsymbol{r})$, $G_0 = G_{\mathrm{KS}}$ and $G = G_s$. In particular, the last three terms must also be evaluated. [5]

In this thesis, we limit the approach to one-shot calculations, i.e., a single step in the station-

[3] Note that, differently from the calculation for the HEG in Ch. 6, throughout the whole chapter, we have found it sufficient to consider SOPs built with simple (first-order) Lorentzians.

[4] Note that, unlike in Ch. 2, we change the notation for $\mathfrak{Tr}$ to $\mathrm{Tr}_\omega = \int \frac{d\omega'}{2\pi i} e^{i\omega' 0^+}$, highlighting the dynamical nature of the functional.

[5] Note that, in contrast to Chapter 6, we use the Klein functional to evaluate the total energy instead of the Galitskii-Migdal formula. In general, due to the variational nature of the functional, this should be preferred in one-shot calculations as it ensures quadratic errors.

arization of $E_{GW_{\text{Loc}}}$, using as the starting propagator the self-consistent Kohn-Sham Green's function computed with standard semi-local DFT.

Thus, we need to evaluate the energy functional at $E_{GW_{\text{Loc}}}[G = G_{\text{KS}}]$. At this level, the localized-GW Klein energy functional simplifies to

$$E_{GW_{\text{Loc}}}[G_{\text{KS}}] = E_{\text{DFT}}[\rho] + \Phi_{GW_{\text{Loc}}}[\boldsymbol{G}_{\text{KS}}], \tag{7.7}$$

with $\Phi_{GW_{\text{Loc}}}[\boldsymbol{G}_{\text{KS}}]$ given by Eq. (5.25), which corrects the DFT energy with a generalized dynamical Hubbard energy term.

7.4 One-shot calculations with AIM-SOP for Dynamical Hubbard

In this section, we describe how to perform one-shot calculations using the dynamical Hubbard functional together with the AIM-SOP method. The procedure can be considered a single step in the self-consistent procedure to stationarize the dynamical Hubbard energy functional $E_{GW_{\text{Loc}}}$, defined in Eq. (7.6), and does not rely on the simplifications brought by a non-interacting propagator G_0 to perform the calculations, as in common G_0W_0 implementations. Additionally, the use of the AIM-SOP guarantees accurate calculations of the total energy (see Sec. 7.3 for details) as well as the spectroscopic quantities (Sec. 7.2).

In particular, the strategy adopted is as follows:

- Compute the electronic structure for the material within a chosen approximation of DFT.
- Identify the Hubbard manifold.[6] See Sec. 7.1 for details. For simplicity, here we consider having only one site I.
- Compute the RPA screening on the localized orbitals that span the manifold to obtain $W^{Im',Im}_{Im,Im'}$ and average on the orbitals to obtain $U(\omega)$ of Eq. (5.11). See Sec. 7.1 for details.
- Transform $U(\omega)$ to a SOP form. See Sec. 3.3.2 for details.
- Calculate the self-energy $\Sigma_{GW_{\text{Loc}}}$ on SOP using Eq. (5.28). See Sec. 7.2 for details.
- Use the algorithmic-inversion method for operators (Sec. 4.3) to get the Green's function on SOP and compute the spectrum. See Sec. 7.2 for details.
- Use the functional $\Phi_{GW_{\text{Loc}}}[G]$, Eq. (5.25), to compute the energetics of different atomic configurations to get bulk modulus and vibrational properties of the material. See Sec. 7.3 for details.

[6] As pointed out in Ch. 5 for the dynamical Hubbard functional and Appendix A.5 for DFT+U, to apply the framework the underlying atomic structure has to have partially filled empty d or f orbitals that build up the bands around the Fermi level.

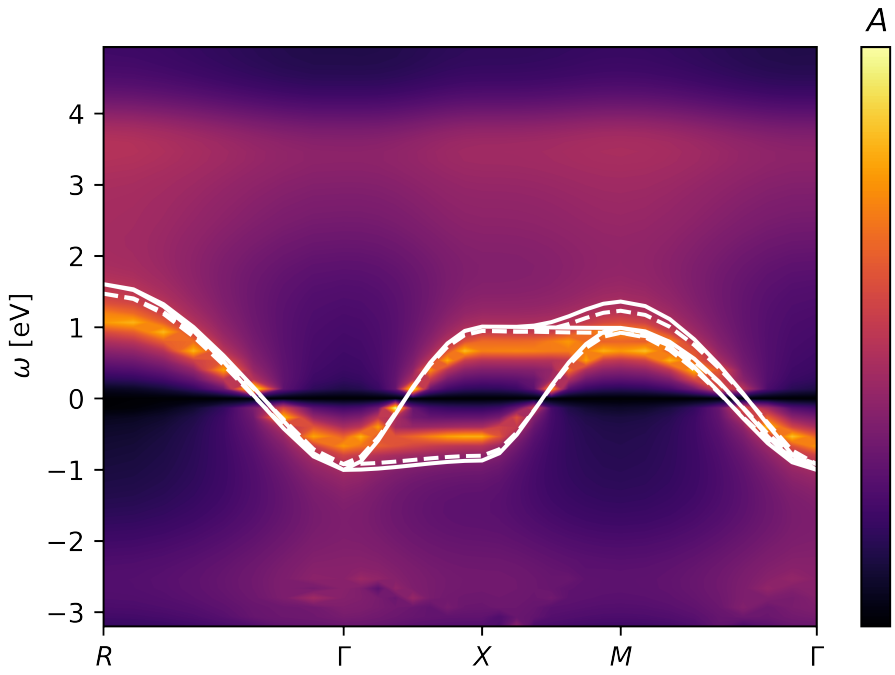

Figure 7.2: Spectral function of $SrVO_3$ from this work (color plot) compared to PBEsol (solid white line) and PBEsol+U (dashed white line). Only the t_{2g} bands are displayed. The chemical potential is shifted to 0 in all the three cases. The thin black band shows the analytic divergence of the spectral function in a metal at the chemical potential. The color map is logarithmic.

7.5 Results on $SrVO_3$

In this section, we apply the formalism described in Sec. 7.4 to the paradigmatic example of $SrVO_3$, where the localized-GW approach has already been shown to give qualitatively good spectral results [100] for the quasi-particle band structure. We not only provide the spectral properties of the material but also integrated quantities such as the total energy and its derivatives (lattice parameter, bulk modulus, phonons), obtained from the functional $E_{GW_{\mathrm{Loc}}}[G]$.

7.5.1 Spectroscopic quantities

In Fig. 7.2, we show the spectral function resulting from the calculation. Contrary to what happens in DFT (PBEsol) and DFT+U (PBEsol+U), which only shift the chemical potential, the spectral function originating from $\Sigma_{GW_{\mathrm{Loc}}}$ shows a reduction of the bandwidth along with a renormalization of the full width of the t_{2g} bands. In Tab. 7.1, we report the bandwidth (BW), the mass enhancement factor (m^*/m_{PBEsol}), and the positions of the lower/upper satellites (LS/US). While PBEsol, PBEsol+U, and GW [100] fail to overestimate the occupied bandwidth and full bandwidth, the present results are in very good agreement with experiments [104, 105] and DMFT [102, 103, 101]. While the quasi-particle band structure calculated with our method

Method	BW	m^*/m_{PBEsol}	LS	US
PBEsol	1.0	1		
PBEsol + U	0.92	1.1		
GW [100]	0.8	1.4	-	-
GW+DMFT [101]	0.5	2	−1.6	2
GW+DMFT [102]	0.6	2	−1.5	2.5
GW+EDMFT [103]			−1.7	2.8
This work	0.6	2	−1.7	2.2
			−3.0	3.9
exp. [104]	0.7	1.8	−1.5	
exp. [105]	0.44	2	−1.5	

Table 7.1: Occupied bandwidth (BW) of the t_{2g} bands, the mass enhancement factor (m^*/m_{PBEsol}), and energy of the lower (LS) and upper satellites (US) from experiments and different theoretical frameworks. Results from the generalized dynamical Hubbard functional introduced in this work are estimated from the spectral function in Fig. 7.2. m^*/m_{PBEsol} is estimated using the ratio of the full bandwidths (LDA and PBEsol coincide). All energies are in eV.

coincides with the one from the localized-GW method of Ref.[100], the satellites are different. This difference may be due to the different choice for the double counting. In Ref.[100], the localization of GW is performed directly from the GW self-energy, which effectively treats the double counting problem in a different way. At variance with other methods, our approach clearly shows that the low-energy satellites shown in Fig. 7.2 are plasmonic since they originate from the 4.7 eV peak of the imaginary part of $U(\omega)$. This can be simply demonstrated by manually taking out the 4.7 eV pole in the SOP for $U(\omega)$ and recomputing the spectral function, which will not show the satellites.

7.5.2 Thermodynamics

In Fig. 7.3, we compare different methods for calculating the equation of state for $SrVO_3$. The legend reports the estimated values for the equilibrium volume V and the bulk modulus B, which are obtained by fitting a Birch-Murnaghan third-order function to the data [107]. The present approach provides a better prediction for the bulk modulus, but it overcorrects the equilibrium lattice parameter, which may be attributed to the lack of self-consistency in the calculations. In Appendix D, we discuss the softening of the bulk modulus in terms of charge rearrangement.

Finally, using the relaxed structures, and taking advantage of the inexpensive computational cost of the present method, we report in Tab. 7.2 the zone-center phonons for $SrVO_3$, using PHONOPY [109, 110]. Since the Hellmann-Feynman theorem does not apply due to the lack of self-consistency, we evaluate the forces for the different displacements of the atoms with finite total energy differences. Analogous to the softening of the bulk modulus, the first two

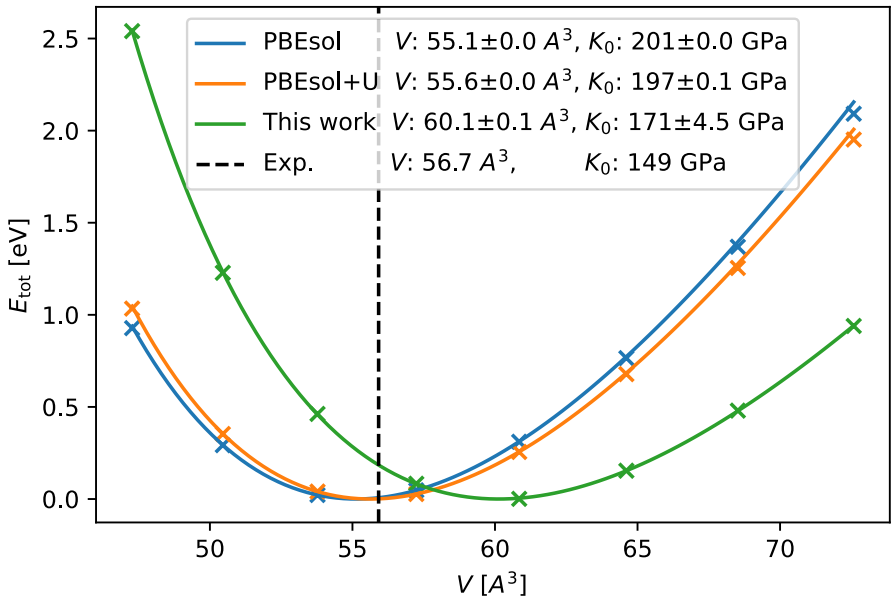

Figure 7.3: The equation of state for $SrVO_3$ is calculated using PBEsol (blue), PBEsol+U (orange), and the present approach (green). The data (crosses) are fitted with the Birch-Murnaghan curve (in solid), and the L values and errors obtained using the fit are displayed in the legend. For reference, the experimental volume is marked in dashed black, and the bulk modulus is reported in the legend. Experimental values are taken from [106].

(THz)	PBEsol	LDA+EDMFT [108]	This work
ω_0	-0.01	0	0.1
ω_1	4.86	4.3	3.9
ω_2	10.3	9.0	9.4
ω_3	11.0	11.2	12.1
ω_4	17.3	18.9	19.4

Table 7.2: Zone center phonons for $SrVO_3$ calculated with different approaches; the last column shows the results obtained using the generalized dynamical Hubbard functional introduced in this work (on top of PBEsol). The data from Ref. [108] have been estimated from the plot.

frequencies are lowered compared to PBEsol calculations. Additionally, similar to state-of-the-art methods such as LDA+EDMFT [108], the remaining optical modes are shifted to higher frequencies. Interestingly, the lack of self-consistency in our method did not significantly alter the results.

7.6 Summary of the work on $SrVO_3$

In this chapter, we provide a Green's function framework for studying the electronic structure in correlated materials using dynamical potentials. We utilize a novel approximation to

the exchange-correlation Φ part of the energy Klein functional, which yields a localized-*GW* self-energy and provides a dynamical generalization of DFT+U, as introduced in Ch. 5. Furthermore, we solve the resulting Dyson equation using an extension of the algorithmic-inversion method on sum-over-poles (AIM-SOP) to realistic materials, as discussed in Ch. 4.

We combine the novel functional with the AIM-SOP method to study the paradigmatic case of $SrVO_3$, obtainig results similar state-of-the-art computational approaches, such as DMFT or EDMFT. However, our approach has a very modest computational cost and allows us to access spectral and thermodynamic properties simultaneously, including total energies and differences.

8 Conclusions and future perspectives

In this thesis, we introduce a novel approach to address the electronic structure of correlated materials. Though not aiming to treat strong correlation, we have designed a framework that is able to deliver spectroscopic and thermodynamic quantities of condensed matter systems accurately and efficiently.

Focusing on a dynamical formalism based on Green's functions, we exploit its flexibility to deliver spectral properties and thermodynamics for a material. First, we provide a suitable representation for dynamical quantities of interacting systems. Termed sum-over-poles representation, we show its effectiveness in performing all the operations of Green's function theories—such as convolutions for spectral quantities and moments for thermodynamics—along with studying the transformation to sum-over-poles forms. See Chapter 3 for details on the work.

Empowered by the framework to deal with dynamical quantities, we address the solution of the Dyson equation. We discuss the Dyson equation as a non-linear eigenvalue problem, showing it is the generalization of the Schrödinger equation to embedded systems, and drawing a link to the mathematical framework. Also, we find a solution for the equation when the dynamical potential is represented as a sum over poles. Within the algorithmic-inversion method, the non-linear problem is mapped into the diagonalization of a Hamiltonian with augmented degrees of freedom, i.e., the poles of the dynamical potential. Similarly to Kohn and Sham DFT, we build a "fictitious" non-interacting system sharing the exact Green's function of the interacting "true" system, when the fictitious degrees of freedom are traced away. The method gives access to the Dyson orbitals as the non-linear eigenvectors, together with the excitation energies of the system as the poles of the Green's function. Furthermore, the sum-over-poles form of the Green's function allows the calculation of accurate spectroscopic and thermodynamic quantities. See Chapter 4 for details on the work.

In order to have an efficient yet accurate energy functional for correlated systems, we combine the precision of DFT+U for ground state properties with the accuracy of GW for the spectrum. Exploiting a localized-GW approach, we generalize the DFT+U functional to host a dynamical

screening $U(\omega)$, thus obtaining the so-called "dynamical Hubbard functional". This yields a localized-GW self-energy and allows for the calculation of the full spectral function of a correlated material while keeping the precision of DFT+U for the charge density, energetics, bulk-modulus, equilibrium lattice constants, phonons, etc. See Chapter 5 for details on the work.

To test the effectiveness of the AIM-SOP for the joint computation of spectral and thermodynamic quantities, we study the homogeneous electron gas at the G_0W_0 level for several densities. We obtain very good agreement with the previous literature when available. See Chapter 6 for details on the work.

To address the electronic structure of correlated real crystals, we combine the AIM-SOP with the dynamical Hubbard functional, and study the paradigmatic test case of $SrVO_3$. We compute the spectral, thermodynamic, and vibrational properties of the correlated metal, showing results similar to state-of-the-art computational approaches, such as DMFT or EDMFT, but with a very modest computational cost, and accessing simultaneously spectral and thermodynamic properties (total energies and differences). See Chapter 7 for details on the work.

In addition, as argued in this thesis, the AIM-SOP method, together with the dynamical Hubbard functional, offers the flexibility to perform self-consistent calculations. The AIM-SOP method is flexible enough to handle interacting propagators at any level of the self-consistent cycle. Moreover, the existence of a Klein functional guarantees variationality, which is a crucial aspect in computing forces or energy derivatives in general via the application of the Hellmann-Feynman theorem.

In general, the computation of material properties with dynamical functionals has yet to demonstrate its predictive power and significant impact on materials science. Along with other applications of the algorithmic-inversion method, allowed by the clear link between the Dyson equation and non-linear eigenvalue problems and solutions, this thesis paves the way for the computation of the spectrum, energy, forces, equilibrium, and vibrational properties of correlated materials with dynamical functionals.

A Details in Green's function theory

A.1 Fourier transform of the Green's function

In this section, it is shown how to perform the Fourier transform of the Green's function from the time to frequency domain. Although lengthy, it is instructive to see how this transformation is performed, giving insights into the reason for a vanishing η, e.g., in Eq. (2.7), and also answering why the Green's function is a complex quantity even in systems that are time-reversal, i.e., when the Hamiltonian is real. Starting from its definition of Eq. (2.5), i.e.,

$$iG(\mathbf{r},t;\mathbf{r}',t') = \langle GS|\hat{\psi}(\mathbf{r},t)\hat{\psi}^{\dagger}(\mathbf{r}',t')|GS\rangle\,\theta(t-t') - \langle GS|\hat{\psi}^{\dagger}(\mathbf{r}',t')\hat{\psi}(\mathbf{r},t)|GS\rangle\,\theta(t'-t), \tag{A.1}$$

the simplest way of obtaining the Fourier transform is by writing the integral representation of the theta function, $\theta(t-t') = -\lim_{\eta\to 0^+}\int \frac{d\omega}{2\pi i}\frac{e^{-i\omega(t-t')}}{\omega+i\eta}$. Then, the equation above reads

$$\begin{aligned} G(\mathbf{r},t;\mathbf{r}',t') = \lim_{\eta\to 0^+}\int \frac{d\omega}{2\pi}\Big(&\langle GS|\hat{\psi}(\mathbf{r})\frac{e^{i(E_{\mathrm{GS}}-\hat{H}-\omega)(t-t')}}{\omega+i\eta}\hat{\psi}^{\dagger}(\mathbf{r}')|GS\rangle \\ &+\langle GS|\hat{\psi}^{\dagger}(\mathbf{r}')\frac{e^{i(\hat{H}-E_{\mathrm{GS}}-\omega)(t-t')}}{\omega-i\eta}\hat{\psi}(\mathbf{r})|GS\rangle\Big), \end{aligned} \tag{A.2}$$

where the $\hat{H}|GS\rangle = E_{\mathrm{GS}}|GS\rangle$ is used for both the first and the second addend, while in the second addend, the change of variable $\omega \to -\omega$ is employed to take into account for the presence of $\theta(t'-t)$, instead of $\theta(t'-t)$. Since the integral has boundaries at infinity, we can make the change of variable $\omega \to E_{GS} - \hat{H} + \omega$ for the first addend and $\omega \to -E_{GS} + \hat{H} + \omega$ for the second and write:

$$\begin{aligned} G(\mathbf{r},t;\mathbf{r}',t') = \lim_{\eta\to 0^+}\int \frac{d\omega}{2\pi}\Big(&\langle GS|\hat{\psi}(\mathbf{r})\frac{e^{i(E_{\mathrm{GS}}-\hat{H}-\omega)(t-t')}}{\omega+i\eta}\hat{\psi}^{\dagger}(\mathbf{r}')|GS\rangle \\ &+\langle GS|\hat{\psi}^{\dagger}(\mathbf{r}')\frac{e^{i(\hat{H}-E_{\mathrm{GS}}-\omega)(t-t')}}{\omega-i\eta}\hat{\psi}(\mathbf{r})|GS\rangle\Big), \end{aligned} \tag{A.3}$$

The Fourier transform reads as in Eq. (2.7),

$$\begin{aligned} G(\mathbf{r},\mathbf{r}',\omega) = \langle GS|\hat{\psi}(\mathbf{r})\frac{1}{\omega-(\hat{H}-E_{GS})+i\eta}\hat{\psi}^{\dagger}(\mathbf{r}')|GS\rangle \\ + \langle GS|\hat{\psi}^{\dagger}(\mathbf{r}')\frac{1}{\omega-(E_{GS}-\hat{H})-i\eta}\hat{\psi}(\mathbf{r})|GS\rangle\,. \end{aligned} \tag{A.4}$$

A.2 Galitskii-Migdal formula

The energy functionals presented in Chapter 2 are not the only functionals of the Green's function that can give the total energy. The Galitskii-Migdal formula [111] gives the exact total energy of a system if the Green's function is exact. To derive it, we add the term $h_0(\mathbf{r})\hat{\psi}(\mathbf{r},t)$ to Eq. (2.45). Recalling the second quantized form of the Hamiltonian in Eq. (2.38) and Eq. (2.45),

$$\int \mathrm{d}\mathbf{r}\left[\hat{\psi}^{\dagger}(\mathbf{r},t)i\partial_t\hat{\psi}(\mathbf{r},t)+\hat{\psi}^{\dagger}(\mathbf{r},t)h_0(\mathbf{r})\hat{\psi}(\mathbf{r},t)\right] = 2\,\hat{H}, \tag{A.5}$$

bracketing on the ground state gives the Galitskii-Migdal formula for the Green's function

$$E = \frac{1}{2}\int \mathrm{d}\mathbf{r}\lim_{\substack{t'\to t^+\\ \mathbf{r}'\to\mathbf{r}}}[\partial_t + ih_0(\mathbf{r})]\,G(\mathbf{r},t;\mathbf{r}',t') = \frac{1}{2}\int \mathrm{d}\mathbf{r}\lim_{\mathbf{r}'\to\mathbf{r}}\int \mathrm{d}\omega\,\frac{e^{i\omega 0^+}}{2\pi i}\,(\omega+h_0(\mathbf{r}))\,G(\mathbf{r},\mathbf{r}',\omega), \tag{A.6}$$

which differs from the interaction energy, Eq. (2.46), only by the sign of the second term. This functional is not variational, i.e., the derivative of the functional does not need to be zero at the exact Green's function. Thus, it *cannot* be used to find the Green's function of a system as a variational condition.

A.3 From the Luttinger Ward to the Klein functional

The stationarity condition, i.e., the Dyson equation, can be used to rewrite the Luttinger Ward functional. This gives rise to other possible functionals of the Green's function, such as the Klein functional. However, care must be taken to not change the derivative to keep the functional variational. For example, using the Dyson equation $G^{-1} = G_0^{-1} - \Sigma$, the last term in the Luttinger Ward functional of Eq. (2.57) can be rewritten as:

$$E_0 + \mathfrak{Tr}\ln(1 - G_0\Sigma[G]) = E_0 + \mathfrak{Tr}\,\ln G_0 G^{-1}. \tag{A.7}$$

For the sake of the argument of Sec. 2.3 one may also point out

$$E_0 + \mathfrak{Tr}\,\ln G_0 G^{-1} = E_0 + \mathfrak{Tr}\,\ln G_0 - \mathfrak{Tr}\,\ln G = -\mathfrak{Tr}\ln G. \tag{A.8}$$

In the last equality, we have used $E_0 = \mathfrak{Tr}\,[h_0 G_0] = -\mathfrak{Tr}\ln G_0$.[1] This follows from $\mathfrak{Tr}\left[G_0^{-1}G_0\right] = 0$, since the trace in frequency, $\int \mathrm{d}\omega\, \frac{e^{i\omega 0^+}}{2\pi i}$, counts the occupied poles of the function, and the Galitskii-Migdal formula. Note that the two lines in the last equation are for demonstration purposes or should be regularized before writing. Indeed, in a continuous system, one can show that $\mathfrak{Tr}\ln G$ diverges, while $E_0 + \mathfrak{Tr}\,\ln G_0 G^{-1}$ does not.

This said, the functional

$$\Phi[G] - \mathfrak{Tr}\,[\Sigma[G]G] + E_0 + \mathfrak{Tr}\ln(1 - G_0\Sigma[G]). \tag{A.9}$$

is not variational anymore.

Rewriting also the second addend by using the Dyson equation restores the variationality,

$$E_{\mathrm{K}}[G] = \Phi[G] - \mathfrak{Tr}\left[G_0^{-1}G\right] + E_0 + \mathfrak{Tr}\ln(1 - G_0\Sigma[G]), \tag{A.10}$$

as can be seen by taking the variation of this functional. The latter is termed the Klein functional and differs from the Luttinger Ward only outside of the stationary points, i.e., where the Dyson equation for the Green's function does not hold.

A.4 GW

In this section, we introduce the GW approximation to the Φ functional and the respective self-energy. In fact, there are mainly two ways of introducing the GW approximation. Historically, the first way is to write Hedin's equations and neglect vertex corrections [112]. The GW self-energy can also be derived from an approximation to the Φ functional. Here, we take the latter approach.

Following Ref. [29] the Φ_{GW} functional reads:

$$\Phi_{GW} = \frac{1}{2}\mathfrak{Tr}\bar{G}v\bar{G} - \frac{1}{2}\mathfrak{Tr}Gv G + \frac{1}{2}\left(\mathfrak{Tr}\ln[I - vP_0] + vP_0\right), \tag{A.11}$$

where v is the Coulomb potential, $\bar{G}$ consider only the diagonal of the matrix G, and the matrices products, e.g., GG conserve energy and momentum. [2] The first term is the Hartree term of the energy as it can be proven by direct integration in frequency

$$E_H = \frac{1}{2}\mathfrak{Tr}\bar{G}v\bar{G} = \frac{1}{2}\int \mathrm{d}\mathbf{r}\,\mathrm{d}\mathbf{r}'\, n(\mathbf{r})\, v(\mathbf{r}-\mathbf{r}')\, n(\mathbf{r}'). \tag{A.12}$$

[1] Please note that this equality is valid only if G_0 is of a *non-interacting closed* system.

[2] The momentum-energy conservation is clearer from the diagrammatic expressions of the different terms for Φ. Here, since only the Φ in terms of matrices and traces are given, one should consider that those are simple (not matrix) products in time-space space, and that G depends only on time differences.

The second addend is the Fock exchange energy

$$E_x = -\frac{1}{2}\mathfrak{Tr}\, G v G = -\frac{1}{2}\int \mathrm{d}\mathbf{r}\,\mathrm{d}\mathbf{r}'\, n(\mathbf{r},\mathbf{r}')\, v(\mathbf{r}-\mathbf{r}')\, n(\mathbf{r}',\mathbf{r}). \tag{A.13}$$

P_0 is the polarizability in the random-phase approximation [113]

$$P_0(\omega) = \int \mathrm{d}\omega'\, \frac{e^{i\omega 0^+}}{2\pi i} G(\omega+\omega')\, G(\omega'), \tag{A.14}$$

where the space indexes are omitted for simplicity. The derivative over $G(\omega)$ of the term $\frac{1}{2}\mathfrak{Tr}\ln[I - vP_0]$ yelds

$$\frac{1}{2}\frac{\delta\left(\mathfrak{Tr}\ln[I-vP_0]\right)}{\delta G(\omega)} = \frac{i}{2\pi}\left[I - vP_0\right]^{-1} G v = \frac{i}{2\pi} GW, \tag{A.15}$$

where W is the screened potential in the RPA approximation

$$W(\mathbf{r},\mathbf{r}',\omega) = v(\mathbf{r}-\mathbf{r}') + v(\mathbf{r}-\mathbf{r}')\, P_0(\mathbf{r},\mathbf{r}',\omega)\, W(\mathbf{r},\mathbf{r}',\omega). \tag{A.16}$$

In full indexes, the overall derivative of Φ_{GW} reads

$$2\pi i \frac{\delta\phi_{GW}}{\delta G(\mathbf{r},\mathbf{r}',\omega)} = \delta(\mathbf{r}-\mathbf{r}')\int \mathrm{d}\mathbf{r}_1\, n(\mathbf{r}_1)\, v(\mathbf{r}-\mathbf{r}_1) - \int \mathrm{d}\omega'\, \frac{e^{i\omega' 0^+}}{2\pi i} G(\mathbf{r},\mathbf{r}',\omega+\omega')\, W(\mathbf{r},\mathbf{r}'+\omega'), \tag{A.17}$$

which is the Hartree potential (first term) and the GW self-energy $\Sigma_{GW}(\omega)$ (second term).

It is not clear whether the success of the GW approximation is due to its derivability from a Φ functional or because it is a very good starting point for solving Hedin's equations. There is a physical advantage to both.

The GW self-energy features a Fock-like term, with a screened interaction instead of a bare one. This is particularly important for solids, especially metals, where the presence of electrons near the Fermi surface increases screening.

Looking instead to the functional in Eq. (A.11), one can see that the term $\mathfrak{Tr}\, vP_0$ takes into account long-range polarization effects and thus van der Waals interactions.

Since GW is variational, it is possible to solve the underlying Dyson equation self-consistently to find the stationary point. Multiple authors have shown, first for the HEG [88], and then for molecules, that self-consistency improves the results on the total energy, while worsening the spectrum of the material. One could infer that the improvement in the total energy is due to the validity of particle conservation at self-consistency (see Sec. 2.2 for details) and the other conservation rules implied by a functional at its stationary point. To account for the loss in the accuracy of the spectral properties, the fact that P_0 is not a good approximation for the polarizability of the system at self-consistency, since it no longer obeys the f-sum rule [88], can play a role.

This is also confirmed by the partial self-consistent GW_0 calculations on the HEG in Ref. [56], where self-consistency is carried out only on G, and spectral results do not seem to worsen. Importantly, also for the GW_0 approach, there is a generating functional, i.e.,

$$\Phi_{GW_0} = \frac{1}{2}\mathfrak{Tr}\bar{G}v\bar{G} - \frac{1}{2}\mathfrak{Tr}Gv G + \frac{1}{2}\mathfrak{Tr}GGW, \tag{A.18}$$

with a given screened potential $W_0(\omega)$. Also, e.g., in Ref. [81], it is shown that Φ_{GW_0} is particle-conserving and holds the continuity equation.

A.5 DFT+U

In this section, we introduce a correction to semi-local DFT that can be applied to materials having partially occupied bands with strong d or f atomic character. Interestingly, the fundamental idea is similar to dynamical-mean field theory. Let's suppose we adopt a quasi-particle picture and know that there are some bands that have a predominant atomic character. In general, these bands are not really dispersive, and thus the electrons are localized in the orbitals contributing to them.[3] The idea of DFT+U is to use this knowledge to improve approximate local or semi-local DFT functionals.

In Mott insulators, the localization of electrons is strong enough to turn a crystal with an odd number of electrons in the unit cell—which, according to band theory, has to be a metal—into an insulator [115]. The Hubbard model is a simple lattice model that captures the Mott transition [116, 117, 118, 119, 120, 121]. The Hamiltonian for this model, the so-called Hubbard Hamiltonian, reads:

$$H_U = t\sum_{i,\sigma}\left(c_{i,\sigma}c^{\dagger}_{i+1,\sigma} + c.c.\right) + U\sum_{i} n_{i,\uparrow}n_{i,\downarrow}, \tag{A.19}$$

where the sum runs over all the sites of the lattice, and σ is the spin index. The first term in H_U is a first-neighbor tight-binding term that represents the hopping between the sites (with spin conservation in the hopping). The second term is a 4-point term—since $n_{i,\sigma} = c_{i,\sigma}c^{\dagger}_{i,\sigma}$—that mimics the on-site Coulomb repulsion (with different spins, since we suppose i,σ is a complete label for the fermions). The transition between the Mott insulator and a normal metal or an insulator is controlled by the ratio between the on-site U term and the band term t. With $U \gg t$, electrons are localized on the sites, and the material is in the Mott regime. Vice versa, with $U \ll t$, the crystal is in a "standard" weakly interacting state, and electrons are delocalized, as in band theory.

The idea of DFT+U is to consider the band term given by a semi-local DFT functional and add a "$+U$" term. This is to correct a failure of semi-local DFT that tends to over-delocalize electrons [13]. This deficiency of semi-local functionals has consequences in ground state predictions such as lattice parameters or metallic ground states. Here, we note that these

[3] Note that the localization of the electrons into such atomic bands can be a signature of correlation. Indeed, one can infer that the wave function describing those electrons is composed of a linear combination of determinants that compete in energy. This is a signature of "static" correlation that local or semi-local DFT fails to predict [114].

are just failures of approximate DFT, in this case semi-local. The exact exchange-correlation functional of the density or the spin-density (for spin-DFT) would give accurate results for all ground-state properties. The fact that in KS-DFT, by looking at the KS spectrum, the bands would be metallic should not mislead since the KS system is fictitious and does not need to reproduce the spectroscopic properties of the system [11].

Historically, to introduce the DFT+U, a parallelism is made between the Hubbard Hamiltonian and the "+U" correction to the energy, given by:

$$\sum_I \frac{U_I}{2} \sum_{m,\sigma \neq m',\sigma'} \mathbf{n}_m^{I\sigma} \mathbf{n}_{m'}^{I\sigma'}, \tag{A.20}$$

where $\mathbf{n}^{I\sigma}$ is the spin-resolved density matrix projected onto a "Hubbard" site, i.e., $\mathbf{n}^{I\sigma} = P_I n_\sigma P_I$. The "Hubbard site" defines the Hubbard space, where it is assumed that "strong interactions" play a role. Moreover, since we are using the +U term to correct an approximate DFT functional, we should take into account that the interactions inside the Hubbard manifold are now counted twice. We can approximate the double-counting term by $\frac{U_I}{2} n^I (1 - n^I)$, with $n^I = \sum_\sigma \mathrm{Tr}\, \mathbf{n}^{I\sigma}$, which is a mean-field approximation to the correction $n_\uparrow n_\downarrow$ that we gave before, respecting the rule that on average $n_\uparrow + n_\downarrow = 1$ for a single (spinless) orbital.

In this section, we take a different approach to explaining the DFT+U functional by showing its link to the issues of "local" piece-wise linearity and delocalization, which are problematic for semi-local DFT. Neglecting spin for simplicity, the functional of the density matrix given by

$$E_U = \sum_I \frac{U_I}{2} \left[\left(n^I\right)^2 - \mathrm{Tr}\left[\left(\mathbf{n}^I\right)^2 \right] \right] + E_{\mathrm{dc}}[n^I] \tag{A.21}$$

is composed of a term that resembles the variance with respect to a mean n^I of the variable $\mathbf{n}^I$, with Tr being the mean estimator operator, and a double counting term. Thus, E_U measures the "localization" of the Hubbard manifold. The more uniformly the manifold is occupied around its mean (n_I), the lower the variance, and so is the +U correction. Conversely, the more the Hubbard manifold tends to have different values for the single orbital occupation, the greater the correction.

A good idea for the double counting is to design a function that is peaked around one half. Since we already know that the semi-local DFT functional tries to put on average one half in all the orbitals, the double counting has to be maximum for those occupation values. A function that respects all the requirements is

$$E_{\mathrm{dc}}[n^I] = \frac{U_I}{2} n^I (1 - n^I). \tag{A.22}$$

Putting all together, the Dudarev functional of DFT+U is

$$E_{\text{PBE+U}}[\rho, \mathbf{n}^I] = E_{\text{PBE}}[\rho] + \sum_I \frac{U_I}{2} \text{Tr}\left[\mathbf{n}(\mathbf{1} - \mathbf{n})\right], \tag{A.23}$$

where $\mathbf{1}$ is the identity in the Hubbard manifold, and we have specialized to a semi-local functional for notation purposes, as described in [33].

Curing the over-delocalization of PBE gives the functional form in Eq. (A.23), composed of a negative quadratic part and a positive linear one. Since semi-local DFT functionals are known to be convex [122] with respect to particle addition/removal, instead of being piece-wise linear [123], the fact that we have a negative concave quadratic term and a linear term means that—with the correct U_I—one can restore a "local" piece-wise linearity for the addition/removal of electrons from the Hubbard manifold to the rest of the solid. In fact, since we are adding an electron from the manifold to the solid, or vice versa, it is better to speak about charge transfer, i.e., moving a charge within the solid from one place to another. Since one requires the DFT functional to exhibit the correct convex behavior, and U multiplies a quadratic $\boldsymbol{n}^2$ term minus a linear one, it is natural to interpret U as the curvature of the functional with respect to populating/depopulating the Hubbard manifold Therefore, we set $U = \chi^{-1} - \chi_0^{-1}$, where χ is the response function of the system for such charge transfer, and χ_0 is the response of the KS system for the same process. We consider a single site here for simplicity.[4] This has been the work of Cococcioni and De Gironcoli in Ref. [124]. A ready-to-read review by Cococcioni on all these aspects can be found in Ref. [114], and references therein.

As a final note, the double counting used to obtain Eq. (A.23), which allows us to interpret U as the charge-transfer linear response, is based on the fully localized limit and is given by Eq. (A.22). However, this is not the only possible choice for the double counting of DFT+U. Another option is the around-mean-field approach given by

$$E_{\text{dc}}^{\text{AMF}}[n^I] = \frac{U_I}{2} n^I \left(\langle n^I \rangle - n^I\right), \tag{A.24}$$

where we have replaced the constant 1 with the average occupation of the manifold $\langle n^I \rangle$.[5] This will be useful when we discuss our dynamical generalization to the Hubbard functional in Ch. 5.

[4] The need to subtract from the full response χ the response of the independent KS electrons χ_0 is because U has to cure the spurious (concave) dependence on the number of particles (in the manifold) due to interactions, and not the response of independent electrons to a perturbation of the charge.

[5] Note that this is true for the energy. For the potential, we need to replace $\frac{1}{2}$ with $\langle n^I \rangle$ because of the derivative.

B Details in dynamical operators

B.1 Sum-over-poles representation of an n-th order Lorentzian

In this appendix, we obtain the SOP representation of a Green's function that features a spectral function described by a single n-th order Lorentzian. Recalling Sec. 3.2, we use the discrete time-ordered Hilbert transform [Eq. (3.5)] of a (not normalized) n-th order Lorentzian centered at ϵ_j:

$$\int \frac{d\omega'}{\pi} \frac{1}{\omega - \omega' - i0^+ \operatorname{sgn}(\mu - \epsilon_j)} \frac{|\delta_j|^{2n-1}}{(\omega' - \epsilon_j)^{2n} + (\delta_j)^{2n}}. \tag{B.1}$$

This expression induces a SOP representation for the Green's function, as described in Sec. 3.2.

We can compute Eq. (B.1) explicitly using the residue theorem. By closing the contour in the lower/upper plane for $\epsilon_j \lessgtr \mu$, the poles of the integrand,

$$\zeta_{j,m} = \epsilon_j + e^{i\frac{\pi}{2n}(1+2m)}\delta_j, \tag{B.2}$$

come only from the spectral function A. Using L'Hôpital's rule, we can reduce the residues of the integrand to:

$$R_{j,m} = -\frac{1}{2n\pi} \frac{e^{i\frac{\pi}{2n}(1+2m)}}{\omega - \zeta_{j,m} - i0^+ \operatorname{sgn}(\epsilon_j)}. \tag{B.3}$$

Thus, taking the limit for $\mathscr{C}$ on the real axis, the poles and residues of the SOP for G are those in Eqs. (3.10) and (3.9). We can compute the normalization of the n-th order Lorentzian by summing α_m of Eq. (3.9) and using the geometric sum:

$$N_n = -\frac{i}{n} \sum_{m=0}^{n-1} e^{i\frac{\pi}{2n}(1+2m)} = \frac{1}{n \sin\left(\frac{\pi}{2n}\right)}. \tag{B.4}$$

B.2 Moments of a propagator and occupied moments of its spectral function

In this Appendix, we discuss the equality between the (regularized) moments of a propagator, defined in Eq. (3.13), and the occupied moments of its spectral function. For simplicity of notation, we restrict to the case of a spectral function A composed of a single n-th Lorentzian $\mathscr{L}^n_{\delta_j}$, as defined in Eq. (3.7), and focus on the case $m \leq 2(n-1)$:

$$\begin{aligned} E_m[G] &= \oint_\Gamma \frac{dz}{2\pi i} \int d\omega \, \frac{e^{iz0^+} z^m \mathscr{L}_{\delta_j}(\omega - \epsilon_j)}{z - \omega - i0^+ \operatorname{sgn}(\mu - \epsilon_j)} \\ &= \int d\omega \, \mathscr{L}_{\delta_j}(\omega - \epsilon_j) \times \\ &\qquad \oint_\Gamma \frac{dz}{2\pi i} \frac{e^{iz0^+} z^m}{z - \omega - i0^+ \operatorname{sgn}(\mu - \epsilon_j)} \\ &= \int_{-\infty}^{+\infty} d\omega \, \omega^m \mathscr{L}_{\delta_j}(\omega - \epsilon_j) \theta(\mu - \epsilon_j), \end{aligned} \tag{B.5}$$

where Γ is defined as in Eq. (3.13) and the integral on the last line is well-defined since $\mathscr{L}_{\delta_j} \sim \frac{1}{\omega^{2n}}$ for large frequencies, and $m \leq 2(n-1)$. Also, the integrals extend over the whole real axis because we are dealing with a single basis element (a single n-th Lorentzian), taken here as retarded. Time-ordering is accounted for by the $\theta(\mu - \epsilon_j)$ factors. In fact, in the continuum limit of a complete basis representation (defined in Sec. 3.2), the last line of Eq. (B.5) becomes $\int_{-\infty}^{\mu} d\omega \, \omega^m A(\omega)$.

For higher-order moments, $m > 2(n-1)$, the above equalities are not valid, with the rhs of Eq. (3.13) becoming complex, and the last line of Eq. (B.5) diverging. While the divergence of the rhs of Eq. (B.5) can be understood by looking at the decay of the overall integral, the imaginary contribution to the moment of Eq. (3.13) may be seen explicitly by inserting poles and amplitudes of $\mathscr{L}^n_{\delta_j}$ and using the binomial expansion. Thus, Eq. (3.13) can be rewritten as

$$E_m[G] = \frac{1 - e^{\frac{i\pi}{2}}}{2} \sum_{k=0}^{m} \binom{m}{k} \epsilon_j^{m-k} \delta_j^k e^{\frac{i\pi k}{2n}} \sum_{p=0}^{n-1} e^{\frac{i\pi(k+1)}{n} p}, \tag{B.6}$$

which is in general complex, and reduces the real number

$$E_m[G] = \frac{1}{nN_n} \sum_{\substack{k=0 \\ \text{even}}}^{m} \binom{m}{k} \epsilon_j^{m-k} \delta_j^k \left[\sin \frac{\pi(k+1)}{2n}\right]^{-1}, \tag{B.7}$$

if $m \leq 2(n-1)$. In the case of $m > 2(n-1)$, we can still use Eq. (3.13) to calculate the occupied moment, and improve on the result by lowering the broadening of the Lorentzian(s), which in turn reduces the spurious imaginary part of the targeted moment.

C Details in AIM-SOP for homogeneous systems in GW

C.1 Time-ordered G_0G_0 polarizability at finite (Lorentzian) broadening

In this Appendix we calculate the time-ordered G_0G_0 polarizability at finite (Lorentzian) broadening δ. Note that usually, e.g., in Ref. [77], the calculation is carried out at $\delta = 0$. The time-ordered G_0G_0 polarizability can be calculated from [77]:

$$\begin{aligned} P^0(q,\omega) = \frac{2}{(2\pi)^3}\int d^3k\, & \frac{\theta(|\mathbf{q}+\mathbf{k}|-k_f)\theta(k_f-k)}{\omega+\epsilon_k-\epsilon_{|\mathbf{k}+\mathbf{q}|}+i\eta} \\ & -\frac{\theta(k_f-|\mathbf{q}+\mathbf{k}|)\theta(k-k_f)}{\omega+\epsilon_k-\epsilon_{|\mathbf{k}+\mathbf{q}|}-i\eta}, \end{aligned} \tag{C.1}$$

where the second addend can be obtained by changing the sign of the frequency in the first.

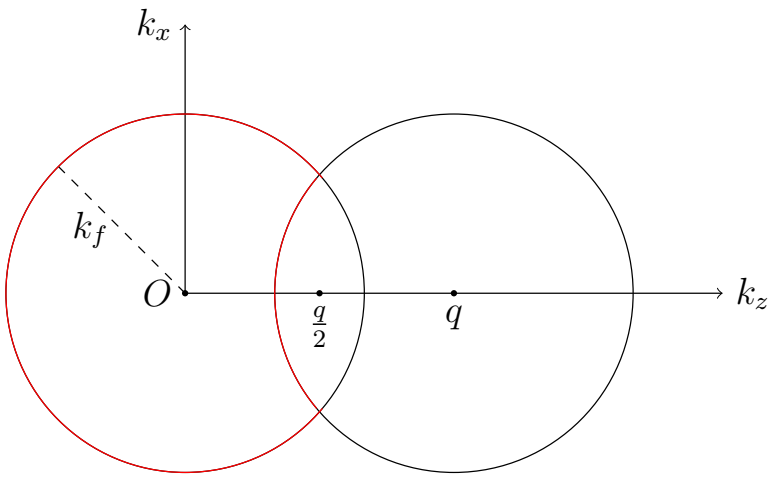

Figure C.1: 2D-projection of Ω onto the (k_z, k_y) plane. Ω can be seen as the volume of revolution around the k_z axis of the region delimited by the red line.

Measuring the momenta in units of k_f, the energies in units of ϵ_f, and exploiting the free-particle energy dispersion $\epsilon_k = k^2$, it is possible to rewrite the first addend of Eq. (C.1) as

$$I(q,z) = \frac{1}{2q}\int_\Omega d^3k\,\frac{1}{z+k_z}, \tag{C.2}$$

assuming a the reference system with q along the k_z axis and $z = \frac{\omega}{2q} - \frac{q}{2} + i\frac{\eta}{q}$. The integral domain Ω can be seen as the volume of revolution around the k_z axis of the region delimited by the red line in Fig. C.1. We calculate I by integrating over the whole sphere (Ω_{sph}) of radius k_f and then subtracting the remainder part (Ω_{R}). The result on the whole sphere is

$$I_{\Omega_{\text{sph}}}(q,z) = \frac{2\pi}{q}\left(\frac{z}{2} + \frac{1-z^2}{4}\ln\frac{z+1}{z-1}\right), \tag{C.3}$$

and for the remainder part it reads:

$$I_{\Omega_{int}}(q,z) = \frac{\pi}{2q}\left[(1-\frac{q}{2})(2z+q) - ((z+q)^2-1)\log\left(\frac{z+q/2}{z+q-1}\right) - (z^2-1)\log\left(\frac{z+1}{z+q/2}\right)\right]. \tag{C.4}$$

Finally, the expression for the G_0G_0 polarizability is

$$P^0(q,\omega) = \frac{4k_f m_e}{(2\pi)^3\hbar}\left[I\left(\frac{\omega/\epsilon_f}{2q/k_f} - \frac{q/k_f}{2} + i\frac{\eta/\epsilon_f}{q/k_f}\right) + I\left(\frac{-\omega/\epsilon_f}{2q/k_f} - \frac{q/k_f}{2} + i\frac{\eta/\epsilon_f}{q/k_f}\right)\right], \tag{C.5}$$

where $I = I_{\Omega_{\text{sph}}} - I_{\Omega_{\text{R}}}$. In addition, the analytic continuation of this function can be done substituting the real ω with a complex one.

C.2 Exploiting parity of the RPA-polarizability integral

In this appendix, we show how it is possible to exploit the parity of the polarizability $P(q,\omega)$ at fixed momentum $\mathbf{q}$. As explained in Sec. 3.4, the SOP approach allows us to compute analytically the convolution of Eq. (6.1). Using Eq. (3.12) in Eq. (6.1), the polarizability may be rewritten as:

$$P(q,\omega) = 2\int\frac{d\mathbf{k}}{(2\pi)^3}\times \left[\sum_{\substack{i,j\\ \text{Im}\{z_i(|\mathbf{k}+\mathbf{q}|)\}<0\\ \text{Im}\{z_j(k)\}>0}}\frac{A_i(|\mathbf{k}+\mathbf{q}|)A_j(k)}{\omega+z_j(k)-z_i(|\mathbf{k}+\mathbf{q}|)} - \sum_{\substack{i,j\\ \text{Im}\{z_i(|\mathbf{k}+\mathbf{q}|)\}>0\\ \text{Im}\{z_j(k)\}<0}}\frac{A_i(|\mathbf{k}+\mathbf{q}|)A_j(k)}{\omega+z_j(k)-z_i(|\mathbf{k}+\mathbf{q}|)}\right], \tag{C.6}$$

where we have not yet restricted to the G_0 case in which only one pole is present. Defining $I(|\mathbf{k}+\mathbf{q}|_{\text{unocc}}, k_{\text{occ}}, \omega)$ as the first term in the right-hand side (where k_{occ} labels the occupied states with momentum k, while $|\mathbf{k}+\mathbf{q}|_{\text{unocc}}$ refers to empty states), and setting $\mathbf{k}+\mathbf{q} \to -\mathbf{k}$ in

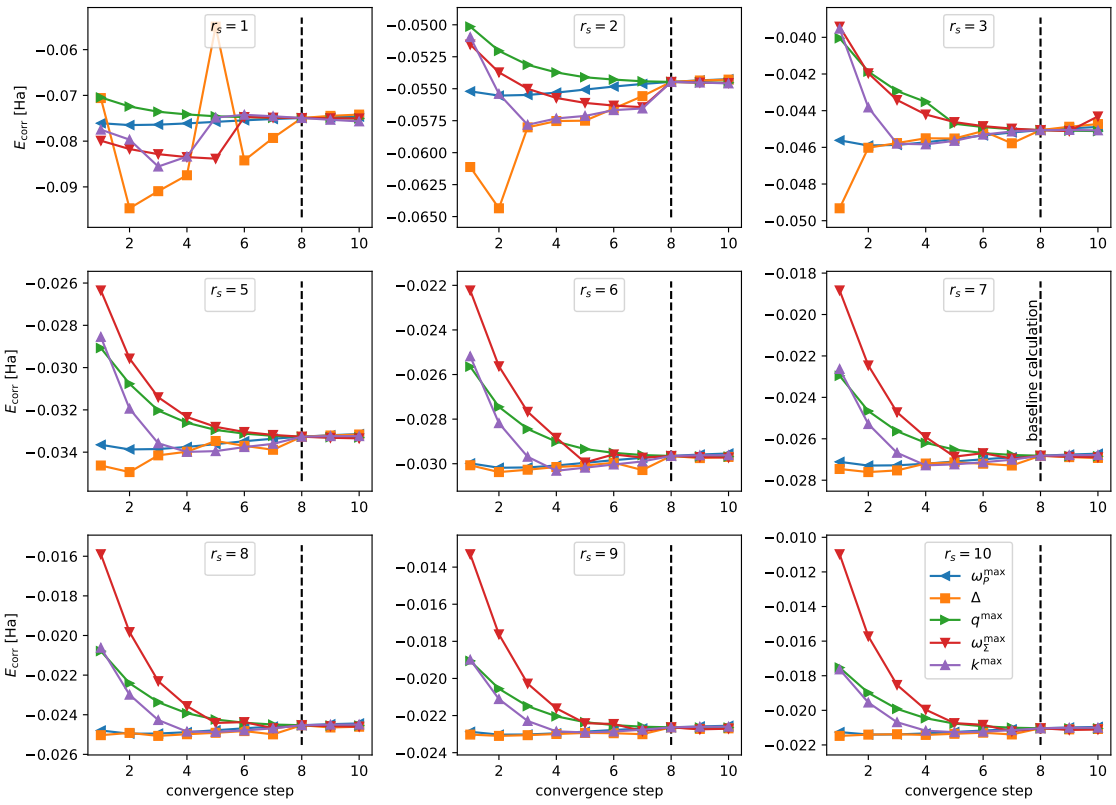

Figure C.2: Convergence studies for the total energy at $r_s = \{1,2,3,5,6,7,8,9,10\}$ following the protocol detailed in Sec. C.4.

the second term,

$$P(q,\omega) = 2\int \frac{d\mathbf{k}}{(2\pi)^3}\left[I(|\mathbf{k}+\mathbf{q}|_{\text{unocc}}, k_{\text{occ}}, \omega) + I(|\mathbf{k}+\mathbf{q}|_{\text{unocc}}, k_{\text{occ}}, -\omega)\right], \tag{C.7}$$

it is possible to limit the calculation to the first term. For the case of $G = G_0$ of Sec. 6.2, the occupied states at momentum k are all within the Fermi sphere, and thus we can limit the momentum integration to the sphere of radius k_f, i.e. $k \leq k_f$ in Eqs. (6.1) and (6.2).

C.3 Total energy convergence studies for several densities of the HEG

In Fig. C.2, we report the convergence studies obtained for the total energy at all densities following the protocol detailed in Sec. C.4. We omit the density corresponding to $r_s = 4$ since it has already been treated in the main text. Similar considerations to the $r_s = 4$ case can be drawn for these cases.

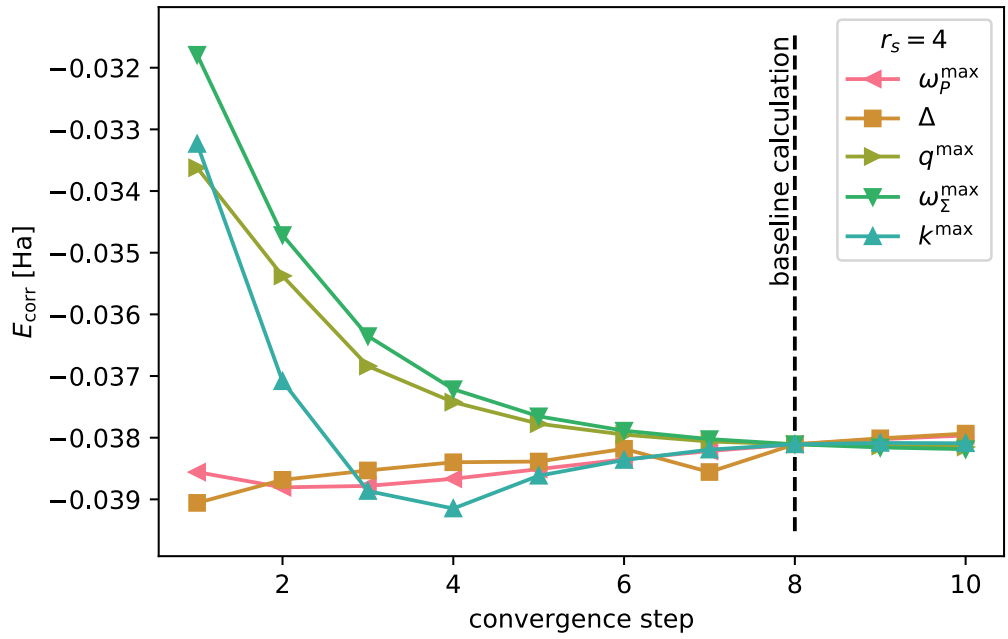

Figure C.3: Convergence study for the correlation energy per particle E_{corr} from a G_0W_0 calculation for the HEG at $r_s = 4$. The parameters to converge are described in Sec. C.4. For each convergence curve (represented by a single line), we study the value of E_{corr} by varying the corresponding parameter, fixing all the others at the convergence point (called baseline calculation). At each step, we vary the target parameter by 20% in the convergent direction and observe a plateau in E_{corr}.

C.4 Numerical details

Here we discuss and report the parameters that control the numerical accuracy of the quantities (polarizability, self-energy, total energy) computed by means of Eqs. (6.2), (6.4), and (6.5). For the spectral quantities, this corresponds to going from left to right in the flow diagram of Fig. 6.1 following the green path, performing all calculations mentioned in the boxes.

The first quantity to be computed is the polarizability $P(q,\omega)$. For each momentum q and frequency ω, we perform the integral of Eq. (6.2). We choose an initial free-particle Green's function having a 2nd order Lorentzian pole at each k broadened by δ_P. The k-momentum integral of Eq. (6.2) is limited by k_f (see Sec. 6.2), and we denote the spacing of the k- and x-grids by Δk_P and Δx_P, respectively. We call the spacing of the (q,ω) grid Δq and $\Delta\omega_P$ and build the q grid from 0 to $q^{\max}$ and the polarizability frequency grid from $[-\omega_P^{\max}, \omega_P^{\max}]$. Note that we will need to converge all the grid spacing parameters to zero, $\delta_P \to 0$, and $q^{\max}, \omega_P^{\max} \to \infty$. Due to the frequency structure of the polarizability, for this calculation, it is best to pass to energy units that depend on the specific q-point, following the law $f(q) = \sqrt{q} + q^2$. Thus, in these units, the maximum of the frequency grid $\omega_P^{\max}$ scales with q and specifically goes to 0 as $q \to 0$ and to infinity as $q \to \infty$. The scaling of the frequency grid allows for the polarizability to decay to 0 at the different momenta q, without having large frequency grids at small momenta,

and was designed looking at the ω/q dependence of the RPA-polarizability (e.g., from Eq. (C.5) of Sec. C.1 of the Appendix).

Moving to the central part of the flow chart in Fig. 6.1, we obtain the SOP representation of the polarizability using the method described in Sec. 3.3. We place the center of the 2nd order Lorentzians on the midpoints of the frequency grid with a broadening equal to the spacing of the grid, and with this choice, the accuracy of the fit improves as $\Delta\omega_P \to 0$. Next, we use the algorithmic-inversion method to obtain the SOP of the screened potential W from the SOP representation of the polarizability.

Using the SOP representation of W (and of G), the self-energy integral (right part of Fig. 6.1), Eq. (6.4), is formally identical to the integral in Eq. (6.2) for the polarizability. Therefore, the remaining parameters to converge are δ_Σ, Δx_Σ, Δk, $\Delta\omega_\Sigma$, $k^{\max}$, and $\omega_\Sigma^{\max}$ (using the same notation adopted above).

As for the polarizability P, we obtain the SOP representation of the self-energy following the method described in Sec. 3.3. We place the center of the 2nd order Lorentzians on the midpoints of the frequency grid with a broadening equal to the spacing of the grid. Finally, we obtain the SOP representation of the Green's function by employing the algorithmic-inversion method.

Using the resulting Green's function, we compute the thermodynamic quantities following the flow chart in Fig. 6.2 and study the numerical stability of the computational procedure with respect to all the aforementioned parameters. In this work, we choose to converge the total energy, as obtained in Sec. C.4, which is sensitive enough to guarantee reasonable convergence for the other spectral properties of interest. By changing individually each parameter (increase or decrease by 20% of its value towards convergence), we study the stability of the total energy against the selected parameter, keeping the values of all the others fixed at a reference point (baseline calculation of Fig. C.3). Each target parameter is then converged separately We continue the convergence until a plateau for the subsequent values of the computed quantity is observed. We evaluate the error in the result by considering the two most distant values among those in the plateau.

Importantly, it is possible to reduce the number of parameters to converge from 13 to 5, by linking all the grid-spacing and broadening of the initial G_0 parameters together into a single variable, Δ, which ensures convergence for $\Delta \to 0^+$. Specifically, we bind those parameters together by setting $\Delta = \Delta k_P/k_f = 5\Delta x_P/k_f = \frac{1}{6}\Delta\omega_P/\epsilon_f = \frac{1}{9}\Delta q/k_f = \frac{1}{25}\Delta\omega_\Sigma/\epsilon_f = \Delta x_\Sigma/k_f = \frac{1}{3}\Delta k_\Sigma/k_f = \frac{5}{4}\delta_P/\epsilon_f = \frac{1}{100}\delta_\Sigma/\epsilon_f$.

Together with Δ, the grid-limit parameters are converged separately, following the strategy designed above. The converged values obtained for all the calculated densities are: $\Delta = 0.00133$, $q^{\max} = 7.292\ k_f$, $k^{\max} = 3.60\ k_f$, $\omega_P^{\max} = 5.0\ \epsilon_f$, and $\omega_\Sigma^{\max} = 10.985\ \epsilon_f$, where k_f is the Fermi momentum and ϵ_f is the Fermi energy.

To give a sense of how many poles are needed in our approach—recalling that the number of poles is equal to the number of points in the frequency mesh times the degree of the Lorentzians—we highlight that at convergence we use for the polarizability and screened potential $2 \times \frac{\omega_P^{\max}}{\delta_P} / \approx 2400$ poles, and for the self-energy $2 \times \frac{\omega_\Sigma^{\max}}{\delta_\Sigma} / \approx 660$ poles. Furthermore, most of the computational time is spent performing the convolutions of Eqs. (6.2) and (6.4), even if a linear scaling is implied in the number of poles of the propagators by exploiting Eq. (3.12).

As a last point, we stress that all of our calculations are performed with the electron-electron self-energy shifted by μ, i.e., $G(k,\omega) = [\omega - \epsilon_k^0 - \Sigma(k,\omega) + \mu]^{-1}$.

This choice ensures that all energy scales are aligned with the chemical potential for all propagators, and in particular, that evaluating $\Sigma(k_f, \omega = 0)$ means evaluating the self-energy at $k = k_f$ and at the chemical potential.

In this sense, we define the chemical potential μ as $\mu = \epsilon_f + \Sigma(k_f, 0)$ and update it after the G_0W_0 cycle.

This manual shift for μ originates from the non-self-consistent nature of the G_0W_0 calculations and helps to conserve the number of particles and the analytic structure of the propagator G, including, for example, the analytic divergence of the spectral function A at $k = k_f$ and $\omega = \mu$. A similar approach is also used in Refs. [56, 88, 125].

D Details in AIM-SOP for crystals using dynamical Hubbard

D.1 Charge rearrangement

To get a qualitative picture of the lowering of the bulk modulus of $SrVO_3$ when applying the localized GW approach, in Fig. D.1 we compare charge-density differences from different methods along the (100) plane. On the plane, vanadium atoms are on the corners, and oxygen atoms are on the midpoint of each edge of the cell. The color-coding in the plots is red-green-blue, with red being positive, green zero, and blue negative. In panel D.1a, one can see the comparison between the DFT and DFT+U charge densities. Looking at the left corner, one can see that there is no qualitative change in the charge density at the middle of the bond between

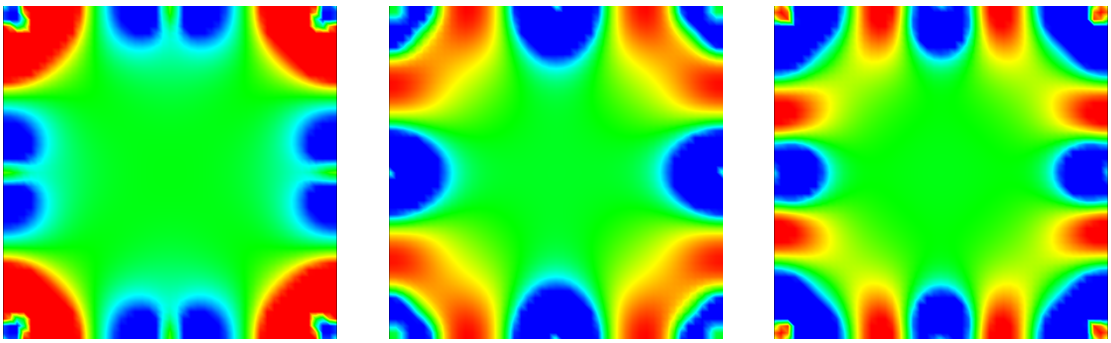

(a) $\rho^{\mathrm{DFT}} - \rho^{\mathrm{DFT+U}}$ (b) $\rho^{\mathrm{DFT}} - \rho^{GW_{\mathrm{Loc}}}$ (c) $\rho^{\mathrm{DFT+U}} - \rho^{GW_{\mathrm{Loc}}}$

Figure D.1: Comparison between charge-density differences from different methods along the 100 plane on $SrVO_3$. In the cell, vanadium atoms are on the corners, oxygen atoms are on the midpoint of each edge, and strontium is at the center of the cell and cannot be seen from the plot since it is in the center of the cell and we are cutting with a plane on the surface of the cell. All calculations are done at the experimental equilibrium ($T = 0$ limit) lattice parameter of $SrVO_3$. See the text for more details. The color-coding is red-green-blue, with red being positive, green zero, blue negative. Same colors for different plots correspond to the same value. For example, in panel (b) the zone where it is red, ρ^{DFT} is higher than $\rho^{GW_{\mathrm{Loc}}}$, where it is blue, it is vice versa, and where it is green, the system has the same electronic charge density.

the vanadium and oxygen atoms. Conversely, in the other two plots, the DFT (panel D.1b) or the DFT+U (panel D.1c) charge in the middle is pulled toward the atoms. Effectively, this can account for a lowering of the bulk modulus obtained by the localized-GW approach with respect to DFT and DFT+U. Also, since the Hubbard manifold is around the vanadium atom, no changes in the charge density on the strontium atom are observed.

D.2 Numerical details

All DFT and DFT+U calculations were performed using the QUANTUM ESPRESSO distribution [126]. The energy, self-energy, Green's function, and spectral function were computed with a (private) PYTHON implementation of the generalized Hubbard approach described in the main text. The localized screened-potential $U(\omega)$ was calculated using RESPACK [127]. The pseudopotentials used for all the calculations are optimized norm-conserving pseudopotentials [128] (PBEsol standard-precision, nc-sr-04) from the PSEUDO DOJO library [129]. The sum-over-poles form for $U(\omega)$ was obtained using an in-house PYTHON implementation of the algorithm described in Sec. 7.4.

For the calculations in Figs. 7.2 (main text) and D.1 (Supp. Mater.), and Table 7.1 (main text), i.e., all but those for the equation of state (EOS), we use a simple cubic cell having a lattice parameter of $a = 3.824$ Å. This value is the extrapolated value at the zero-temperature limit of the experimental value $a = 3.841$ Å from Refs. [106] and [130], considering an average linear thermal expansion coefficient $\alpha_l = 1.45 \times 10^{-5} K^{-1}$ from Ref. [106].

For all electronic structure calculations, we use a Marzari-Vanderbilt [131] smearing of ~ 0.27 eV. For the generalized Hubbard calculations involving G_{KS}, we shift the poles above and below the real axis with an effective amount of $i\eta_\pm = \pm i\ 0.1$ eV, depending on whether the pole is occupied (+) or empty (−). To implement the smearing in G_{KS}, we double each pole to be both above and below the real axis, multiplying its occupation—1 in the Kohn and Sham basis—by a factor of $f^\pm(1 - f^\pm)$, where + is the sign of $\eta_\pm$. Here, f^+ is the Marzari-Vanderbilt smearing function, and $f^- = 1 - f^+$.

For all total energy and ground-state density calculations, including DFT, DFT+U, and generalized Hubbard, we use a $12\times12\times12$ **k**-point Monkhorst-Pack grid. Specifically, this **k**-grid is used to compute E_{tot} in the lines "DFT, DFT+U, This work" of Table 7.1, as well as the equation of state in Fig. 7.3 and the charge-density differences in Fig. D.1. With the chosen values, we ensure a convergence of 10 meV (or better) for the total energy in DFT.

Due to the **k**-point sampling, the localized-GW approach requires an additional "pole-condensation" procedure. The issue arises from the number of poles of the self-energy, which scales linearly with the dimension of H_{AIM}, which we need to diagonalize. The self-energy poles are calculated from Eq. (7.2), using the SOP form for **G** and U. Specifically, the number of poles of Σ equals the number of poles of **G** multiplied by those of U. While U introduces a number of poles on the order of 10, the projected KS Green's function has poles at all KS states with

residues as projections over the Hubbard manifold,

$$\mathbf{G}^{\mathrm{KS}}_{mm'}(\omega) = \sum_{\mathbf{k},n} \frac{\langle m|\psi_{n\mathbf{k}}\rangle\langle\psi_{n\mathbf{k}}|m'\rangle}{\omega - \epsilon_{n\mathbf{k}} + i\eta_{\pm}}, \tag{D.1}$$

where $|m\rangle$ span the Hubbard manifold, and $\psi_{n\mathbf{k}}, \epsilon_{n\mathbf{k}}$ are the Kohn-Sham orbitals and eigenvalues. The sum is performed over all Kohn-Sham states. Thus, with a $12\times12\times12$ grid and 25 orbitals in the calculation, one obtains more than 10,000 poles (without point-group symmetries). As with the density of states, in the localized representation, most of these poles effectively overlap, resulting in a structure that can be represented with many fewer poles.

In order to condense the poles, we use the algorithm described in Sec. 3.6. We check that the value chosen for the threshold changes the total energy by less than 10 meV. With this procedure, we are able to reduce the number of poles to a few hundred (without symmetries), making the diagonalization of H_{AIM} computationally much cheaper.

Bibliography

[1] N. Marzari, A. Ferretti, and C. Wolverton, *Electronic-structure methods for materials design*, Nature Materials **20**, 736 (2021).

[2] G. Materzanini, T. Chiarotti, and N. Marzari, *Solids that are also liquids: elastic tensors of superionic materials*, npj Computational Materials **9**, 1 (2023).

[3] J. S. Zhou, L. Reining, A. Nicolaou, A. Bendounan, K. Ruotsalainen, M. Vanzini, J. J. Kas, J. J. Rehr, M. Muntwiler, V. N. Strocov, F. Sirotti, and M. Gatti, *Unraveling intrinsic correlation effects with angle-resolved photoemission spectroscopy*, Proceedings of the National Academy of Sciences **117**, 28596 (2020).

[4] N. Mounet, M. Gibertini, P. Schwaller, D. Campi, A. Merkys, A. Marrazzo, T. Sohier, I. E. Castelli, A. Cepellotti, G. Pizzi, and N. Marzari, *Two-dimensional materials from high-throughput computational exfoliation of experimentally known compounds*, Nature Nanotechnology **13**, 246 (2018).

[5] M. T. Yin and M. L. Cohen, *Microscopic Theory of the Phase Transformation and Lattice Dynamics of Si*, Physical Review Letters **45**, 1004 (1980).

[6] A. De Vita, G. Galli, A. Canning, and R. Car, *A microscopic model for surface-induced diamond-to-graphite transitions*, Nature **379**, 523 (1996).

[7] M. Guzzo, G. Lani, F. Sottile, P. Romaniello, M. Gatti, J. J. Kas, J. J. Rehr, M. G. Silly, F. Sirotti, and L. Reining, *Valence Electron Photoemission Spectrum of Semiconductors: Ab Initio Description of Multiple Satellites*, Physical Review Letters **107**, 166401 (2011).

[8] V. Olevano and L. Reining, *Excitonic Effects on the Silicon Plasmon Resonance*, Physical Review Letters **86**, 5962 (2001).

[9] P. Hohenberg and W. Kohn, *Inhomogeneous Electron Gas*, Physical Review **136**, B864 (1964).

[10] J. P. Perdew, K. Burke, and M. Ernzerhof, *Generalized Gradient Approximation Made Simple*, Physical Review Letters **77**, 3865 (1996).

[11] J. P. Perdew, W. Yang, K. Burke, Z. Yang, E. K. U. Gross, M. Scheffler, G. E. Scuseria, T. M. Henderson, I. Y. Zhang, A. Ruzsinszky, H. Peng, J. Sun, E. Trushin, and A. Görling, *Understanding band gaps of solids in generalized Kohn–Sham theory*, Proceedings of the National Academy of Sciences **114**, 2801 (2017).

[12] J. Sun, A. Ruzsinszky, and J. Perdew, *Strongly Constrained and Appropriately Normed Semilocal Density Functional*, Physical Review Letters **115**, 036402 (2015).

[13] A. J. Cohen, P. Mori-Sánchez, and W. Yang, *Insights into Current Limitations of Density Functional Theory*, Science **321**, 792 (2008).

[14] N. L. Nguyen, N. Colonna, A. Ferretti, and N. Marzari, *Koopmans-Compliant Spectral Functionals for Extended Systems*, Physical Review X **8**, 021051 (2018).

[15] N. Colonna, N. L. Nguyen, A. Ferretti, and N. Marzari, *Koopmans-Compliant Functionals and Potentials and Their Application to the GW100 Test Set*, Journal of Chemical Theory and Computation **15**, 1905 (2019).

[16] N. Colonna, R. De Gennaro, E. Linscott, and N. Marzari, *Koopmans Spectral Functionals in Periodic Boundary Conditions*, Journal of Chemical Theory and Computation **18**, 5435 (2022).

[17] R. De Gennaro, N. Colonna, E. Linscott, and N. Marzari, *Bloch's theorem in orbital-density-dependent functionals: Band structures from Koopmans spectral functionals*, Physical Review B **106**, 035106 (2022).

[18] L. Reining, *The GW approximation: content, successes and limitations*, Wiley Interdisciplinary Reviews: Computational Molecular Science **8**, e1344 (2018).

[19] J. M. Luttinger and J. C. Ward, *Ground-State Energy of a Many-Fermion System. II*, Physical Review **118**, 1417 (1960).

[20] R. M. Martin, L. Reining, and D. M. Ceperley, *Interacting Electrons: Theory and Computational Approaches*, 2016.

[21] A. Georges, G. Kotliar, W. Krauth, and M. J. Rozenberg, *Dynamical mean-field theory of strongly correlated fermion systems and the limit of infinite dimensions*, Reviews of Modern Physics **68**, 13 (1996).

[22] A. A. Kananenka, E. Gull, and D. Zgid, *Systematically improvable multiscale solver for correlated electron systems*, Physical Review B **91**, 121111 (2015).

[23] T. N. Lan and D. Zgid, *Generalized Self-Energy Embedding Theory*, The Journal of Physical Chemistry Letters **8**, 2200 (2017).

[24] A. Calzolari, N. Marzari, I. Souza, and M. Buongiorno Nardelli, *Ab initio transport properties of nanostructures from maximally localized Wannier functions*, Physical Review B **69**, 035108 (2004).

[25] A. Ferretti, A. Calzolari, B. Bonferroni, and R. D. Felice, *Maximally localized Wannier functions constructed from projector-augmented waves or ultrasoft pseudopotentials*, Journal of Physics: Condensed Matter **19**, 036215 (2007).

[26] G. Baym and L. P. Kadanoff, *Conservation Laws and Correlation Functions*, Physical Review **124**, 287 (1961).

[27] G. Baym, *Self-Consistent Approximations in Many-Body Systems*, Physical Review **127**, 1391 (1962).

[28] G. Stefanucci and R. v. Leeuwen, *Nonequilibrium Many-Body Theory of Quantum Systems: A Modern Introduction*, 2013.

[29] C.-O. Almbladh, U. V. Barth, and R. V. Leeuwen, *Variational total energies from phi- and psi- derivable theories*, International Journal of Modern Physics B **13**, 535 (1999).

[30] N. E. Dahlen and U. v. Barth, *Variational energy functionals tested on atoms*, Physical Review B **69**, 195102 (2004).

[31] L. Hedin and S. Lundqvist, *Effects of Electron-Electron and Electron-Phonon Interactions on the One-Electron States of Solids*, in *Solid State Physics*, edited by F. Seitz, D. Turnbull, and H. Ehrenreich, volume 23, pages 1–181, Academic Press, 1970.

[32] G. Kotliar, S. Y. Savrasov, K. Haule, V. S. Oudovenko, O. Parcollet, and C. A. Marianetti, *Electronic structure calculations with dynamical mean-field theory*, Reviews of Modern Physics **78**, 865 (2006).

[33] S. L. Dudarev, G. A. Botton, S. Y. Savrasov, C. J. Humphreys, and A. P. Sutton, *Electron-energy-loss spectra and the structural stability of nickel oxide: An LSDA+U study*, Physical Review B **57**, 1505 (1998).

[34] T. Chiarotti, N. Marzari, and A. Ferretti, *Unified Green's function approach for spectral and thermodynamic properties from algorithmic inversion of dynamical potentials*, Physical Review Research **4**, 013242 (2022).

[35] T. Chiarotti, A. Ferretti, and N. Marzari, *Energies and spectra of solids from the algorithmic inversion of localized GW*, arxiv, submitted (24 Feb 2023).

[36] N. W. Ashcroft and N. D. Mermin, *Solid State Physics*, Holt, Rinehart and Winston, 1976, Google-Books-ID: 1C9HAQAAIAAJ.

[37] M. Born and R. Oppenheimer, *Zur Quantentheorie der Molekeln*, Annalen der Physik **389**, 457 (1927).

[38] J. C. Slater, *The Theory of Complex Spectra*, Physical Review **34**, 1293 (1929).

[39] D. R. Hartree, *The Wave Mechanics of an Atom with a Non-Coulomb Central Field. Part II. Some Results and Discussion*, Mathematical Proceedings of the Cambridge Philosophical Society **24**, 111 (1928).

[40] D. A. Mazziotti, *Structure of Fermionic Density Matrices: Complete N-Representability Conditions*, Physical Review Letters **108**, 263002 (2012).

[41] S. M. Valone, *A one-to-one mapping between one-particle densities and some n-particle ensembles*, The Journal of Chemical Physics **73**, 4653 (1980).

[42] W. Kohn and L. J. Sham, *Self-Consistent Equations Including Exchange and Correlation Effects*, Physical Review **140**, A1133 (1965).

[43] G. Giuliani and G. Vignale, *Quantum Theory of the Electron Liquid*, 2005.

[44] W. Kohn, *Density Functional and Density Matrix Method Scaling Linearly with the Number of Atoms*, Physical Review Letters **76**, 3168 (1996).

[45] E. Prodan and W. Kohn, *Nearsightedness of electronic matter*, Proceedings of the National Academy of Sciences **102**, 11635 (2005).

[46] D. M. Ceperley and B. J. Alder, *Ground State of the Electron Gas by a Stochastic Method*, Physical Review Letters **45**, 566 (1980).

[47] J. P. Perdew and A. Zunger, *Self-interaction correction to density-functional approximations for many-electron systems*, Physical Review B **23**, 5048 (1981).

[48] L. J. Sham and M. Schlüter, *Density-Functional Theory of the Energy Gap*, Physical Review Letters **51**, 1888 (1983).

[49] A. Georges and G. Kotliar, *Hubbard model in infinite dimensions*, Physical Review B **45**, 6479 (1992).

[50] K. Haule, *Exact Double Counting in Combining the Dynamical Mean Field Theory and the Density Functional Theory*, Physical Review Letters **115**, 196403 (2015).

[51] M. E. Casida, *Generalization of the optimized-effective-potential model to include electron correlation: A variational derivation of the Sham-Schl\"uter equation for the exact exchange-correlation potential*, Physical Review A **51**, 2005 (1995).

[52] M. Gatti, V. Olevano, L. Reining, and I. V. Tokatly, *Transforming Nonlocality into a Frequency Dependence: A Shortcut to Spectroscopy*, Physical Review Letters **99**, 057401 (2007).

[53] B. Farid, R. Daling, D. Lenstra, and W. van Haeringen, *GW approach to the calculation of electron self-energies in semiconductors*, Physical Review B **38**, 7530 (1988).

[54] G. E. Engel, B. Farid, C. M. M. Nex, and N. H. March, *Calculation of the GW self-energy in semiconducting crystals*, Physical Review B **44**, 13356 (1991).

[55] B. Holm and F. Aryasetiawan, *Self-consistent cumulant expansion for the electron gas*, Physical Review B **56**, 12825 (1997).

[56] U. von Barth and B. Holm, *Self-consistent GW results for the electron gas: Fixed screened potential W within the random-phase approximation*, Physical Review B **54**, 8411 (1996).

[57] M. Abramowitz, I. A. Stegun, and R. H. Romer, *Handbook of Mathematical Functions with Formulas, Graphs, and Mathematical Tables*, American Journal of Physics **56**, 958 (1988).

[58] P. Virtanen, R. Gommers, T. E. Oliphant, M. Haberland, T. Reddy, D. Cournapeau, E. Burovski, P. Peterson, W. Weckesser, J. Bright, S. J. van der Walt, M. Brett, J. Wilson, K. J. Millman, N. Mayorov, A. R. J. Nelson, E. Jones, R. Kern, E. Larson, C. J. Carey, I. Polat, Y. Feng, E. W. Moore, J. VanderPlas, D. Laxalde, J. Perktold, R. Cimrman, I. Henriksen, E. A. Quintero, C. R. Harris, A. M. Archibald, A. H. Ribeiro, F. Pedregosa, and P. van Mulbregt, *SciPy 1.0: fundamental algorithms for scientific computing in Python*, Nature Methods **17**, 261 (2020).

[59] C. L. Lawson and R. J. Hanson, *Solving Least Squares Problems*, Classics in Applied Mathematics, Society for Industrial and Applied Mathematics, 1995.

[60] W. H. Press, S. A. Teukolsky, W. T. Vetterling, and B. P. Flannery, *Numerical Recipes 3rd Edition: The Art of Scientific Computing*, Cambridge University Press, 2007.

[61] K.-H. Lee and K. J. Chang, *Analytic continuation of the dynamic response function using an N-point Pad\'e approximant*, Physical Review B **54**, R8285 (1996).

[62] D. A. Leon, C. Cardoso, T. Chiarotti, D. Varsano, E. Molinari, and A. Ferretti, *Frequency dependence in GW made simple using a multipole approximation*, Physical Review B **104**, 115157 (2021).

[63] S. Güttel and F. Tisseur, *The nonlinear eigenvalue problem**, Acta Numerica **26**, 1 (2017).

[64] G. B. Thomas and M. D. Weir, *Calculus and Analytic Geometry*, Addison-Wesley, 1988.

[65] S. Y. Savrasov, K. Haule, and G. Kotliar, *Many-Body Electronic Structure of Americium Metal*, Physical Review Letters **96**, 036404 (2006).

[66] L. Wang, H. Jiang, X. Dai, and X. C. Xie, *Pole expansion of self-energy and interaction effect for topological insulators*, Physical Review B **85**, 235135 (2012).

[67] J. C. Budich, R. Thomale, G. Li, M. Laubach, and S.-C. Zhang, *Fluctuation-induced topological quantum phase transitions in quantum spin-Hall and anomalous-Hall insulators*, Physical Review B **86**, 201407 (2012).

[68] S. J. Bintrim and T. C. Berkelbach, *Full-frequency GW without frequency*, The Journal of Chemical Physics **154**, 041101 (2021).

[69] Y. Cho, S. J. Bintrim, and T. C. Berkelbach, *Simplified GW/BSE Approach for Charged and Neutral Excitation Energies of Large Molecules and Nanomaterials*, Journal of Chemical Theory and Computation **18**, 3438 (2022).

[70] D. Nabok, S. Blügel, and C. Friedrich, *Electron–plasmon and electron–magnon scattering in ferromagnets from first principles by combining GW and GT self-energies*, npj Computational Materials **7**, 1 (2021).

[71] M. Vanzini and N. Marzari, *Towards a minimal description of dynamical correlation in metals*, in preparation (2023).

[72] V. I. Anisimov, F. Aryasetiawan, and A. I. Lichtenstein, *First-principles calculations of the electronic structure and spectra of strongly correlated systems: theLDA$\mathplus$Umethod*, Journal of Physics: Condensed Matter **9**, 767 (1997).

[73] H. Jiang, R. I. Gomez-Abal, P. Rinke, and M. Scheffler, *First-principles modeling of localized d states with the $GW@\text{LDA}+U$ approach*, Physical Review B **82**, 045108 (2010).

[74] H. N. Rojas, R. W. Godby, and R. J. Needs, *Space-Time Method for Ab Initio Calculations of Self-Energies and Dielectric Response Functions of Solids*, Physical Review Letters **74**, 1827 (1995).

[75] M. M. Rieger, L. Steinbeck, I. D. White, H. N. Rojas, and R. W. Godby, *The GW space-time method for the self-energy of large systems*, Computer Physics Communications **117**, 211 (1999).

[76] P. García-González and R. W. Godby, *Self-consistent calculation of total energies of the electron gas using many-body perturbation theory*, Physical Review B **63**, 075112 (2001).

[77] A. L. Fetter and J. D. Walecka, *Quantum Theory of Many-particle Systems*, Courier Corporation, 2003.

[78] L. Hedin, J. Michiels, and J. Inglesfield, *Transition from the adiabatic to the sudden limit in core-electron photoemission*, Physical Review B **58**, 15565 (1998).

[79] A. Damascelli, Z. Hussain, and Z.-X. Shen, *Angle-resolved photoemission studies of the cuprate superconductors*, Reviews of Modern Physics **75**, 473 (2003).

[80] D. Golze, M. Dvorak, and P. Rinke, *The GW Compendium: A Practical Guide to Theoretical Photoemission Spectroscopy*, Frontiers in Chemistry **7** (2019).

[81] A. Schindlmayr, P. García-González, and R. W. Godby, *Diagrammatic self-energy approximations and the total particle number*, Physical Review B **64**, 235106 (2001).

[82] N. E. Dahlen, R. van Leeuwen, and U. von Barth, *Variational energy functionals of the Green function and of the density tested on molecules*, Physical Review A **73**, 012511 (2006).

[83] Y. Pavlyukh, G. Stefanucci, and R. van Leeuwen, *Dynamically screened vertex correction to GW*, Physical Review B **102**, 045121 (2020).

[84] A. L. Kutepov, *Electronic structure of Na, K, Si, and LiF from self-consistent solution of Hedin's equations including vertex corrections*, Physical Review B **94**, 155101 (2016).

[85] A. L. Kutepov and G. Kotliar, *One-electron spectra and susceptibilities of the three-dimensional electron gas from self-consistent solutions of Hedin's equations*, Physical Review B **96**, 035108 (2017).

[86] R. Levy, J. P. F. LeBlanc, and E. Gull, *Implementation of the maximum entropy method for analytic continuation*, Computer Physics Communications **215**, 149 (2017).

[87] R. N. Silver, D. S. Sivia, and J. E. Gubernatis, *Maximum-entropy method for analytic continuation of quantum Monte Carlo data*, Physical Review B **41**, 2380 (1990).

[88] B. Holm and U. von Barth, *Fully self-consistent GW self-energy of the electron gas*, Physical Review B **57**, 2108 (1998).

[89] B. Holm and F. Aryasetiawan, *Total energy from the Galitskii-Migdal formula using realistic spectral functions*, Physical Review B **62**, 4858 (2000).

[90] B. I. Lundqvist, *Single-particle spectrum of the degenerate electron gas. I*, Physik der kondensierten Materie **6**, 193 (1967).

[91] B. I. Lundqvist, *Single particle spectrum of the degenerate electron gas. II*, Physik der kondensierten Materie **6**, 206 (1967).

[92] B. I. Lundqvist, *Single-particle spectrum of the degenerate electron gas*, Physik der kondensierten Materie **7**, 117 (1968).

[93] L. N. Trefethen and J. a. C. Weideman, *The Exponentially Convergent Trapezoidal Rule*, SIAM Review **56**, 385 (2014).

[94] T. Chiarotti and S. Vacondio and A. Ferretti, `AGWX` code suite.

[95] F. Caruso and F. Giustino, *The GW plus cumulant method and plasmonic polarons: application to the homogeneous electron gas**, The European Physical Journal B **89**, 238 (2016).

[96] Y. Dewulf, D. Van Neck, and M. Waroquier, *Discrete approach to self-consistent GW calculations in an electron gas*, Physical Review B **71**, 245122 (2005).

[97] J. J. Kas, J. J. Rehr, and L. Reining, *Cumulant expansion of the retarded one-electron Green function*, Physical Review B **90**, 085112 (2014).

[98] M. Z. Mayers, M. S. Hybertsen, and D. R. Reichman, *Description of quasiparticle and satellite properties via cumulant expansions of the retarded one-particle Green's function*, Physical Review B **94**, 081109 (2016).

[99] R. Sakuma, C. Martins, T. Miyake, and F. Aryasetiawan, *Ab initio study of the downfolded self-energy for correlated systems: Momentum dependence and effects of dynamical screening*, Physical Review B **89**, 235119 (2014).

[100] T. Miyake, C. Martins, R. Sakuma, and F. Aryasetiawan, *Effects of momentum-dependent self-energy in the electronic structure of correlated materials*, Physical Review B **87**, 115110 (2013).

[101] J. M. Tomczak, M. Casula, T. Miyake, and S. Biermann, *Asymmetry in band widening and quasiparticle lifetimes in ${\mathrm{SrVO}}_{3}$: Competition between screened exchange and local correlations from combined GW and dynamical mean-field theory $GW + \mathrm{DMFT}$*, Physical Review B **90**, 165138 (2014).

[102] R. Sakuma, P. Werner, and F. Aryasetiawan, *Electronic structure of SrVO${}_{3}$ within GW+DMFT*, Physical Review B **88**, 235110 (2013).

[103] L. Boehnke, F. Nilsson, F. Aryasetiawan, and P. Werner, *When strong correlations become weak: Consistent merging of GW and DMFT*, Physical Review B **94**, 201106 (2016).

[104] T. Yoshida, K. Tanaka, H. Yagi, A. Ino, H. Eisaki, A. Fujimori, and Z.-X. Shen, *Direct Observation of the Mass Renormalization in ${\mathrm{SrVO}}_{3}$ by Angle Resolved Photoemission Spectroscopy*, Physical Review Letters **95**, 146404 (2005).

[105] M. Takizawa, M. Minohara, H. Kumigashira, D. Toyota, M. Oshima, H. Wadati, T. Yoshida, A. Fujimori, M. Lippmaa, M. Kawasaki, H. Koinuma, G. Sordi, and M. Rozenberg, *Coherent and incoherent d band dispersions in ${\text{SrVO}}_{3}$*, Physical Review B **80**, 235104 (2009).

[106] T. Maekawa, K. Kurosaki, and S. Yamanaka, *Physical properties of polycrystalline SrVO3-δ*, Journal of Alloys and Compounds **426**, 46 (2006).

[107] F. Birch, *Finite Elastic Strain of Cubic Crystals*, Physical Review **71**, 809 (1947).

[108] C. P. Koçer, K. Haule, G. L. Pascut, and B. Monserrat, *Efficient lattice dynamics calculations for correlated materials with $\mathrm{DFT}+\mathrm{DMFT}$*, Physical Review B **102**, 245104 (2020).

[109] A. Togo and I. Tanaka, *First principles phonon calculations in materials science*, Scripta Materialia **108**, 1 (2015).

[110] A. Togo, *First-principles Phonon Calculations with Phonopy and Phono3py*, Journal of the Physical Society of Japan **92**, 012001 (2023).

[111] V. M. Galitskii and A. B. Migdal, *APPLICATION OF QUANTUM FIELD THEORY METHODS TO THE MANY BODY PROBLEM*, Zhur. Eksptl'. i Teoret. Fiz. **Vol: 34** (1958).

[112] L. Hedin, *New Method for Calculating the One-Particle Green's Function with Application to the Electron-Gas Problem*, Physical Review **139**, A796 (1965).

[113] D. Bohm and D. Pines, *A Collective Description of Electron Interactions: III. Coulomb Interactions in a Degenerate Electron Gas,* Physical Review **92**, 609 (1953).

[114] M. Cococcioni, *The LDA + U Approach : A Simple Hubbard Correction for Correlated Ground States,* 2012.

[115] I. G. Austin and N. F. Mott, *Metallic and Nonmetallic Behavior in Transition Metal Oxides,* Science **168**, 71 (1970).

[116] J. Hubbard, *Electron correlations in narrow energy bands,* Proceedings of the Royal Society of London. Series A. Mathematical and Physical Sciences **276**, 238 (1963).

[117] J. Hubbard, *Electron correlations in narrow energy bands. II. The degenerate band case,* Proceedings of the Royal Society of London. Series A. Mathematical and Physical Sciences **277**, 237 (1964).

[118] J. Hubbard, *Electron correlations in narrow energy bands III. An improved solution,* Proceedings of the Royal Society of London. Series A. Mathematical and Physical Sciences **281**, 401 (1964).

[119] J. Hubbard, *Electron correlations in narrow energy bands - IV. The atomic representation,* Proceedings of the Royal Society of London. Series A. Mathematical and Physical Sciences **285**, 542 (1965).

[120] J. Hubbard, *Electron correlations in narrow energy bands VI. The connexion with many-body perturbation theory,* Proceedings of the Royal Society of London. Series A. Mathematical and Physical Sciences **296**, 100 (1966).

[121] J. Hubbard, *Electron correlations in narrow energy bands V. A perturbation expansion about the atomic limit,* Proceedings of the Royal Society of London. Series A. Mathematical and Physical Sciences **296**, 82 (1966).

[122] P. Mori-Sánchez, A. J. Cohen, and W. Yang, *Many-electron self-interaction error in approximate density functionals,* The Journal of Chemical Physics **125**, 201102 (2006).

[123] J. P. Perdew, R. G. Parr, M. Levy, and J. L. Balduz, *Density-Functional Theory for Fractional Particle Number: Derivative Discontinuities of the Energy,* Physical Review Letters **49**, 1691 (1982).

[124] M. Cococcioni and S. de Gironcoli, *Linear response approach to the calculation of the effective interaction parameters in the $\mathrm{LDA}+\mathrm{U}$ method,* Physical Review B **71**, 035105 (2005).

[125] H. O. Frota and G. D. Mahan, *Band tails and bandwidth in simple metals,* Physical Review B **45**, 6243 (1992).

[126] P. Giannozzi, S. Baroni, N. Bonini, M. Calandra, R. Car, C. Cavazzoni, D. Ceresoli, G. L. Chiarotti, M. Cococcioni, I. Dabo, A. D. Corso, S. d. Gironcoli, S. Fabris, G. Fratesi, R. Gebauer, U. Gerstmann, C. Gougoussis, A. Kokalj, M. Lazzeri, L. Martin-Samos, N. Marzari, F. Mauri, R. Mazzarello, S. Paolini, A. Pasquarello, L. Paulatto, C. Sbraccia, S. Scandolo, G. Sclauzero, A. P. Seitsonen, A. Smogunov, P. Umari, and R. M. Wentzcovitch, *QUANTUM ESPRESSO: a modular and open-source software project for quantum simulations of materials*, Journal of Physics: Condensed Matter **21**, 395502 (2009).

[127] K. Nakamura, Y. Yoshimoto, Y. Nomura, T. Tadano, M. Kawamura, T. Kosugi, K. Yoshimi, T. Misawa, and Y. Motoyama, *RESPACK: An ab initio tool for derivation of effective low-energy model of material*, Computer Physics Communications **261**, 107781 (2021).

[128] D. R. Hamann, *Optimized norm-conserving Vanderbilt pseudopotentials*, Physical Review B **88**, 085117 (2013).

[129] M. J. van Setten, M. Giantomassi, E. Bousquet, M. J. Verstraete, D. R. Hamann, X. Gonze, and G. M. Rignanese, *The PseudoDojo: Training and grading a 85 element optimized norm-conserving pseudopotential table*, Computer Physics Communications **226**, 39 (2018).

[130] Y. C. Lan, X. L. Chen, and M. He, *Structure, magnetic susceptibility and resistivity properties of SrVO3*, Journal of Alloys and Compounds **354**, 95 (2003).

[131] N. Marzari, D. Vanderbilt, A. De Vita, and M. C. Payne, *Thermal Contraction and Disordering of the Al(110) Surface*, Physical Review Letters **82**, 3296 (1999).